ELECTRONIC PROPERTIES OF AMORPHOUS GERMANIUM-SELENIUM-TELLURIUM SEMICONDUCTORS

by

JOSEPH WIEDER

A dissertation submitted to the Graduate Faculty in Chemistry in partial fulfillment of the requirements for the degree of Doctor of Philosophy, City University of New York.

1976

This manuscript has been read and accepted for the Graduate Faculty in Chemistry in satisfaction of the dissertation requirement for the degree of Doctor of Philosophy.

9/8/76
Date

Seymour Aronson
Seymour Aronson
Examining Committee Chairman

9/8/76
Date

Leonard H. Schwartz
Leonard H. Schwartz
Executive Officer

Vojtech Fried
Professor of Chemistry

Joseph Glickstein
Joseph Glickstein
Professor of Chemistry

George Skorinko
George Skorinko
Professor of Physics

The City University of New York

ABSTRACT

ELECTRONIC PROPERTIES OF AMORPHOUS
GERMANIUM-SELENIUM-TELLURIUM SEMICONDUCTORS

by

JOSEPH WIEDER

The electronic properties of glass samples composed of Ge, Se, and Te in varying amounts were studied in both the bulk and thin-film forms. After preparation of the samples, their non-crystallinity was confirmed by x-ray crystallography, and their composition and homogeneity by electron microprobe analysis. Bulk samples were subjected to d.c. and a.c. conductivity measurements as well as thermoelectric power measurements, all as a function of temperature, in order to determine the activation energy, $\varepsilon_f - \varepsilon_v$, and the carrier type. Thin-film samples were subjected to optical measurements to determine their thicknesses and their absorption and reflection characteristics as a function of wavelength. From these, an energy band gap, $\Delta E_{opt.}$, was estimated. The data on the activation energy, band gap, and carrier type support theoretical models proposed by Mott, Ovshinsky and others to describe electrical conduction in the disordered state.

Current-controlled switching of the bulk samples from the non-crystalline high resistance state to the crystalline low resistance state under the influence of a high electric

field produced by closely spaced electrodes on the sample surface resulted in the formation of a fine filament between the electrodes. Electron microprobe analysis and elemental x-ray mapping were utilized before and after switching to determine if the conducting filament's crystallinity could be related to a composition change induced by Joule heating along the path of the field.

Differential thermal analysis of the bulk samples yielded data corroborating x-ray crystallographic data from annealed samples that suggested the preferential formation of crystalline Te together with or followed by formation of the crystalline eutectic GeTe upon structural transformation from the non-crystalline to the crystalline state. The polycrystalline Te increases the sample conductivity substantially from what it was in the amorphous state; subsequent GeTe formation increases it only somewhat further.

ACKNOWLEDGEMENT

I would like to take this opportunity to thank the members of my committee for contributing their time and advice throughout the course of this project.

Though there are many deserving of it, I would like to express my appreciation singularly,

------ to Seymour Aronson, for his timely suggestions and support as well as his seemingly infinite patience.

------ to John W. Dooley, for the considerable amount of help on both technical and theoretical levels needed to set up many of the experiments, not to mention his making available enormous resources of equipment from the Physics Department.

------ to Ira Sanzon, who found the time and the priority to look at the electronics that were constantly in need of repair.

------ to Ottmar Safferling, for his perennial good nature, and for having glassware always ready the day before which he promised.

------ to Marty Litvak, who introduced me to the wonders of electron microscopy and the methods of high-vacuum technology.

------ to Harry Woodrow, whose assiduous and highly competent labors freed me for other experimental endeavors, while his irrepressible curiosity kept me thinking.

There were, of course, others, members of the Biology, Geology, Physics, and Biochemistry Departments who supplied equipment, as well as my own colleagues and members of the Chemistry faculty who supplied advice and a warm, convivial atmosphere in which to work. In short, "mikawl melamdii hiskalti," from all my teachers have I gained wisdom.

I would also like to thank Harper and Row Publishers, Inc., New York, and Oxford University Press, London for permission to use some of their figures in the background discussions of Sections II and III.

Brooklyn, N.Y.
July, 1976

Joseph Wieder

to my parents

Helena and Ludvik

with love and appreciation

TABLE OF CONTENTS

LIST OF TABLES

LIST OF FIGURES

I. INTRODUCTION

Amorphous semiconductors have been known to exist for some time, although little study of them was done before 1955. In the past decade, however, certain characteristic features have made them the subject of renewed interest for both pragmatic and theoretical purposes.

As their name implies, amorphous semiconductors differ from crystalline semiconductors in that they lack the three-dimensional periodicity inherent in the latter. Instead, the metastable materials form a twofold disordered system. Firstly, there is structural disorder, as in the elemental forms of amorphous Ge, Si, Te, S, and B where the structure is not repetitive beyond a few atomic spacings. In addition, in binary (GeTe), ternary (GeSeTe), and larger systems (AsTeGeSiP) there is considerable compositional disorder, so that the molecular stoichiometry also varies after a few atomic spacings.

Despite the microscopic chaos, amorphous semiconductors have many properties similar to their crystalline counterparts and, because of their disordered structures, some more advantageous ones as well. They are much cheaper to produce, without the need for stringent purity required in crystalline devices where one ppm of As in crystalline Ge changes the conductivity by 10^5. Being already disordered, they are impervious to high radiation fields as well as 1-2% impurity

concentrations[1]. Many of these non-crystalline systems, especially those containing one or more chalcogens from Group VI, S, Se, or Te have been found useful in computer memories, electroluminescent displays, and a variety of electro-optical devices. They have the ability to be switched from a highly resistive state to a conductive state and back again by a short pulse of electrical or optical energy[2,3].

In order to more fully appreciate and exploit these non-crystalline materials, experiments revealing their physical characteristics, electron transport mechanisms, together with optical absorption data have to be correlated with a theoretical model just as was done with crystalline semiconductors. Although the tremendous degree of disorder among various samples of the same material makes this objective a monumental task, a recent government study reviewing past progress attached a great deal of importance to it and recommended optimal support[4].

II. THEORETICAL BACKGROUND

The past forty years have seen the development of solid state physics to the point where just about every electronic transport phenomenon occurring in crystalline materials can be explained by some theoretical model.

Conductivity can either be ionic or electronic in nature. The ionic form is common in molten alkali halides where the ions move toward the oppositely charged electrodes. It occurs also, to some extent, in silicate glasses where small, highly mobile Na^+ impurities move about between the larger SiO covalently bonded molecules[5]. In chalcogenide glasses, with only covalent bonding present, there is no ionic contribution to the conductivity as found in transport experiments done by Kolomiets[1].

Electronic conductivity is of two types, based either on a *band mechanism* or a *hopping mechanism*. In order, primarily, to provide a basis for comparison and contrast between crystalline and non-crystalline materials and to introduce terminology common to both, a brief, largely qualitative survey of the models for the two types of conductivity found in crystalline systems is presented along with more recently developed models proposed for non-crystalline systems. Also, as it happens, the chief commercial application of amorphous semiconductor devices presently is in circumstances where they are switched repeatedly between the non-crystalline

state and the crystalline one in order to utilize their conductivity properties in one or the other.

A. Conduction in Crystalline Material

1. Band Mechanism

Following the Bloch and Wilson development[7,11,12], an electron moving in a perfectly periodic crystalline lattice will be subject to a periodic Coulombic potential (a series of equally spaced potential wells as in the Kronig-Penny model) whose exact form and contribution to the electron's energy depends on whether the "free-electron" or the "tight-binding" approximation is being used. In either case, solution of the Schroedinger equation yields the Bloch function, a time independent wavefunction in 3-dimensions of the form

$$\psi_{\vec{k}}(\vec{r}) = e^{i\vec{k}\vec{r}}\mu_{\vec{k}}(\vec{r}) \qquad (1)$$

where $\vec{k}$ is the propagation vector for plane waves modulated by a function $\mu_{\vec{k}}(\vec{r})$ whose periodicity is that of the crystal lattice.

The resulting energy function can be plotted as a discontinuous function of k to give Figure 1, with discontinuities occurring at $k = n\pi/a$ where a is the lattice constant. These represent interaction with lattice planes (Brillouin zones) which reflect the electron wave and by exchanging energy with the vibrating lattice atoms, phonons, the electron is *scattered*. If, however, $\mu_{\vec{k}}(\vec{r})$ is a constant, the wave

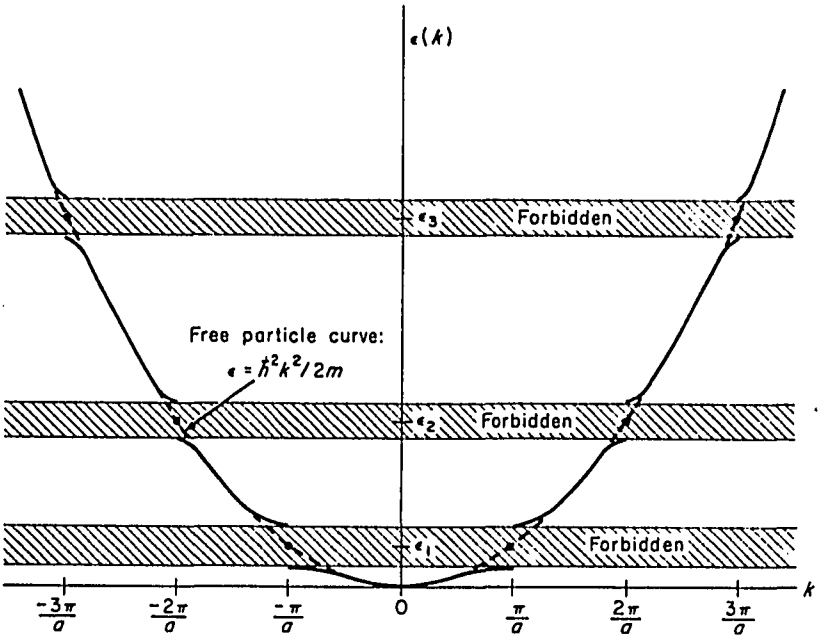

Figure 1. Schematic representation of E vs. k. (After McKelvey, *Solid State and Semiconductor Physics*, Harper and Row, New York, 1966, p.230).

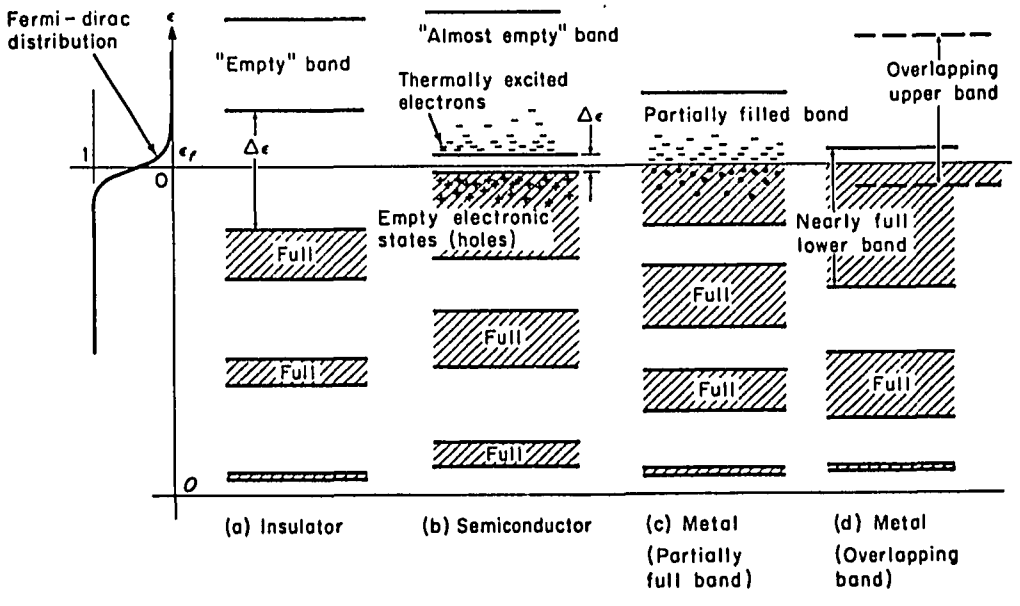

Figure 2. Energy band diagrams for (a) insulator, (b) semiconductor, (c) metallic conductor (partially filled band) and (d) metallic conductor (overlapping bands). (After McKelvey, p.246).

function would take the form $e^{i\vec{k}\vec{r}}$, giving an energy

$$E = \hbar^2 k^2/2m \qquad \text{(in 1 dimension)} \qquad (2)$$

which is just the energy of the free electron in a one dimensional box with momentum $p = \pm\hbar k$ (dashed parabolic curve).

This situation is approximated at higher energies so that an atom's higher energy electrons, i.e. its valence electrons, would be subject to an "effective potential" which can be considered almost constant[6], rather than a periodic one, and solutions of its wavefunctions would extend throughout the lattice, so that energy states can be found anywhere in the lattice, not necessarily localized near individual atoms. This then will be taken as the definition of *non-localized* or *extended* states[8]. This situation, common to real crystalline conductors, also gives rise to a long *mean free path*, ℓ (> 100 lattice spacings) and affects the carrier *mobility*, μ , (velocity per unit of applied field), and *effective mass*, m^*, (expression for apparent changing value of mass at the band edge as a result of the changing curvature as opposed to where electrons at an edge would have constant mass equal to the electron mass).

Differences between conductors, non-conductors and semi-conductors can readily be seen from the schematic in Figure 2.

Conductors typically have an uppermost band containing

the valence electrons, a *valence band*, where, for Group I metals or those transition metals, like Cu and Cr, where each atom has one available valence electron per unit cell, one half of the total energy states in the band will be filled. When an electric field is applied, the electrons are accelerated along the field increasing their kinetic energy and moving into available higher energy states. This also occurs despite the valence band being filled as is the case with Group II metals and most of the transition metals. Here, low-lying higher energy orbitals overlap the filled band making available empty higher energy states and giving a partially-filled band effect.

Non-conductors have completely filled bands with no empty energy states available to the electrons and the Pauli Exclusion principle prevents them from occupying already filled states. The nearest available energy states are located across a large *band gap*, ΔE, ($> 3eV$), too far removed to be reached by thermal or other excitation of the electrons.

Semiconductors, on the other hand, have a smaller value for ΔE (0.2-2.5eV) so that even at room temperature a number of electrons from the top of the valence band have sufficient energy to cross over to the empty *conduction band* leaving behind an equal number of vacancies. Under the influence of an electric field, these relatively few *holes* act as positive electrons or electrons with negative effective mass in that they move in a direction opposite to the one the

remaining multitude of negative electrons move in. Current is thus carried by electrons in the conduction band and holes in the valence band. The carrier with the lower effective mass and consequent higher mobility, will be the predominant one. Although in a perfectly periodic semiconductor with identical lattice spacing in all 3-dimensions, neither predominates, $m^*_{neg.} = m^*_{pos.}$ and $\mu_n = \mu_p$, in a real semiconductor, the lattice constants are not the same in every direction resulting in different values of $m^*_n \neq m^*_p$ and $\mu_n \neq \mu_p$ despite there being the same number of electrons and holes, i.e. despite being an *intrinsic* semiconductor.

There is another type of semiconductor — an *extrinsic* one. Here, additional electron or hole carriers are introduced by the presence of impurity atoms dispersed throughout the lattice. The impurity defect replaces the crystalline atom in the lattice, satisfying local bonding requirements but since it is from a group adjacent to the one containing the crystalline atom , it has either one additional electron or one hole (one fewer electron) which can migrate throughout the lattice leaving an ion behind. These defects give rise to energy states which lie in the energy gap, slightly below the conduction level or slightly above the valence level. In the former case, electrons are excited into an empty conduction band by thermal energy (by as little as 20°K). Similarly, electrons in the valence band move up into the impurity level

above it, filling the holes there, while leaving holes behind at the top of the valence band. The first situation gives an n-type semiconductor, the latter a p-type. Conductivity increases with increased carriers so that the slightest trace of impurities will greatly affect the crystalline semiconductors.

In order to determine the number of carriers in a given energy range which would be involved in the conduction process, it is necessary to combine a function denoting the number of quantum energy states whose energy is in the range $d\varepsilon$ about ε, with a function representing the average number of particles that can occupy the quantum state of energy ε. The first function, called the *density of states*, $g(\varepsilon)d\varepsilon$, and the second, a *distribution function*, $f(\varepsilon)$, together give the number of particles in a given energy range

$$N(\varepsilon)d\varepsilon = f(\varepsilon)g(\varepsilon)d\varepsilon \tag{3}$$

The density of states function can be derived exactly for the case of higher energy particles moving under the influence of a uniform potential which, as mentioned earlier, is approximated by the electrons in the valence band and can be treated as free particles. The result is

$$g(\varepsilon)d\varepsilon = \frac{8\sqrt{2}\pi V m^{3/2}}{h^3}\sqrt{\varepsilon}d\varepsilon \tag{4}$$

where V is the energy volume (actually the volume in momentum space), m is the particle mass, and h is Planck's constant.

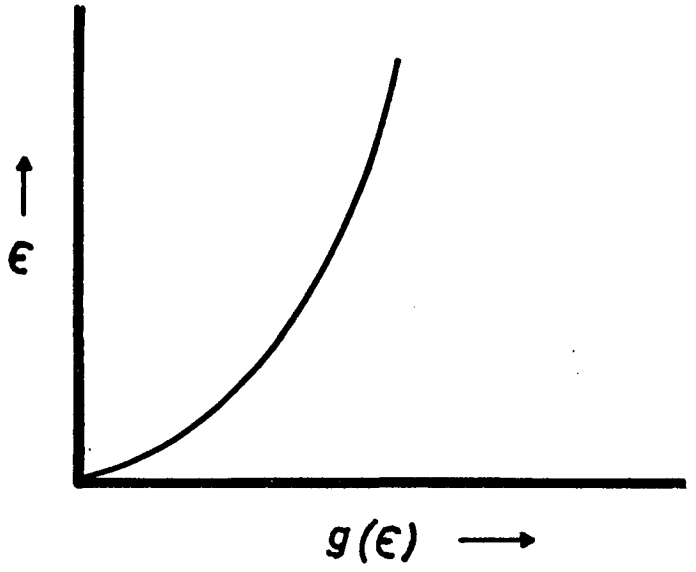

Figure 3. Density of states function for the free-electron model.

$$f(\varepsilon) = 1 \qquad (\varepsilon < \varepsilon_f)$$
$$= 0 \qquad (\varepsilon > \varepsilon_f).$$

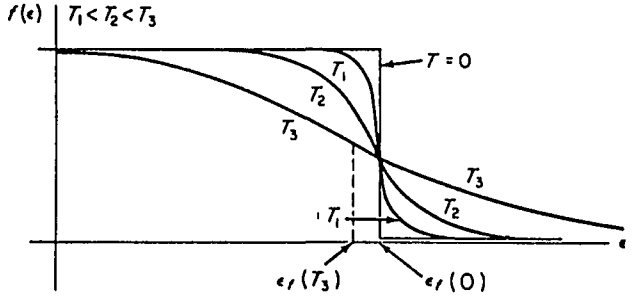

Figure 4. Schematic representation of the Fermi distribution function for four different temperatures. (After McKelvey, p. 153).

The function has the form given by Figure 3.

The actual number of particles that fill the energy bands varies with temperature as well as with energy and is given by a Fermi-Dirac distribution function

$$f(\varepsilon) = \frac{1}{1 + e^{(\varepsilon-\varepsilon_f)/kT}} \tag{5}$$

(where k is the Boltzmann constant) whose variation with the two parameters is illustrated in Figure 4.

The Fermi distribution takes into account the Pauli Exclusion Principle restricting any one quantum state's occupation to one particle. Because of this, the value for $f(\varepsilon)$ at a particular energy will represent the probability that a quantum state at that energy is occupied. The term ε_f refers to the *Fermi energy*, which is a parameter with dimensions of energy and represents the energy level at which $f(\varepsilon)$ becomes equal to 1/2; so that, when $\varepsilon = \varepsilon_f$, a quantum state at the Fermi level has a probability of being filled equal to 1/2.

From the curve, it is apparent that at T=0 all the states are filled and as T increases, even a few kT of energy promote electrons above ε_f and give rise to holes below ε_f. As this occurs, the ε_f level drops further back with increasing energy to accommodate the changing number of filled states and maintain the value of $f(\varepsilon)$ at 1/2.

The particle density as a function of energy can now

be given by

$$N(\varepsilon)d\varepsilon = g(\varepsilon)f(\varepsilon)d\varepsilon = \frac{8\sqrt{2}\ \pi\ V\ m^{3/2}}{h^3(1 + e^{(\varepsilon-\varepsilon_f)/kT})}\sqrt{\varepsilon}\ d\varepsilon \qquad (6)$$

and varies with energy at different temperatures as given by the curves in Figure 5.

For the case of a semiconductor with both valence (v) and conductance (c) bands, the former with particles having negative effective mass, i.e. holes, and the latter having electrons, the density of states per unit volume becomes for the conduction band

$$g_c(\varepsilon)d\varepsilon = \frac{8\sqrt{2}\ \pi\ m_n^{*3/2}}{h^3}\sqrt{\varepsilon-\varepsilon_c}\ d\varepsilon \quad ; \quad (\varepsilon > \varepsilon_c) \qquad (7)$$

and for the valence band

$$g_v(\varepsilon)d\varepsilon = \frac{8\sqrt{2}\ \pi\ m_p^{*3/2}}{h^3}\sqrt{\varepsilon_v-\varepsilon}\ d\varepsilon \quad ; \quad (\varepsilon < \varepsilon_v) \qquad (8)$$

The density of states function now takes the shape of Figure 6, and the density of states in the forbidden energy gap is, of course, zero.

Combining $g(\varepsilon)d\varepsilon$ with the Fermi distribution yields in both intrinsic and extrinsic semiconductors that for electrons

$$dn = N(\varepsilon)d\varepsilon = g_c(\varepsilon)f_n(\varepsilon)d\varepsilon$$

$$= \frac{8\sqrt{2}\ \pi\ m_n^{*3/2}}{h^3}\frac{\sqrt{\varepsilon-\varepsilon_c}}{(1 + e^{(\varepsilon-\varepsilon_f)/kT})}d\varepsilon \quad ; \ (\varepsilon>\varepsilon_c) \qquad (9)$$

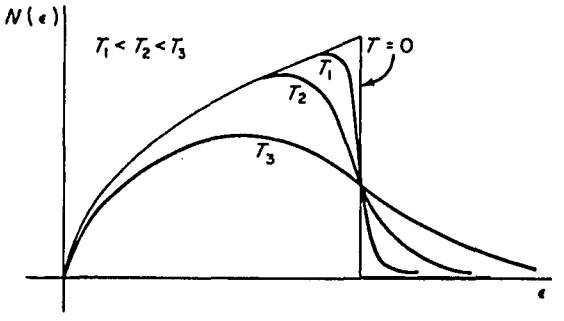

Figure 5. Schematic representation of electron density as a function of energy for a three-dimensional free-electron gas. (After McKelvey, p. 154).

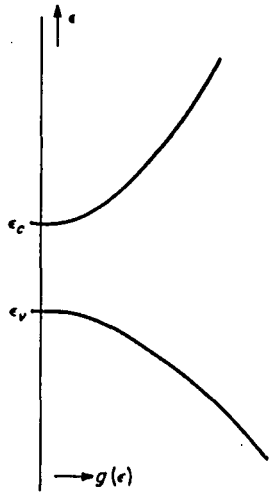

Figure 6. Density of states function for an intrinsic semiconductor. (After McKelvey, p.260).

and for holes where,

$$f_p(\varepsilon) = 1 - f_n(\varepsilon) = 1 - \frac{1}{1 + e^{(\varepsilon-\varepsilon_f)/kT}}$$

$$= \frac{1}{1 + e^{(\varepsilon_f-\varepsilon)/kT}} \tag{10}$$

$$dp = N(\varepsilon)d\varepsilon = g_v(\varepsilon)f_p(\varepsilon)d\varepsilon$$

$$= \frac{8\sqrt{2}\,\pi\, m_p^{*\,3/2}}{h^3} \frac{\sqrt{\varepsilon_v-\varepsilon}}{(1 + e^{(\varepsilon_f-\varepsilon)/kT})}\, d\varepsilon \quad ; \quad (\varepsilon<\varepsilon_v) \tag{11}$$

with the resulting electron and hole densities for intrinsic semiconductors and extrinsic semiconductors given by Figures 7 and 8, respectively.

As it happens, the range for the band gap, $\Delta\varepsilon$, is about leV, while the value for kT at 300°K is about .025eV. If the Fermi energy level in the band gap is at least a few kT away from either band edge ($\varepsilon_c-\varepsilon_f >> kT$, $\varepsilon_f-\varepsilon_v >> kT$), then the exponential part of the denominator of the Fermi distribution function is much greater than unity and equation (5) becomes,

for electrons:

$$f_n(\varepsilon) \simeq e^{-(\varepsilon-\varepsilon_f)/kT} \tag{12}$$

for holes:

$$f_p(\varepsilon) \simeq e^{-(\varepsilon_f-\varepsilon)/kT} \tag{13}$$

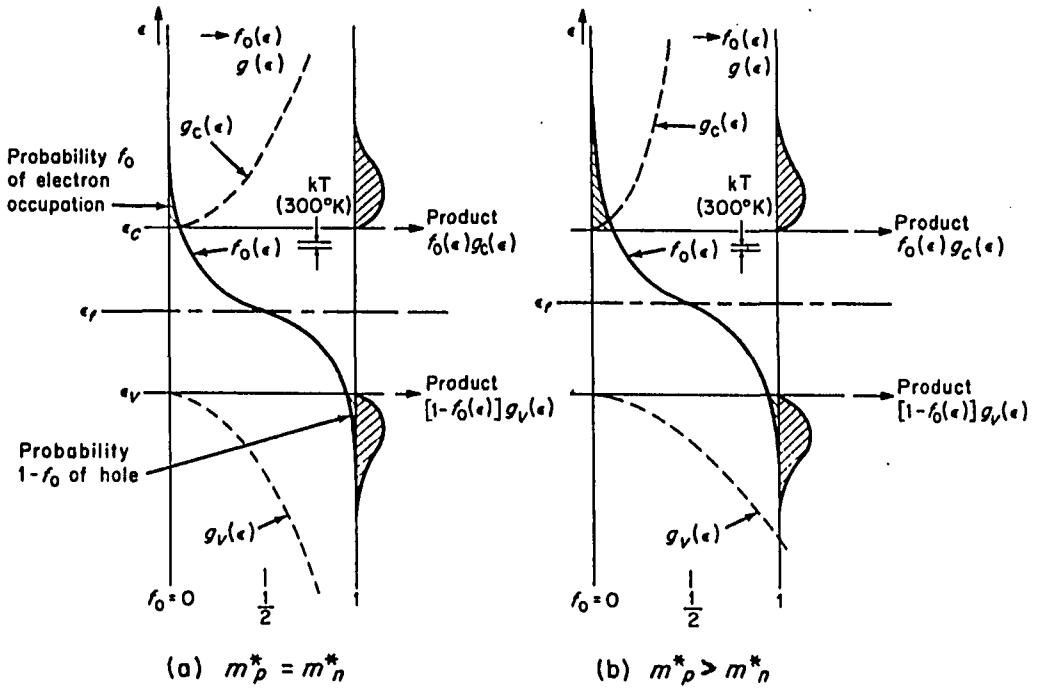

Figure 7. Distribution function, Fermi level, density of states function and electron and hole populations for an intrinsic semiconductor (a) where $m^*_p = m^*_n$ and (b) where $m^*_p > m^*_n$. Note the Fermi level moving up. (After McKelvey, p. 261).

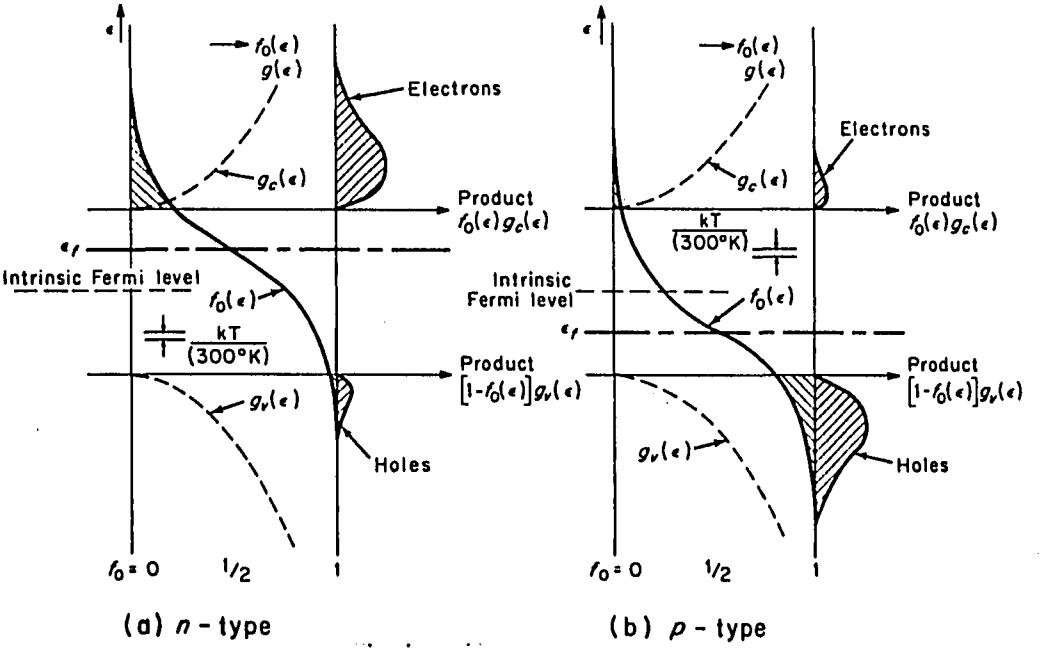

Figure 8. Distribution function, Fermi level, and electron and hole populations for (a) an n-type and (b) a p-type impurity semiconductor. (After McKelvey, p. 263).

which is of the form of a Maxwell-Boltzmann distribution and is called the Boltzmann approximation. The validity of this approximation, i.e. of ignoring the Pauli Exclusion Principle, is apparent at high temperatures where there are so many available energy states that the probability of having two particles in the same quantum state becomes negligible.

The total number of particles per unit volume can now be determined for electrons in the conduction band by integrating equation (9) from ε_c to ∞ .

$$n = \int_{\varepsilon_c}^{\infty} dn = U_c e^{-(\varepsilon_c - \varepsilon_f)/kT} \tag{14}$$

where

$$U_c = 2(2\pi m_n^* kT/h^2)^{3/2} \tag{15}$$

Similarly, for holes in the valence band, integration of eq. (11) over the range $-\infty$ to ε_v yields

$$p = \int_{-\infty}^{\varepsilon_v} dp = U_v e^{-(\varepsilon_f - \varepsilon_v)/kT} \tag{16}$$

where

$$U_v = 2(2\pi m_p^* kT/h^2)^{3/2} \tag{17}$$

Regardless of whether a semi-conductor is intrinsic (n=p) or extrinsic (n≠p), the product, np, will be a function only of the energy gap and the temperature,

$$np = n^2(T) = U_c U_v e^{-(\varepsilon_c - \varepsilon_v)/kT}$$
$$= U_c U_v e^{-\Delta\varepsilon/kT} \tag{18}$$

where $n(T)$ is the number of particles per unit volume at temperature T so that

$$n(T) = 2[2\pi(m_p^* m_n^*)^{1/2} kT/h^2]^{3/2} e^{-\Delta\varepsilon/2kT} \tag{19}$$

When an electric field, $\vec{E}$, is applied and a current flows, the electron current density, $\vec{I}_n$, is given by

$$\vec{I}_n = ne\mu_n \vec{E} \tag{20}$$

and the hole current density, $\vec{I}_p$, by

$$\vec{I}_p = pe\mu_p \vec{E} \tag{21}$$

with e the particle charge, and μ_n, μ_p the electron and hole mobilities defined as

$$\mu_n = e\bar{\tau}_n/m_n^* = e\ell/m_n^*\bar{\nu}_n \tag{22}$$

and

$$\mu_p = e\bar{\tau}_p/m_p^* = e\ell/m_p^*\bar{\nu}_p \tag{23}$$

where $\bar{\tau}$ is the weighted average for the relaxation time (time between scattering collisions) over the Maxwell-Boltzmann distribution, ℓ is the mean free path, and $\bar{\nu}$ is the average drift velocity.

The total current becomes

$$\vec{I} = e(n\mu_n + p\mu_p)\vec{E} = \sigma\vec{E} \tag{24}$$

where, σ , the conductivity is defined by

$$\sigma = e(n\mu_n + p\mu_p) \tag{25}$$

For an intrinsic semiconductor , $n = p = n_i$:

$$\sigma = en_i(\mu_n + \mu_p) = 2e(\mu_n + \mu_p)[2\pi(m_n^* m_p^*)^{1/2} kT/h^2]^{3/2} e^{-\Delta\varepsilon/2kT}$$

$$= \sigma_0 e^{-\Delta\varepsilon/2kT} \tag{26}$$

so that,

$$2.3 \log \sigma = -\frac{\Delta\varepsilon}{2k}\left(\frac{1}{T}\right) + 2.3 \log \sigma_0 \tag{27}$$

and a plot of log σ vs. 1/T yields a straight line (Figure 9) from whose slope $\Delta\varepsilon$ can be determined.

Note that σ_0 was treated as a constant independent of temperature, despite the $T^{3/2}$ dependence in σ_0 . This is because the mobility depends primarily on scattering due to thermal vibrations as a function of $T^{-3/2}$ (ref. 10) which cancels out the other T term [9] .

The expression for σ in the case of extrinsic semiconductors is somewhat more complicated, but at room temperature and above, it behaves (Figure 10) like the expression for an intrinsic semiconductor.

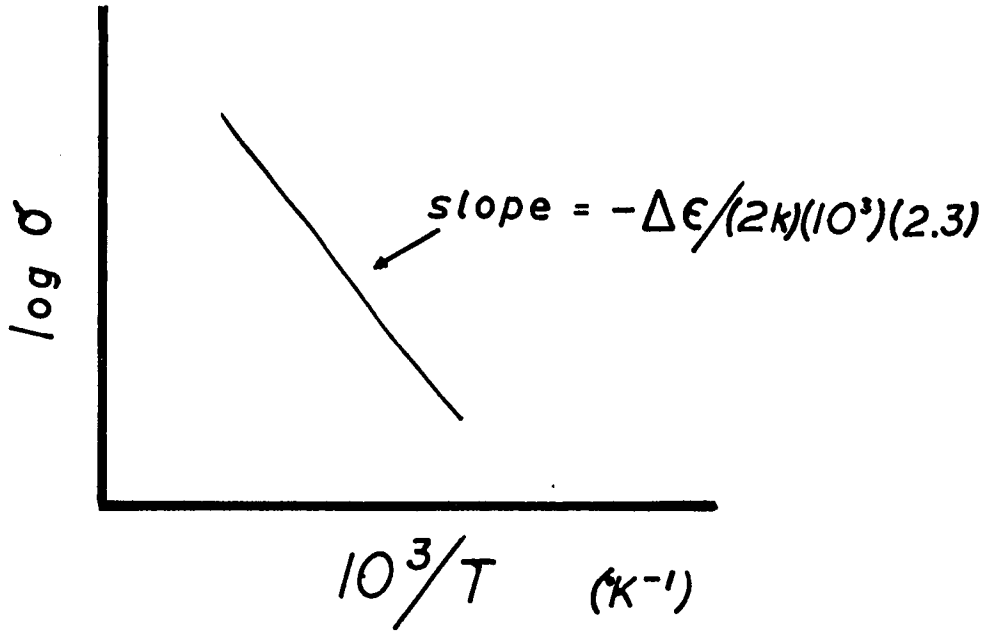

Figure 9. Temperature dependence of conductivity for an intrinsic semiconductor.

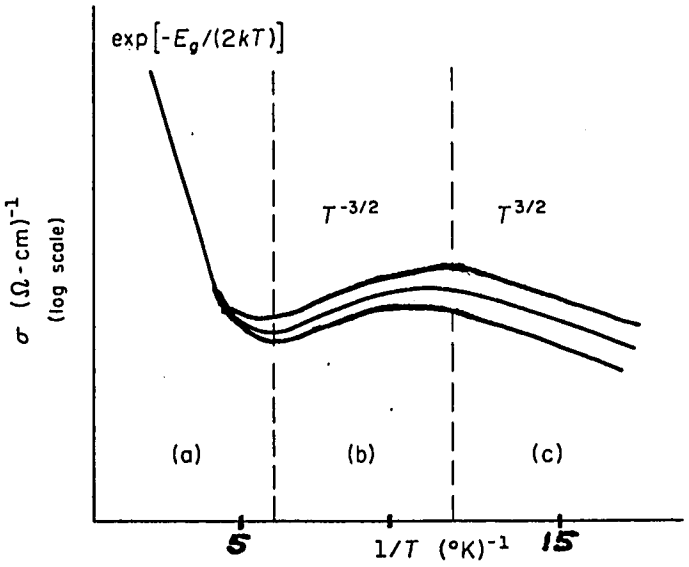

Figure 10. Temperature dependence of conductivity for an extrinsic semiconductor at (a) intrinsic region, (b) extrinsic region with lattice scattering dominant, (c) extrinsic region with impurity scattering dominant. The different curves represent different doping levels.

2. Hopping Mechanism

The other electronic model for conductivity involves a *hopping* mechanism[9,13,14] common to transition metal oxide semiconductors such as Fe_2O_3 and NiO[15], and probably present in organic molecular crystals like anthracene and naphthalene. In a transition metal oxide, there are a few metal ions of a different oxidation state interspersed in the lattice. When a field is applied, the extra electron can get across the potential barrier by either tunnelling (under certain conditions), or more often by picking up energy from interaction with a phonon and moving over the barrier to another ion. The latter process is thermally activated and is known as hopping.

Hopping mechanism: $Fe^{+2} - O - Fe^{+3} \rightarrow Fe^{+3} - O - Fe^{+2}$

The primary evidence for a hopping mechanism is a very low mobility, $< 5\ cm^2 \cdot volt^{-1} \cdot sec^{-1}$, and consequent short mean free path $\ell \leq a$, 3-5 Å (as compared to $\mu > 100\ cm^2 \cdot v^{-1} \cdot sec^{-1}$, with ℓ greater than the carrier wavelength, $h(2\pi mkT)^{-\frac{1}{2}}$, the situation found in the crystalline band model where ℓ gets as large as 10^4 Å)[16]. This indicates a large degree of influence on a particle's motion by individual atomic potentials giving rise to *localized energy states* where the probability amplitude of the wavefunction for a state decreases exponentially with distance away from the state[8], unlike the uniform potential that results in the free particle motion of the band model.

Because the "hops" depend on the energy exchanged with the vibrating lattice atoms, the probability for a transition depends on a Boltzmann distribution. The mobility is therefore exponentially dependent on temperature, and consequently, the conductivity would be given by

$$\sigma = \sigma' e^{-\Delta W/kT} \tag{28}$$

where σ' is related to the vibrational frequency, the angle of hopping relative to the field, the number of neighboring sites, and the interatomic spacing, all of which affect the mobility; ΔW is the energy barrier height, i.e. the energy between a pair of localized states. A plot of log σ against 1/T is linear as in the case of the band model, so that Equation (28) is analogous to, but not the same as, Equation (26).

B. Conduction in Non-Crystalline Material

Despite the fact that both mechanisms for conductivity were developed for crystalline materials, long-range order is not a necessary condition for their validity - certainly not in the hopping mechanism, but not even in the band model. Besides, some form of band gap must exist, otherwise ordinary optical glass would not be transparent[16].

Many solid crystalline materials retain linear conductivity temperature dependence as they go past their melting point and lose their long-range order. Ioffe and

Regel showed that short-range order up to 10^4 Å still exists on transition from the solid to the liquid state enabling electrical properties to remain the same despite the phase change. Occasional sharp differences are due primarily to density changes as a result of coordination number changes rather than to loss of long-range order [17].

In non-crystalline materials, all the atoms have their local valence requirements satisfied [18]. The atoms immediately surrounding any one atom and their relative positions, i.e. the first coordination number, are the same in elemental and binary amorphous semiconductors as they are in the corresponding crystalline forms [17]. In ternary and higher alloys they may vary more randomly. However, the energy bands depend primarily on the first coordination number and the idea of extended states in valence and conduction bands remains valid with the compositional and translational disorder acting as a perturbation [18,19,21]. The more distorted the bond lengths or angles are, the more localized the resulting states will be. However, increasingly larger distortions become less probable, so that the density of states decreases exponentionally with increasing energy, tailing off from the valence and conduction band edges into the forbidden energy region [22].

Cohen, Fritzche and Ovshinsky (CFO) view the *tail* of localized states (Figure 11) as moderate in elemental semiconductors such as amorphous Ge [20], and extensive to the point of band overlap (Figure 12) in alloys with both

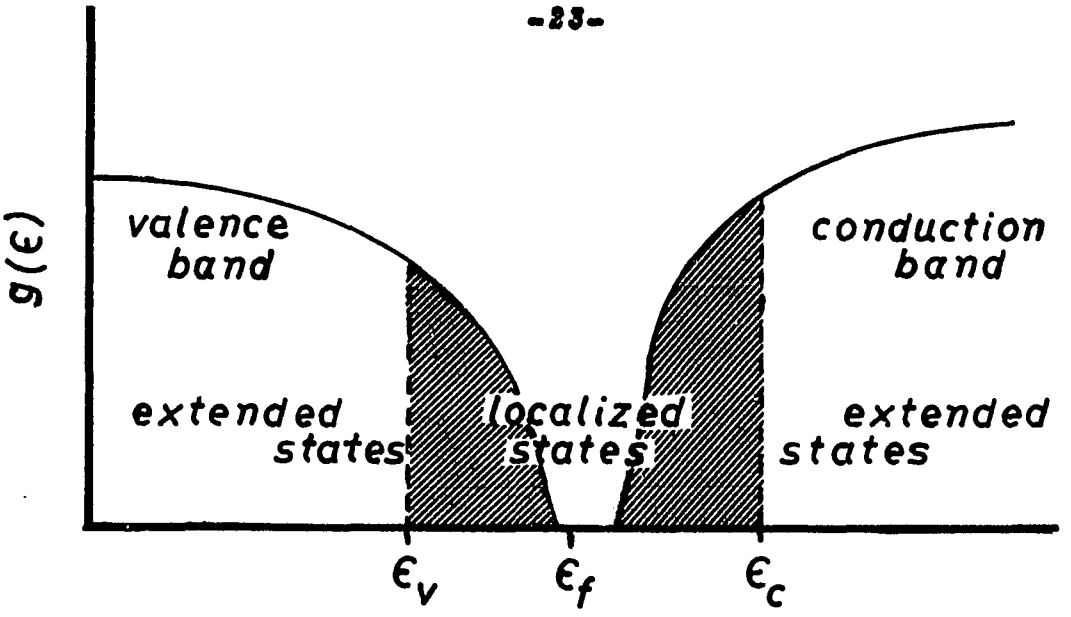

Figure 11. Density of states function for a single element amorphous semiconductor.

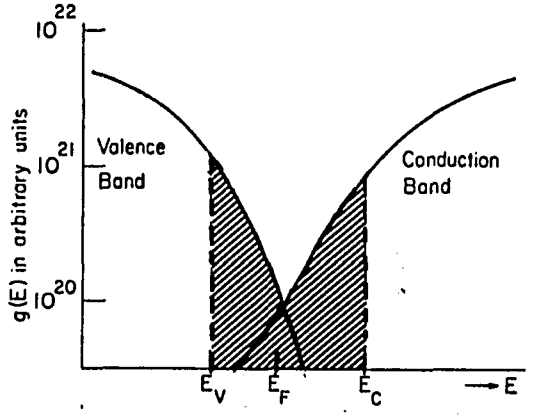

Figure 12. Density of states function for a multi-element amorphous semiconductor.

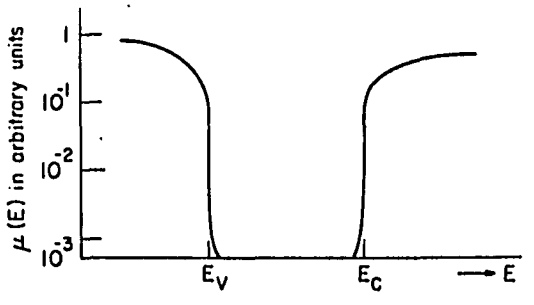

Figure 13. Mobility function for an amorphous semiconductor.

compositional and translational disorder [19].

A direct result of localization is the creation of mobility edges at ε_v and ε_c (Figure 13), where the band edges in crystalline semiconductors were. These mark the sharp transition from a continuum of non-localized or extended states where the particles can have a relatively high mobility to the localized states where the mobility drops by a factor of ~ 1000 and particle motion depends on phonon assistance [19,14].

These mobility edges serve to explain the existence of a well defined activation energy, $\Delta\varepsilon$, despite the lack of sharp band edges; the energy gap is replaced by a *mobility gap*.

Because the tails of the valence and conduction bands overlap, electrons in higher energy states of the valence bands can drop down to fill empty lower energy states in the conduction band tail. Since valence band states are normally filled, and conduction band states normally empty, the repopulation results in the formation of positively charged states in the valence band edges and an equal number of negatively charged ones in the conduction band. These charged states maintain the integrity of the individual band edges so that they cannot be plotted as a combined density of states. Because they are charged, these localized states act as *traps*, either shallow or deep depending on their energies, which will affect conductivity by limiting the carrier mobility.

In addition, these charged states affect the Coulombic potential, altering the energies of all states so that occupation of the tail states becomes a self-consistent field problem [19].

Although theoretical calculations are not yet up to the complexity involving the high degree of compositional and translational disorder present in the chalcogenide glasses, certain experimental evidence supports the CFO theory. Intrinsic conductivity can occur across the mobility gap at higher temperatures, while hopping in the localized states occurs at low temperatures. That p-type conduction is the case at all glass compositions is probably due to the fact that the conduction band tail, coming off a higher energy and therefore wider band, is spread out more than the valence band tail (note Fig. 12). The Fermi energy, ε_f , lies pinned between the overlapping band tails but closer to ε_v as a result of shifting to compensate for additional conduction band tail states becoming filled. In intrinsic conduction, the number of holes is proportional to $e^{-(\varepsilon_f-\varepsilon_v)/kT}$ (eq.16), while the number of electrons depends on $e^{-(\varepsilon_c-\varepsilon_f)/kT}$ (eq.14). Since $\varepsilon_f-\varepsilon_v < \varepsilon_c-\varepsilon_f$, holes will be the dominant current carriers. This remains the case even when doping with n-type material. In a crystalline lattice, the introduction of a donor atom with an extra electron results in the formation of a dangling bond, i.e. the extra electron is nonbonding and becomes available as a current carrier; in amorphous materials, where the disorder allows all local valence bonding require-

ments to be fulfilled, the extra electrons are tied up in bonding. Therefore, impurities do not affect the conductivity except in concentrations large enough to affect the short-range order. Kolomiets found that zone refining does not affect the conductivity in vitreous systems of arsenic-sulfide and arsenic-selenide[1].

Similarly, high radiation fields will break bonds, forming donor states; however, the donors will be in the valence band tail and can repopulate downward in energy, dropping into empty valence states immediately below them, as well as into unfilled conduction band tail states. The effect will be to shift ε_f a little to $\varepsilon_f + \Delta\varepsilon_f$ but will not change the conductivity considerably, as it would in the formation of a high density of donor states in a crystalline semiconductor[20]. And finally, dark photoconductivity measurements at low temperatures ($77^\circ K$) indicate the probable existence of immobile traps above and below ε_f, the kind that would be formed by the charged states resulting from the CFO theory[19].

Although in agreement on most points, Mott and Davis dislike the idea of extensive band overlap. Instead, they prefer a narrow band (<.1eV) of localized states situated in the middle of the mobility gap, in addition to the localized states in the band tails (Fig. 14-d)[47].

Note that here too the conduction tail is wider than the valence tail resulting in $\varepsilon_f - \varepsilon_v < \varepsilon_c - \varepsilon_f$ and giving p-type

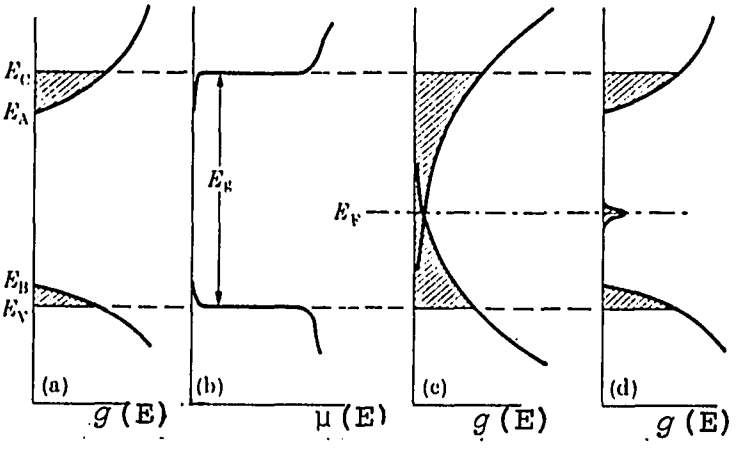

Figure 14. Density of states and mobility as functions of energy in amorphous semiconductors. (After Mott and Davis, *Electronic Processes in Non-Crystalline Materials*, Oxford University Press, London, 1971, p. 199).

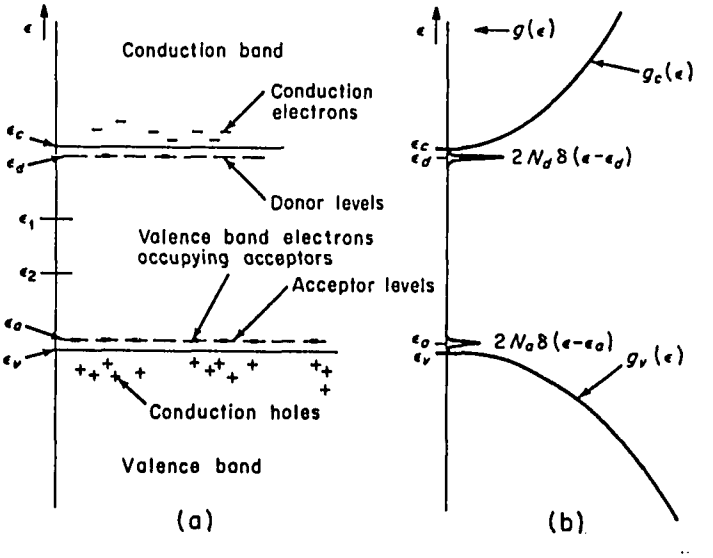

Figure 15. (a) Energy band diagram of an impurity semiconductor, showing donor and acceptor levels; (b) corresponding density of states curve. (After McKelvey, p. 269).

conduction. Also, the central band contains a high enough density of states to effectively pin the Fermi energy over a wide temperature range, as in the CFO theory (Fig. 14-c). Mott and Davis conclude that a model of this sort better accounts for the high transparency of amorphous glasses at photon energies below the absorption edge [14].

The idea of a continuum of localized energy states in the band gap is not new. In extrinsic crystalline semiconductors, impurity states have their energy levels in the forbidden energy gap, represented in figure 15 by delta "spike" functions [7].

When there is a high concentration of donor and acceptor states in relatively equal amounts, as in a *compensated semiconductor*, their wave-functions will overlap appreciably, resulting in the broadening of the levels into a narrow band. At low temperatures ($< 30^{\circ}K$) where electrons and holes are "frozen out" of the valence and conduction bands, they will occupy the impurity band and exhibit conduction by a hopping mechanism. This is in line with the concept that a narrow band implies high effective mass; consequently, the particles will have a low mobility determined by

$$\mu = \mu_0 e^{-\Delta W/kT} \tag{29}$$

where ΔW is the potential barrier height between the localized states [16]. This situation probably prompted Marshall and Owen [59] to model their density of states function along similar lines

and arrive at Figure 16(d) as their model for amorphous semiconductors.

From the work of Anderson[23] and Twose[24], Mott concluded that for a completely randomized linear chain of delta functions (the case of a disordered Kronig-Penney model) all the solutions are localized[18]. In the case of a non-crystalline semiconductor, although most local valence bonding requirements are fulfilled, there may be a few impurities such as dangling bonds, interstitial atoms, etc. depending on the method of formation and subsequent annealing, which give rise to the central band of localized states. Conduction determined by this band would be an example then of extrinsic conduction in a non-crystalline semiconductor[14]. This revised model is illustrated in Figure 16(c), juxtaposed next to the other three models proposed to describe the density of states in non-crystalline semiconductors.

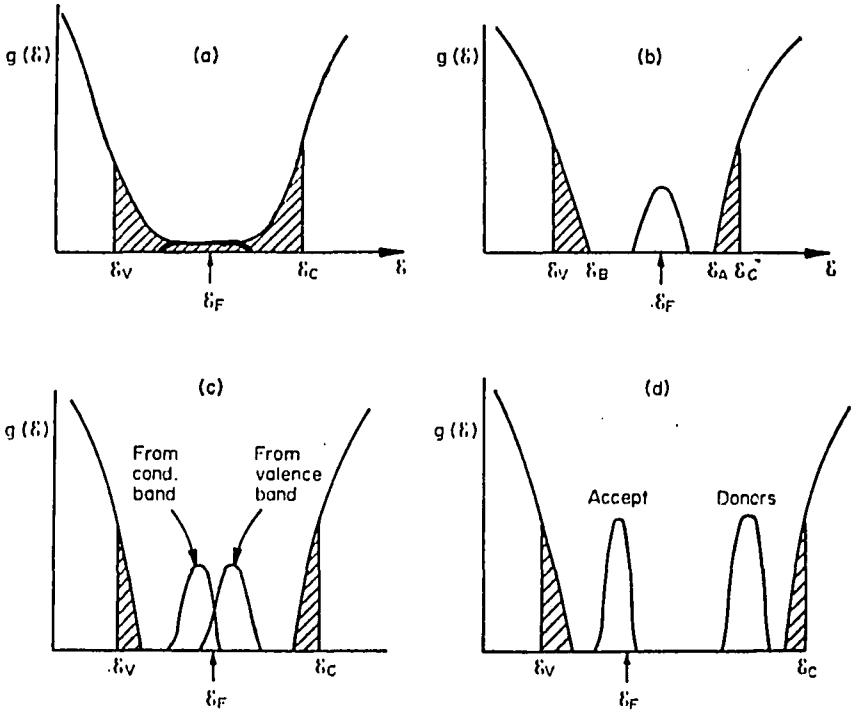

Figure 16. (a) CFO model (ref. 19); (b) Mott and Davis model (ref.14); (c) Mott model revised (ref. 60); (d) Marshall and Owen model (ref. 59).

III. EXPERIMENTAL BACKGROUND

Studies of some amorphous structures can be carried out on both bulk and thin-film samples. Bulk samples are readily obtained by mixing the elements in powdered form in the desired composition and heating to a temperature above that of the highest melting component. Rapid quenching results in glass formation, if the glass forms at that composition [25,26].

Thin films are achieved by either thermally controlled evaporation of a sample onto a substrate or by sputtering techniques. Evaporation is a quicker and cheaper method but has the problem of fractional distillation to overcome in the preparation of multicomponent samples [27].

Not all materials yield glasses by both methods. Germanium and tellurium cannot be formed in an amorphous structure in bulk form, regardless of the rapidity of quenching [78]. In thin-film form, Ge also crystallizes above 3μm (30,000 Å), while Te must be deposited on a substrate kept below 77°K to keep it from crystallizing.

The short-range order structure of amorphous glasses is usually found to be the same as the structure of their crystalline counterparts. The same coordination number with other atoms occasionally substituted is common. However, all atoms are bonded covalently to the number of atoms required by their Group number. Group IV Ge is tetrahedrally linked no matter where it finds itself, while Group VI Se and Te

have two bonds each. Both Se and Te form isomorphous hexagonal structures in the crystalline state and exist as chains in the melt (with some Se_8 ring structures as well). Te can therefore replace Se atoms easily, though forming weaker Se-Te bonds than Se-Se. In the vitreous phase, some of the bond angles vary somewhat (<15°) from their crystalline norms resulting in a corrugated or puckered layer structure [28]. Ge-Se and Ge-Te have the structures of black phosphorous and metallic arsenic respectively, both layered systems[29]. The addition of Ge in ternary systems results in interlocking tetrahedra cross-linking the chain laminate layers, consequently increasing the microhardness and glass transition temperature (softening point)[1].

Although the energy in a non-crystalline state is higher than in a crystalline state, making an amorphous structure a metastable condition which may crystallize when the temperature is raised beyond the softening temperature, once formed, the glass is stable for long periods of time (3 years in our lab) without change in its electrical characteristics.

Recalling Mott's density of states model for amorphous semiconductors (figure 14), there are three types of mechanisms that can occur to give electrical conduction [14].

(a) Electrons excited from the non-localized states below the valence mobility edge to those above the conduction mobility edge leaving holes behind in the extended states

of the valence band. This is analogous to the situation in an intrinsic crystalline semiconductor.

(b) Electron excitation into the localized conduction band tail to give n-type current or excitation from the localized band tail leaving holes to carry a p-type current. Conduction will be by hopping between localized states near the band tail edges, with the current carriers being the particles with the higher mobility.

(c) Conduction carried by hopping between localized states within the narrow band in the middle of the mobility gap. This is analogous to the conduction in heavily doped compensated crystalline semiconductors.

Since the conductivity depends on the mobility (eq. 25), and the mobility varies in the different mechanisms, the total conductivity will include a term for the variation of the mobility with energy $\mu(\varepsilon)$, in addition to the terms for density of states, $g(\varepsilon)$ and distribution function, $f(\varepsilon)$ [30],

$$\sigma = e \sum_{b=c,v,d} \int g_b(\varepsilon)\mu_b(\varepsilon)f_b(\varepsilon)d\varepsilon \qquad (30)$$

where b is a band index, with $c, v,$ and d labelling the conduction, valence and defect bands respectively.

For the different processes where current is carried in the conduction band's extended states, process (a),

localized states (b), or in the central band (c), the variation of the conductivity as a function of energy, $\sigma(\varepsilon)$ depends on the temperature as illustrated by Figure 17.

Experiments to determine the electronic properties of chalcogenide glasses are similar to those designed for crystalline semiconductors, but modified to resolve difficulties caused by the glasses' small conductivities, 10^{-3}-10^{-13} $ohm^{-1} \cdot cm^{-1}$.

A. D.C. Conductivity

The variation of conductivity as a function of temperature yields information directly about the energy gap as well as indirect information about the carrier mobility and effective mass (eq. 26)[14].

(a) For the intrinsic mechanism, in the case of a current carried by holes, as is the case in chalcogenides, the conductivity is given by,

$$\sigma = \sigma_o e^{-(\varepsilon_f - \varepsilon_v)/kT} \tag{31}$$

with σ_o independent of temperature.

(b) For carrier conduction at the band tail edge, the conductivity becomes

$$\sigma = \sigma'_o e^{-(\varepsilon_f - \varepsilon_b + \Delta W)/kT} \tag{32}$$

where ΔW is the activation energy for hopping and ε_b is the energy at the band edge. σ'_o is smaller than σ_o primarily

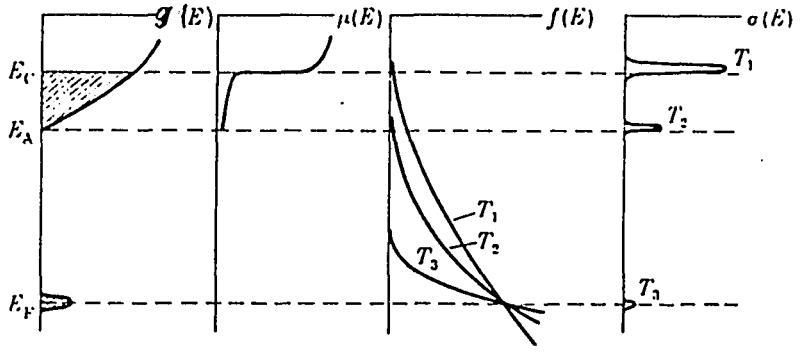

Figure 17. Illustration of the effect of temperature on the mode of conduction. (After Mott and Davis, p. 202).

$\sigma(E) = eg(E)\mu(E)f(E)$; $T_1 > T_2 > T_3$

because of the smaller mobility associated with a hopping mechanism.

(c) When a hopping process occurs between nearest pairs of localized states near the Fermi energy,

$$\sigma = \sigma_o'' e^{-\Delta W'/kT} \tag{33}$$

with $\sigma_o'' < \sigma_o'$, and $\Delta W'$ is of the order of half the width of the central band in Figure 14 (d).

(d) At lower temperatures, when carriers tunnel between more distant states in the central localized band, the process is no longer activated and log σ is no longer linear with $1/T$; instead,

$$\ln \sigma = A - BT^{-1/4} \tag{34}$$

where B is a function dependent on the slight degree of overlap between wave-functions for distant sites.

The plot of $\ln \sigma$ vs. $1/T$ for the four cases is illustrated in Figure 18 and is based on the model of Figure 17.

B. A.C. Conductivity

Though more difficult to measure because of shielding problems caused by lead geometries, as well as electronic circuitry limitations, the a.c. conductivity as a function of temperature and as a function of frequency helps differentiate between the possible mechanisms[14].

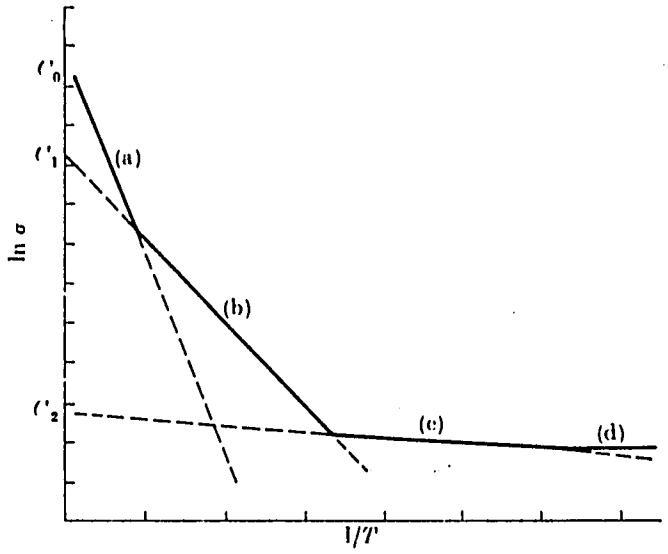

Figure 18. Schematic representation of the temperature dependence of the four conduction mechanisms described in the text. (After Mott and Davis, p. 203).

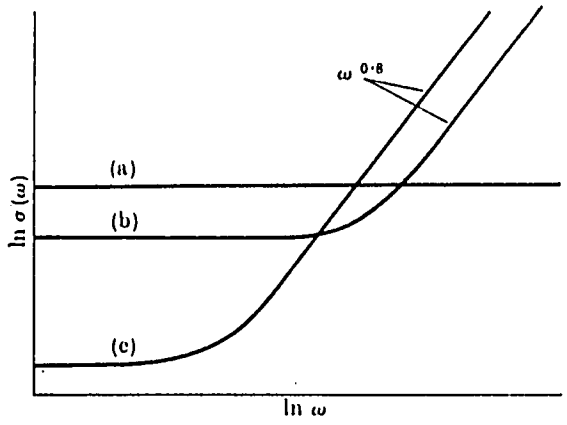

Figure 19. Schematic illustration of the frequency dependence of three of the conduction mechanisms described in the text. (After Mott and Davis, p. 213).

(a) For intrinsic type conduction, the conductivity as a function of frequency, $\sigma(\omega)$ is given by,

$$\sigma(\omega) = \frac{\sigma(0)}{1 + \omega^2\tau^2} \tag{35}$$

where τ is the relaxation time. Although this dependence, the Drude formula, was derived for liquid metals where $\tau \simeq 10^{-15}$ sec, it is applicable to solid non-crystalline materials, though τ is somewhat longer. In either case, ω would have to be about $10^8 - 10^{10}$ Hz before $\sigma(\omega)$ differs from $\sigma(0)$, the d.c. conductivity. Its temperature dependence would also contain the same exponential term as σ in equation (31), $\propto e^{-(\varepsilon_f - \varepsilon_v)/kT}$.

(b) For conduction along the band edge by hopping, Mott derives the relationship,

$$\sigma(\omega) \propto \omega[\ln(\nu_{ph}/\omega)]^4 \simeq \omega^{0.8} \qquad (\omega << \nu_{ph}) \tag{36}$$

where ν_{ph} is the phonon vibration, taken to be about 10^{12} Hz. The temperature dependence of $\sigma(\omega)$ for this process is again the same as for the d.c. conductivity, $\sigma' \propto e^{-(\varepsilon_f - \varepsilon_b)/kT}$ (in the case of hole conduction).

(c) Hopping in the defect band in states near the Fermi energy will give rise to an $\omega^{0.8}$ dependence of the form,

$$\sigma(\omega) = \tfrac{1}{3}\pi e^2 kT[g(\varepsilon_f)]^2\alpha^{-5}\omega[\ln(\nu_{ph}/\omega)]^4 \qquad (\omega << \nu_{ph}) \tag{37}$$

where $g(\varepsilon_f)$ is the density of states at the Fermi energy, and α^{-1} is the length for exponential decay of the wave-

function amplitudes for the states[31]. In this mechanism, $\sigma(\omega)$ will no longer be exponentially dependent on T, but will be proportional to T if $kT << J$, the defect band width, and independent of T otherwise.

The three processes will follow the scheme presented in Figure 19 with the primary difference between mechanisms (b) and (c) being in the $\sigma(\omega)$ temperature dependence.

C. Thermoelectric Power

Measurement of the Seebeck coefficient, S yields information directly about the type of carrier that predominates in the conduction process,

$$S = \Delta V/\Delta T \tag{38}$$

where ΔV is the voltage developed between two sample-lead junctions held at slightly different temperatures, ΔT. The sign of the voltage indicates the sign of the mobility carrier. After correction for the absolute thermoelectric power of the lead wire, the Seebeck coefficient for hole conduction is given by,

$$S = \frac{k}{e}\left(\frac{\varepsilon_f - \varepsilon_v}{kT} + A\right) \tag{39}$$

where A is a small constant, taken to be about unity for non-crystalline semiconductors; AkT is the average energy of the holes formed with respect to the valence mobility edge, i.e. the width of the energy band below the valence mobility

edge where holes will be formed ($\varepsilon_f - \varepsilon_v >> kT$). A plot of S vs. $1/T$ yields information about the mobility gap for conduction by process (a), or energy $\varepsilon_f - \varepsilon_\beta$ for process (b)[14].

Although the Hall voltage (a voltage generated perpendicular to mutually perpendicular magnetic and electric fields) serves as the prime indicator of the majority carrier in crystalline semiconductors, its value in non-crystalline materials is dubious. The Hall mobilities turn out to be extremely small, $10^{-1} cm^2 V^{-1} sec^{-1}$, about the experimental limit of measurement, and seem to be independent of temperature where they shouldn't be; the Hall coefficient is paradoxically always of opposite sign than the Seebeck coefficient[32,48]. Thermoelectric power measurements are, therefore, relied on to determine the type of carrier.

D. Optical Absorption

The absorption spectrum of a crystalline semiconductor is characterized by a rapid increase in the absorption coefficient α, at an energy corresponding to the energy gap as in Figure 20.

The absorption coefficient at any photon energy can be determined by measuring the transmittance, T, and reflectance, R, of a sample and solving for α from

$$T = \frac{(1 - R)^2}{e^{\alpha x} - R^2 e^{-\alpha x}} \simeq (1 - R)^2 e^{-\alpha x} \tag{40}$$

$$R = \frac{(n - 1)^2}{(n + 1)^2} \tag{41}$$

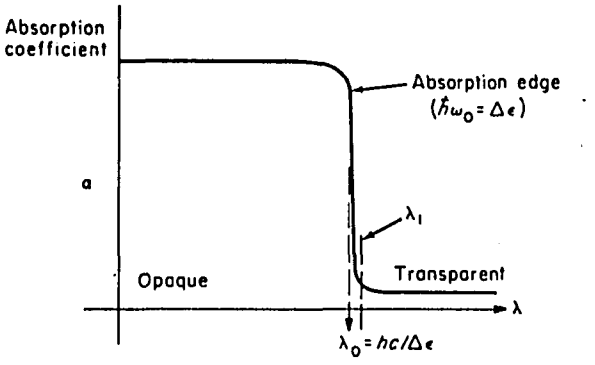

Figure 20. Absorption spectrum of a typical crystalline semiconductor showing an absorption edge. (After McKelvey, p. 321).

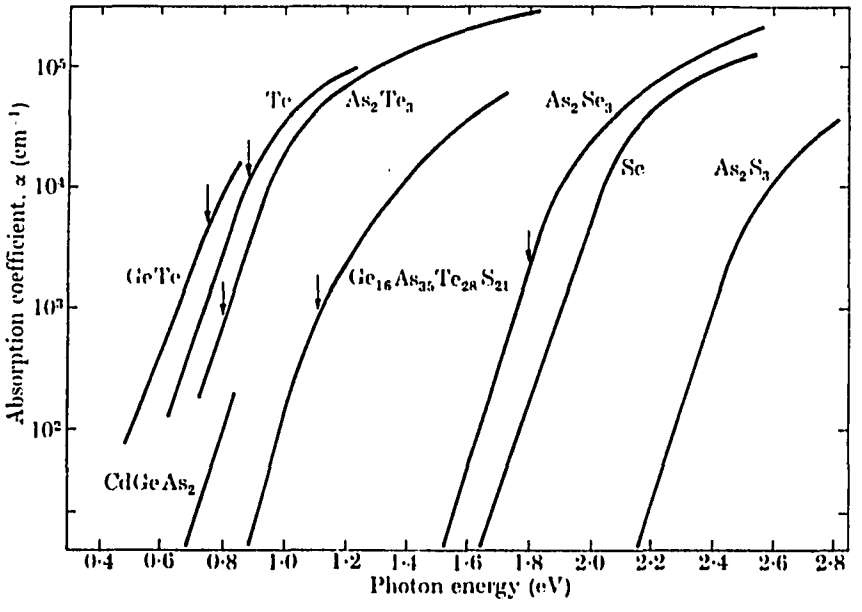

Figure 21. Exponential absorption edges in amorphous semiconductors at room temperature. (After Mott and Davis, p.244).

where x is the sample thickness and n is the index of refraction[33].

Unfortunately, the increase in absorption coefficient as a function of energy does not occur sharply in glass semiconductors as it does in crystalline ones. Rather, a plot of α vs. $\hbar\omega$ yields an exponential absorption edge spread over a few tenths of an eV. This type of dependence is common to many amorphous semiconductors (Fig. 21) and is given by the Urbach rule,

$$\alpha = \alpha_o e^{[\gamma(\hbar\omega - \Delta\varepsilon_o)/kT]} \tag{42}$$

where γ is a constant and $\Delta\varepsilon_o$ is the energy gap.

The exact energy at which an optical gap corresponding to the mobility gap can be said to occur varies among authors who try to fit the curve to various empirical equations representing different mechanisms for the transition[14,34]. Note the arrows in Figure 21 that indicate values for ε_o corresponding to twice the value of the energy term in the exponential conductivity dependence for an intrinsic process given in equation (31). This would be the case if $\varepsilon_f - \varepsilon_v = \varepsilon_c - \varepsilon_f$, i.e. if ε_f were in the center of the mobility gap.

E. Switching

One of the most valuable features common to many amorphous chalcogenides is their ability to be switched from a highly resistive state to a highly conductive one in a short time interval. Two types of switching have been characterized,

threshold and memory switching.

In a threshold monostable device, as an applied voltage across a thin bulk sample or thin film creates a field greater than 10^4 V/cm, the current becomes non-ohmic, rising exponentially with increasing voltage. At the threshold, V_T, the material becomes highly conductive and can be kept that way by maintaining a smaller holding voltage, V_H across the sample. When the holding voltage is removed, the current drops below a minimum I_H and the highly resistive state is restored (Fig. 22[a]). The threshold voltage is proportional to thickness and can vary over a large range (2-300 V); the larger V_T for a particular sample thickness, the shorter, exponentially, the switching time, going from a few μsec to ≃.5η sec. The holding voltage, on the other hand, is independent of thickness and varies over a range of .5 - 1.5 V.

If the applied voltage is in the form of a fairly long pulse (∿10 msec.) in excess of the threshold voltage, some chalcogenide compositions, especially those at the edge of the glass-forming region, will switch to the conductive state and remain there even after the removal of any holding voltage (Fig. 22[b]). This bistable memory device can be reset to the non-conductive state with a short (≃5μsec) high current (≃150ma) pulse[2,5].

Although known for some time to occur to some degree in a variety of materials[3-8], switching as it is found in chalcogenides was only first thoroughly investigated by S.R. Ovshinsky[3]. Working on a quaternary system of $Ge_{10}Si_{12}As_{30}Te_{48}$, he found threshold devices to be independent of polarity and

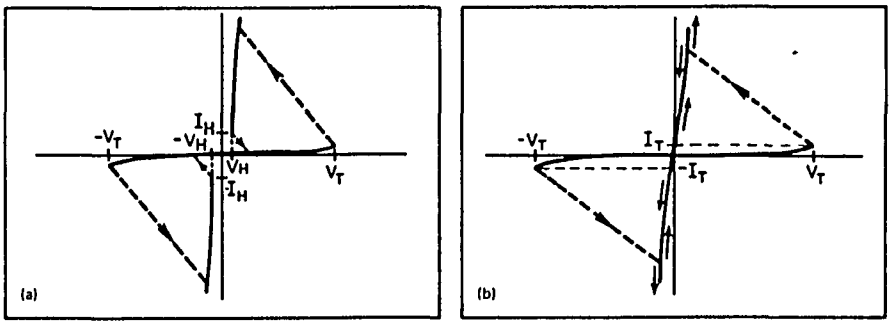

Figure 22. (a) Current-voltage characteristics of a typical current-controlled threshold device. The dotted lines are significant for their end points, showing the transitions made with a particular value of series resistance, as the total voltage applied to the series combination is varied. (b) Current-voltage characteristics of a memory device, showing bistability at V = I = 0.

able to retain their characteristics after 10^{13} switching events. Besides many practical applications of electrical switching[39,40], his colleagues at Energy Conservation Devices, Inc. have found that amorphous structures of $Ge_{15}Sb_2S_2Te_{81}$ undergo reversible laser induced switching, forming alloys transparent to red light in the high resistance state and opaque in the low resistance state, thus paving the way for many electro-optical applications[35].

There have been many mechanisms advanced to explain switching phenomena, some based on analogous processes in crystalline materials, such as Zener tunneling or avalanche breakdown, others on purely thermal effects caused by extremely rapid Joule heating[41]. The fact that switching effects in chalcogenides are unlike those observed in other materials suggests an electronic mechanism involving the localized states unique to these amorphous structures[20].

Based on the CFO theory that equal densities of positively and negatively charged trap states exist in the amorphous semiconductor, Henisch, Fagen and Ovshinsky (HFO) suggested a double injection space-charge model. As electrons are injected from the cathode and holes from the anode, they are trapped, building up a space-charge in the semiconductor near each electrode and distorting the internal field, As the current increases, the space-charges widen until they begin to overlap. The higher the applied voltage the less time it takes for the overlap to occur in a small region. At the point of overlap, all positive and negative traps are

filled and the resulting neutral region is highly conductive. As carriers begin to flow, the elecrtic field redistributes itself leading to further overlap and increased current flow until most of the region has become conductive. The conductive state is then sustained by double injection as long as a small holding voltage greater than the mobility gap is maintained[36]. This sequence is illustrated in Figure 23.

Fritzche and Ovshinsky (FO) have also proposed another mechanism similar to the HFO model, but suggesting that the excess injected carriers lead to the development of Schottky barriers within the semiconductor near each electrode as those local regions are depleted of electrons and holes. This occurs because the carriers injected from the electrodes are moving much more quickly than those in the semiconductor and cannot recombine with them, i.e. the transit time is much smaller than the recombination time. If this were not the case, space charges would be set up in other regions beyond the immediate area of the electrodes, leading to a space-charge limited current as in the HFO theory. Because of the high density of localized trap states, the entire Schottky space-charge can be accommodated within ≈30Å of the electrodes and the contact remains ohmic so that electrons can continue to tunnel into the conduction band at the cathode, while holes tunnel into the valence band at the anode. When all the traps get filled, the conductivity becomes high and remains high as long as the minimum voltage, V_H is maintained to keep injecting the carriers at both electrodes[37]. Mott, more

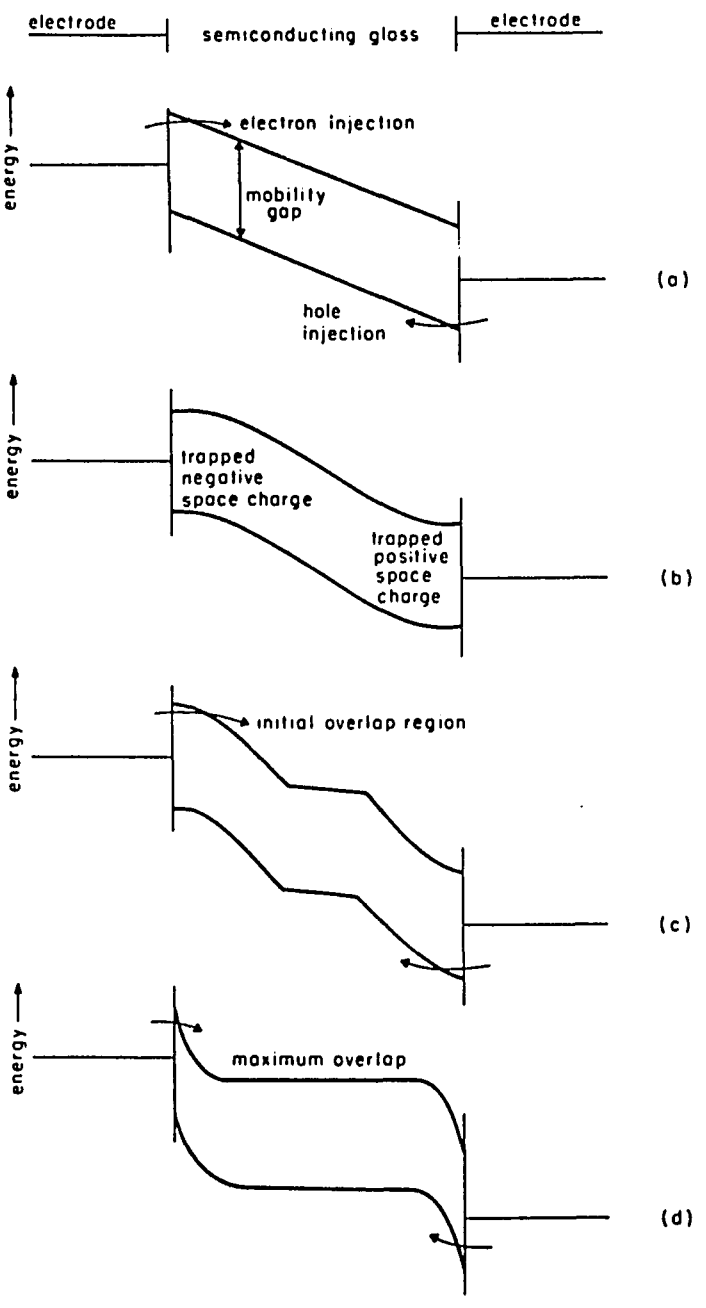

Figure 23. Sequence of events during threshold switching. (a) voltage applied: instantaneous situation. (b) space charges established on opposite sides. (c) beginning of space charge overlap; unstable situation. (d) maximum space charge overlap (as profiled by Mott).(After HFO, ref.36).

or less agrees with this model[16,42]. Again, the potential energy plotted against position across the film would result in Figure 23(d).

While some workers agree with this mechanism for threshold switching[61], more recent work has suggested a greater role for heating effects[62]. There is some heating occurring even in the threshold devices, especially the thicker ones (>8μm), and some evidence that temperatures rise sharply in local regions so that the resulting negative resistance plays a part in the switching[46]. However, threshold devices experience no sharp transitions in differential thermal analysis, so that structural changes are unlikely to affect the threshold mechanism, at least not in the thin films (≃1μm) studied by Ovshinsky's group where heating effects are minimal[37].

Kroll[63] combines both mechanisms into an elegant electrothermal one and calculates various parameters which describe how the mechanism would proceed for different materials and device geometries. Roosbroeck[64,65] prefers a single injection electronic mechanism for both thick and thin samples despite heating effects in the former, but contends that, in contrast to the HFO theory, carrier injection proceeds as it does in a relaxation semiconductor, characterized by a dielectric relaxation time greater than the recombination time. The key feature of this theory lies in that it proposes a "recombination front" at the anode during a switching event

accounting for observations that structural changes, when they occur, seem to proceed from the anode[66].

Impact ionization, a mechanism common to crystalline semiconductors, is another possibility for electronic switching, wherein carriers accelerated by a high field cause ionization that in turn creates more carriers. This sort of avalanching can also prompt Joule-heating which increases the carrier recombination time or diffusion-length lifetime by decreasing the time spent in traps. Field-assisted thermal ionization whereby the high field serves to lower the Coulombic potential barrier between localized states, thus freeing trapped carriers, is known to occur in some insulators as the Poole-Frankel effect, and has been proposed as another possibility to account for threshold switching.

The extent to which these mechanisms apply to non-crystalline materials and the degree to which their implications concur with experiment has recently been reviewed by Vezzoli, *et al*[67].

In memory devices the threshold voltage and its purpose remains, but is accompanied by extremely rapid Joule heating from the original higher voltage pulse ($>V_T$) which serves to break some of the weaker bonds, freeing valence electrons for conduction purposes, and rearranging the structure so that, as it cools relatively slowly, micro-crystalline conducting channels are formed. These channels function analagously to extrinsic crystalline semiconductors. Their existence is also justified by the fact that the alloys

showing memory capability are usually near the edge of the glass-forming region in the phase diagram, contain some percentage of cross-linking elements in their composition, and upon differential thermal analysis contain two distinct thermal transitions (Fig. 24). The first transition at T_1, an exothermic one, is associated with a phase separation and crystallization. The second transition at T_2 is endothermic and is correlated with melting. Cooling between the two transition temperatures yields the low resistance state, while slow cooling after the second transition (Fig. 24c) yields the polycrystalline state. Rapid quenching after the second transition (Fig. 24b) gives the high resistance glass[43]. In order to reset the memory device, therefore, a short high current pulse heats the microscopic conducting channel, and the cooler non-conducting environment serves to quench it back to the high resistance state. These heating filaments have been observed in both thick films by Pearson[38] and in bulk samples by others[44,45].

Filament formation is not necessarily restricted to memory devices but has been observed in threshold compositions as well[68,69]. This is to be expected in view of the evidence that the first few switching events of a virgin threshold device require higher voltages than subsequent operation[38]. V_H also decreases as the current passed in the ON-state increases[70]. It appears that some degree of structural ordering is initiated by the field, either directly or indirectly (thermally) creating microcrystalline domains which aid an

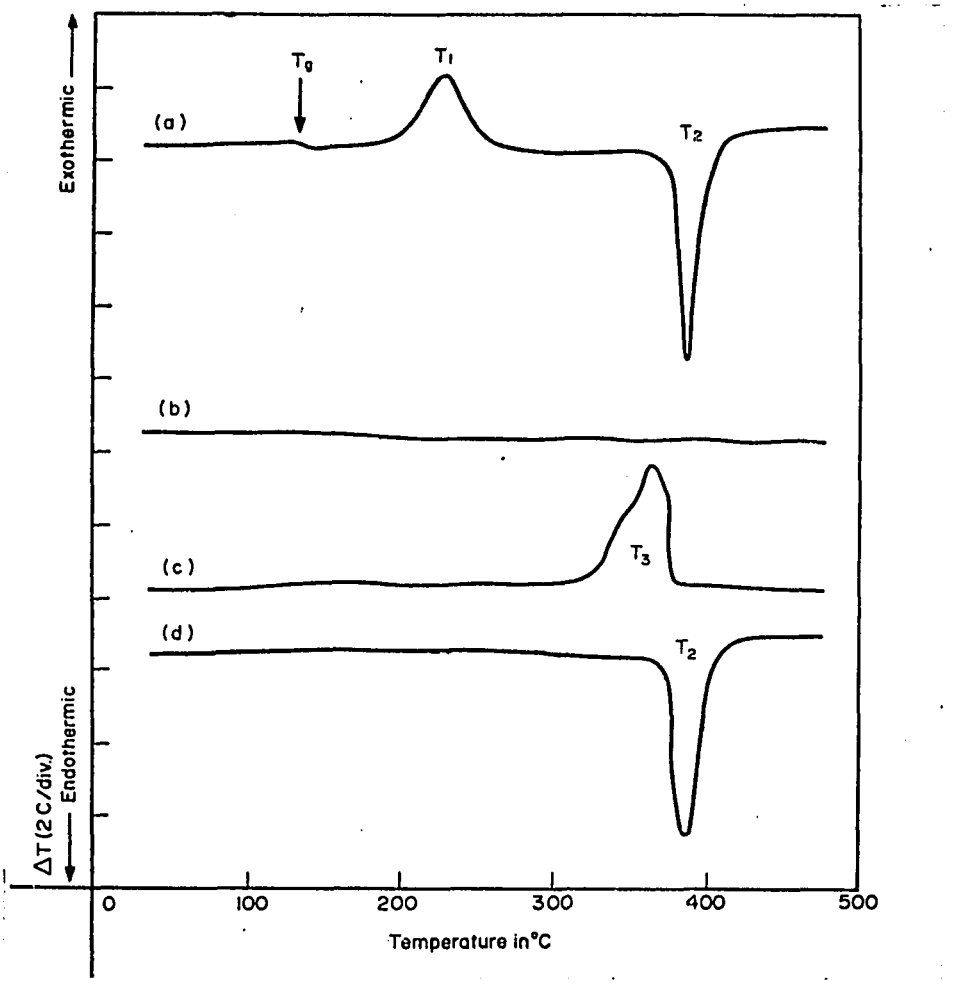

Figure 24. Differential thermal analysis of a memory type chalcogenide alloy $Ge_{16}Se_2Te_{82}$.
(a) Heating from the amorphous state, 25°C/min.;
(b) rapid cooling from the liquid, >50°C/min.;
(c) slow cooling from the liquid, <10°C/min.;
(d) heating from the crystallized state.
(After Fritzche and Ovshinsky, Ref. 43).

electronic mechanism in the threshold switch or, in the event of sufficient overlap, form microcrystalline channels which carry the current in the memory switch. Indeed, threshold devices of thin film $Ge_{10}Si_{12}As_{30}Te_{48}$ kept for successively longer times in the ON-state experience lock-on to the memory state[71], while memory devices of thin-film $Ge_{15}X_4Te_{81}$ operated under extremely short pulsing perform as threshold switches[62].

Studies of both memory and threshold device compositions using scanning electron microscopy and differential thermal analysis should yield information related to the non-crystalline-crystalline transitions that either cause or are caused by switching. Similarly, electron microprobe analysis and elemental X-ray mapping of device composition before and after a switching event should be able to determine the degree to which compositional changes are involved in the transition.

IV. EXPERIMENTAL APPARATUS

A. Bulk Sample Preparation

Bulk glass samples were prepared by mixing the pure elements in powdered form, heating the evacuated container to a temperature above that of the highest melting component and quenching rapidly in air or in an ice bath. A few compositions in a variety of different systems were considered for study. Among those prepared were Si-As-Te, Ge-P-Se, Ge-Se-Te, As_2Te_3, As_2Se_3 and As_2Se_2Te; the last two having been extensively investigated by Kolomiets[2], Edmonds[33], and others. The system chosen, Ge-Se-Te, had until recently *not* been mentioned in the literature except as a potentially useful infrared window[49].

A number of different types and shapes of boats, molds, crucibles and vials were utilized in an effort to obtain a reasonably homogenous sample free of macroscopic cracks, holes, or veins of different composition. The method that finally worked was to use a quartz tube 120 mm. long, made of 100mm. of 3mm. inner diameter tubing connected to 20 mm. of 10mm. inner diameter tubing sealed off at the wide end. The premixed elements were placed into the wide end, evacuated to $\sim 10^{-1}$ torr , and sealed off. The tube was heated to above 950° C (melting point of Ge is 937.4° C) in a Thermolyne furnace, type 10500 for 16 hours, during which time the molten solution was occasionally shaken vigorously.

Immediately before removal from the furnace, the tube was again shaken and inverted so that the contents filled the narrow end. It was then removed and quenched in an ice bath. The purity of the Ge and Te (from other semi-metals, not C, O, and N) was five 9's for each, while that of Se was four 9's, with the prime impurities in the latter two being each other. Drying the reagents or baking out the quartz tube at 1000°C did not affect the results.

The resulting solid solution appears silvery, hard, and brittle in the glassy state, is insoluble in acid, but dissolves in dilute (∿.1M) basic solution forming a suspension rather than a solution. Density measurements, using a pyncnometer showed less than ±.2g/ml (about 4.5%) variation along the length of the sample in some cases. This was taken as one indication of homogeneity; subsequently, electron microprobe analysis served as another. The softening point of the glass, although not measured per se, was confirmed to decrease as a function of the Ge composition as discussed in the previous section. As measurements of conductivity vs. temperature were made, samples with decreasing percentages of Ge were indented by the pressure of the contacts at successively lower temperatures. Near the composition $Ge_{33}Se_{33}Te_{33}$ the softening point is 283 ± 5°C[49]; with 10% Ge, T_g is down to ∿100°C, near 0% Ge it is ∿60°C[50].

Those samples that remained crystalline despite the rapid quenching appeared metallic, pockmarked, formed sharp

cleavage planes and were good conductors. Using Philips' Norelco Instrumentation, the vitreous or non-vitreous state was confirmed by X-ray diffraction analysis of the powdered sample; the lack of any sharp peaks indicated the amorphous state as in Figure 25.

For those compositions that remained in the crystalline state upon quenching, a FORTRAN IV program (see Appendix) calculated the value of d, the distance between planes of atoms, in the Bragg equation,

$$n\lambda = 2d\sin\theta \tag{43}$$

for a series of values of θ, where the first-order (n=1) diffraction peaks occurred for X-rays of wavelength λ. It then compared these values to the ASTM literature values of the elements and various crystalline eutectic mixtures, in order to determine which peaks were due to which materials crystallizing from the melt.

B. Thin-Film Sample Preparation

Thin-film samples were prepared by evaporating bulk samples of the desired compositions onto glass substrates held sufficiently distant from the hot filament to enable the films to quench themselves upon deposition into the amorphous state and not undergo subsequent annealing. A Veeco Hi-Vacuum Evaporation Unit, model VE-400, operating in a

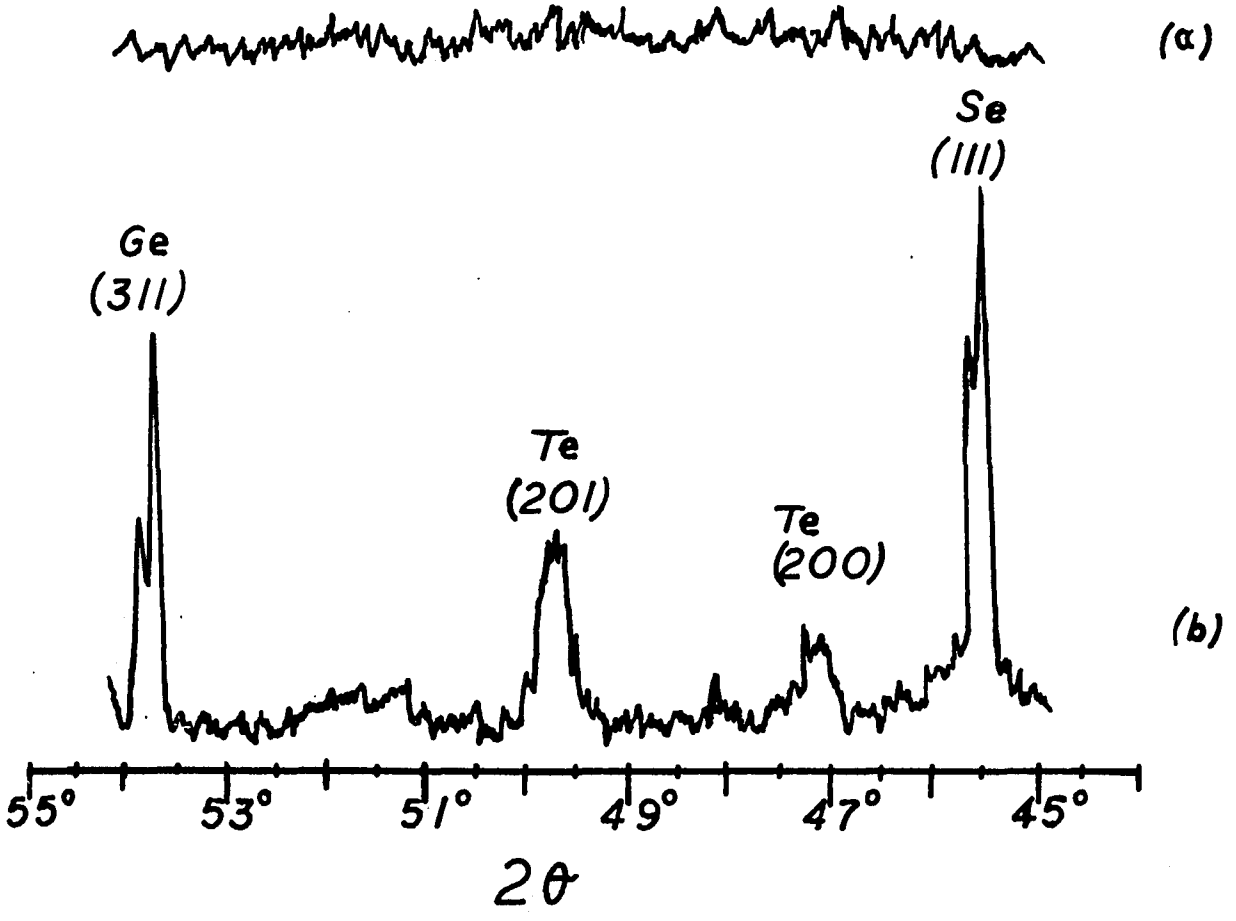

Figure 25. X-ray diffraction peaks for powdered sample of $Ge_{25}Se_{25}Te_{50}$ in (a) non-crystalline state after quench from melt and (b) crystalline state before heating of elemental mixture. (Miller indices in parentheses).

pressure range of 1-2 X 10^{-6} torr during deposition was used. Glass substrates in the form of pre-cleaned microscope slides and optically flat quartz disks were suspended 15-25 cm. above the filament area from an aluminum heat shield where a chromel-alumel thermocouple also attached to the shield monitored the temperature which never exceeded 88°C during an evaporation. For each composition to be studied, a number of films were deposited simultaneously—one each for thickness determination, optical measurements, electrical measurements, and switching experiments.

The actual rate of evaporation was monitored as a function of the film thickness being deposited on the vibrating quartz crystal of a Sloan Deposit Thickness Monitor DTM-4. If the position of the quartz sensor relative to the glass substrates is known, then the thickness of the thin-film samples is some multiple of the film thickness deposited on the quartz crystal which is calculated from,

$$\Delta t = 2\Delta f/\rho \qquad (44)$$

where Δf is the change in the crystal's vibrating frequency, ρ is the film density, and Δt, the thickness in Ångstroms.

The density of the thin film was estimated to be the same as that determined for the bulk sample. This is usually true for crystalline films evaporated from crystalline metals[72] but may be way off for amorphous materials. In any event, the actual film thickness was measured using interferometry

after first depositing a reflecting layer of metal film (either Al or Ag) over the sample film deposited on an optical flat. The displacement of the Fizeau line pattern under monochromatic light and the calculation of the film thickness is illustrated in the schematic of Figure 26. Film thickness measured in this manner differed by less than 10% from the value estimated by the DTM for 50% of the samples.

As with the bulk samples, the thin films were subjected to X-ray diffraction analysis to confirm their noncyrstallinity. A thin film of gold 370Å thick yielded strong peaks for the (111) and (200) planes, indicating that the method was sufficiently sensitive to determine if the thin glass films were indeed amorphous.

The problem of fractional distillation from the bulk mixture can be overcome by flash evaporating only a few grains of powdered sample at a time without allowing molten material to accumulate[55]. A small conveyor belt system built around an old clock motor was installed under the bell jar in order to feed the powdered bulk sample at a uniform slow rate into a quartz chute opening into the hot quartz crucible seated in a tungsten box filament. The rate at which material dropped down the chute could be controlled with a Variac autotransformer. Electron microprobe analysis of the thin-film sample composition with that of the bulk sample from which it was evaporated indicated that this method of

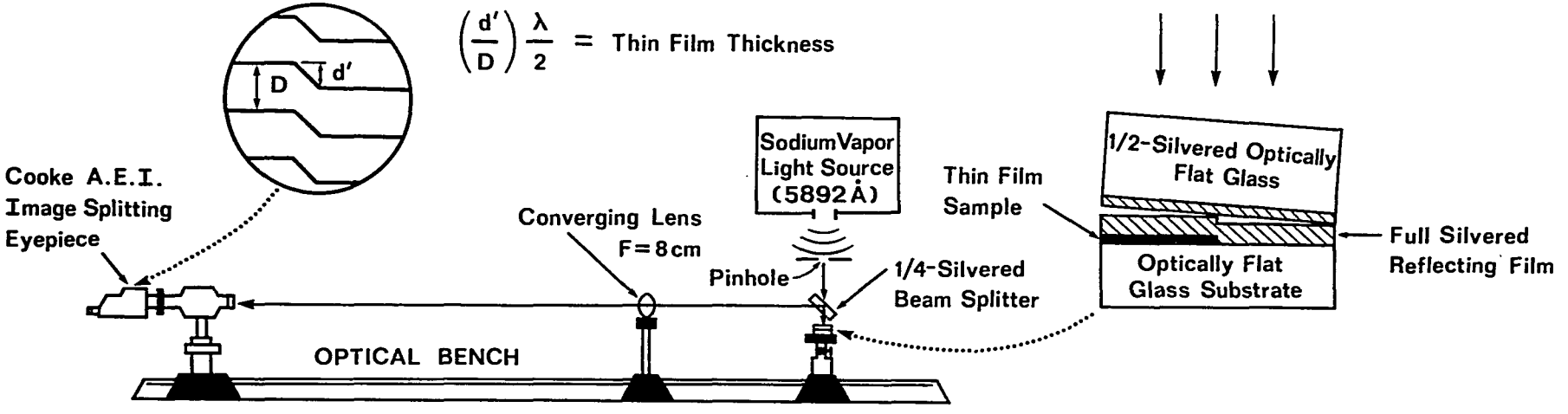

Figure 26. Schematic of apparatus for determining thin-film thickness by measurement of displacement in Fizeau fringe pattern.

preparation yielded the desired film compositions.

Determinations of optical transmission and reflection of the films on the microscope slides were made with a Carey 17 Spectrophotometer for the former and a Carey 14 Spectrophotometer with reflectance attachment for the latter. In both, a microscope slide coated with a thick film of silver served as the standard for 0% transmittance and 100% reflectance.

C. Electron Microprobe Analysis (EMPA)

In order to ascertain the homogeneity as well as the composition of both bulk and thin-film samples, a system of electron microprobe analysis was implemented.

A Coates and Welter Cwikscan/100 Field Emission Scanning Electron Microscope (Figure 27) collimated a narrow beam (250 Å in diameter) of up to 20 keV electrons onto the sample surface, exciting characteristic $K_{\alpha,\beta}$ x-ray lines for $_{32}$Ge and $_{34}$Se, and $L_{\alpha,\beta,\gamma}$ lines for $_{52}$Te. These were picked up by a Princeton Gamma-Tech SiLi detector, amplified, and displayed an a RIDL 400-channel Analyzer, Model 34-12B. The composition by weight at any point relates directly to the ratio of the pulse height of the element in the sample at that point to the pulse height of the pure elemental standard[56]. In addition, x-rays for each of the elements could be channeled through an Ortec 420A SCA to the television monitor giving an x-ray image of that element's distribution near

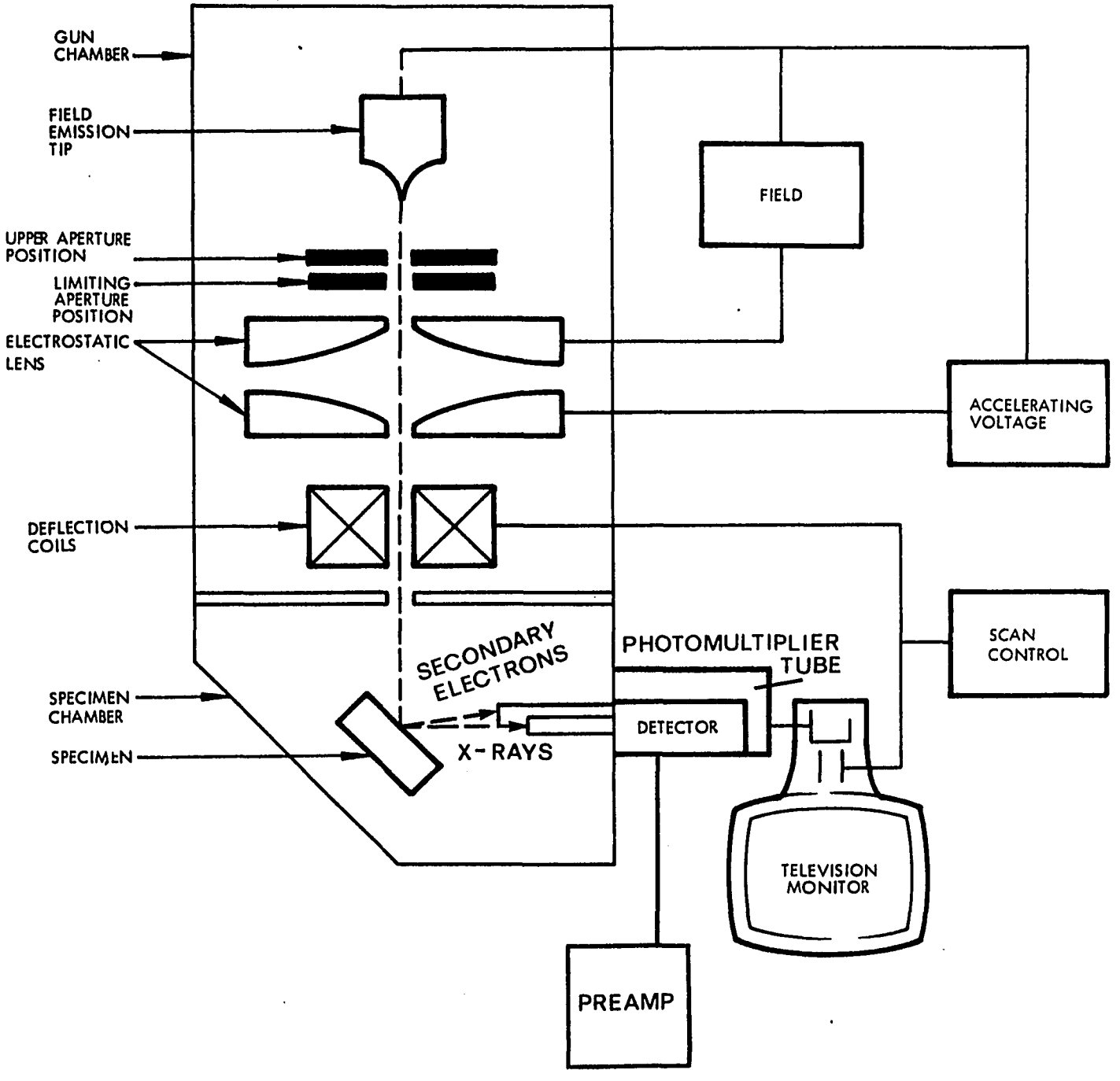

Figure 27. Schematic of Coates and Welter scanning electron microscope, model 100-2, with x-ray analyzing detector in place.

the sample surface. Unlike the instantaneous visual image produced by the secondary electrons in normal use of the SEM, the x-ray image develops slowly over a period of time and, unless collected over a 5-30 minute time exposure, appears only as a haphazard series of flashes on the TV monitor. The background noise over that time period would destroy the image, but is effectively minimized by a Canberra 1464 resistor/rejector. Secondary electron micrographs were recorded on Polaroid Type 52, ASA 400 film, x-ray micrographs on Type 57, ASA 3200 film. A schematic of the instrumentation used in the x-ray analysis appears in Figure 28, while examples of electron and x-ray micrograph appear in Figure 29.

Use of the electron microprobe for quantitative analysis requires careful preparation of the sample surface to eliminate inhomogeneities which might otherwise interfere with x-ray generation and affect the relative peak intensities[57]. The pure Ge, Se, and Te bulk standards were therefore sanded and polished with rouge to a mirror finish. The bulk glass samples were sectioned into flat disks with a stainless steel wire saw using a glycerine-methanol suspension of 1000 mesh corundum abrasive, but were not polished further. Thin-film samples already had a mirror finish on formation.

X-ray intensities for the standards were determined at an accelerating voltage of 20 kV for an electron current that generated x-rays at such rate that the SiLi detector dead-time did not exceed 10%. Live-time counts of 2 minutes were found to be satisfactory for measuring relative intensity

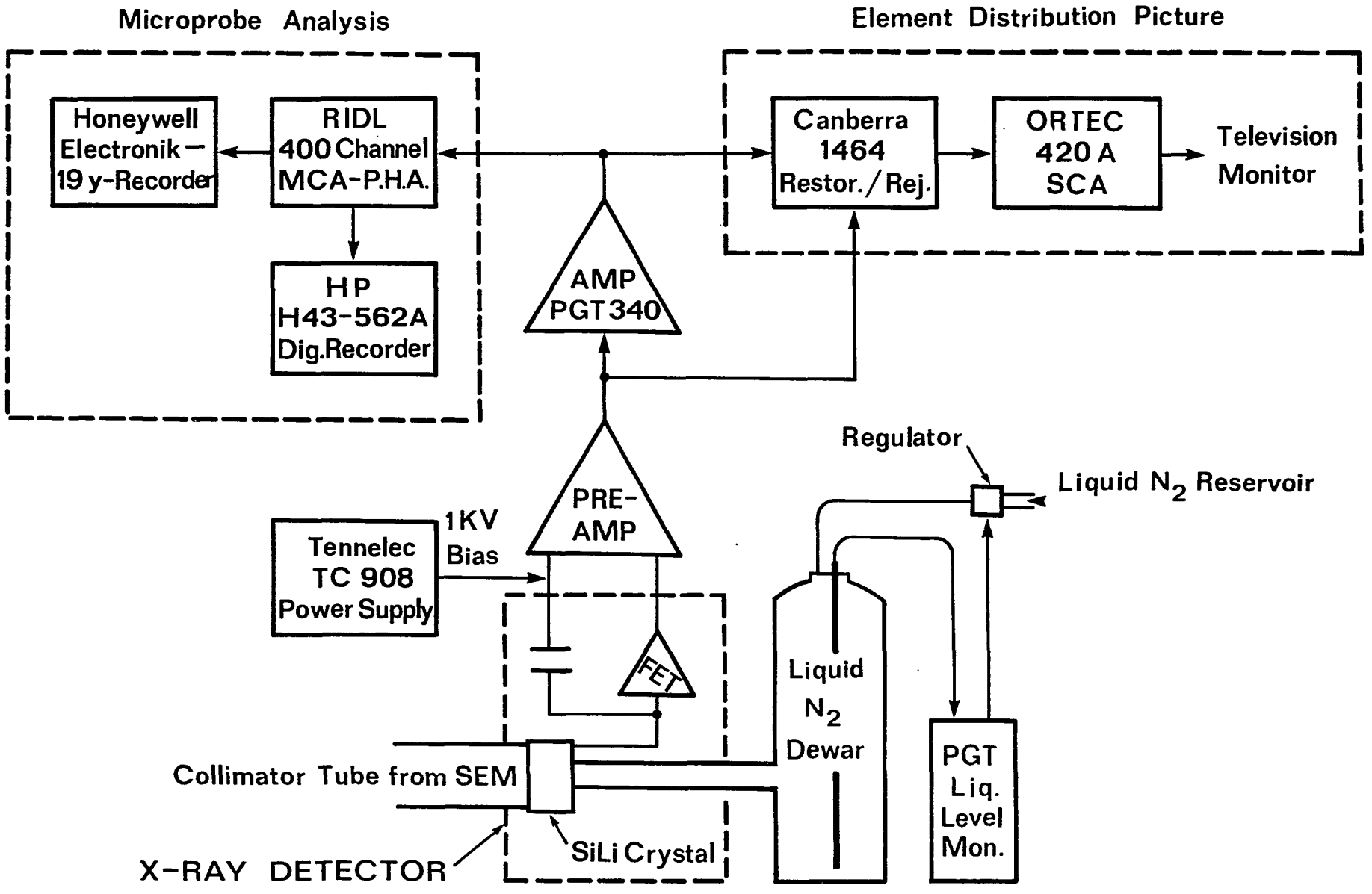

Figure 28. Schematic of the electronic instrumentation for analyzing x-rays generated by the electron beam of the SEM.

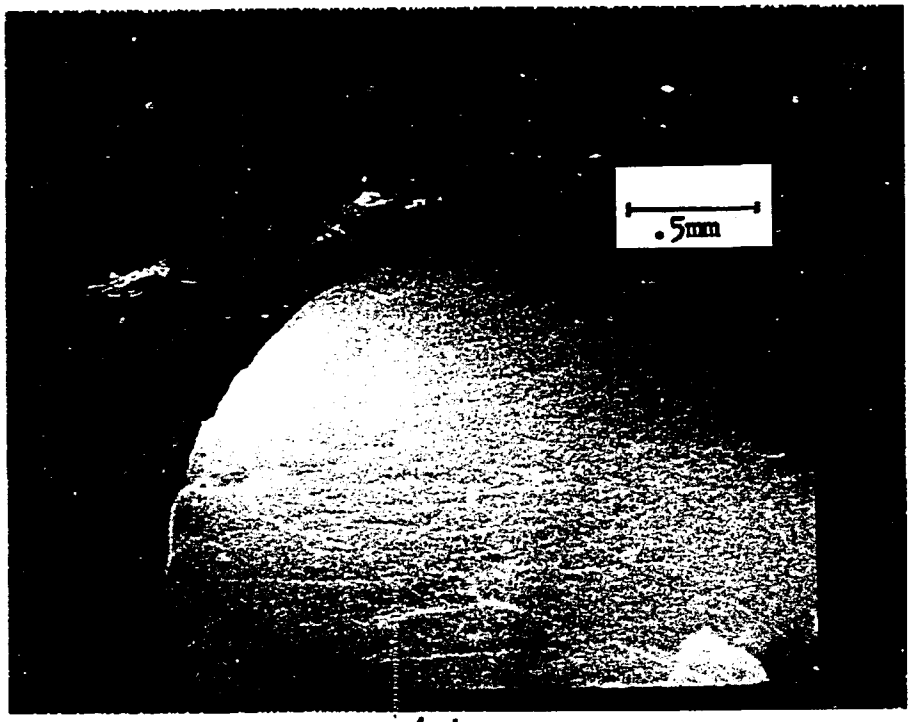

(a)

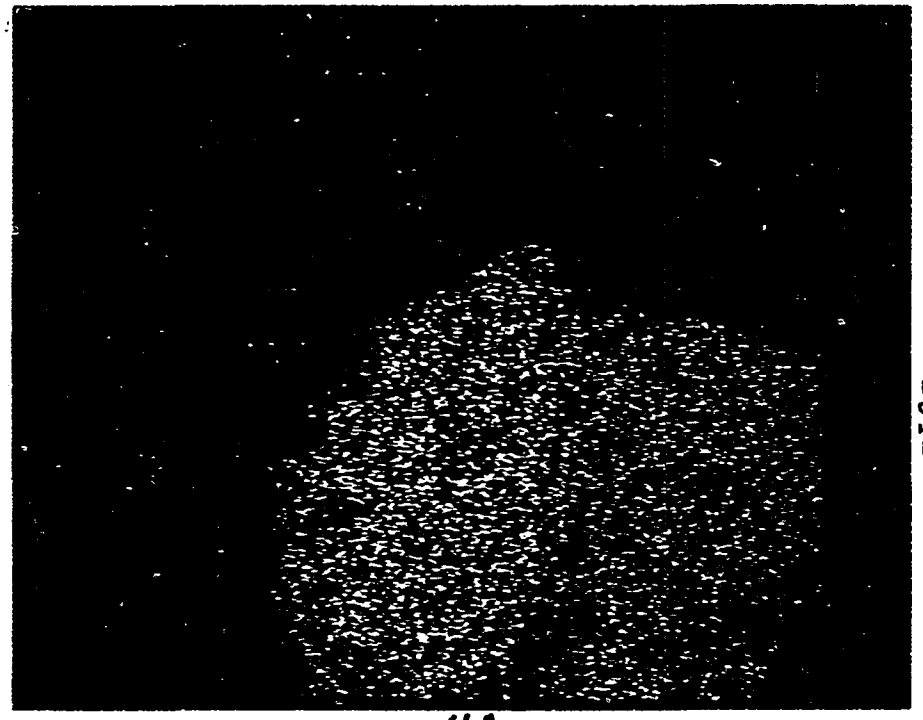

(b)

Figure 29. (a) Electron micrograph of a polished bulk sample of pure crystalline Te quenched from the melt (Magnification 34X). (b) X-ray micrograph of Te distribution.(with restorer/rejector, 10 min. expo.).

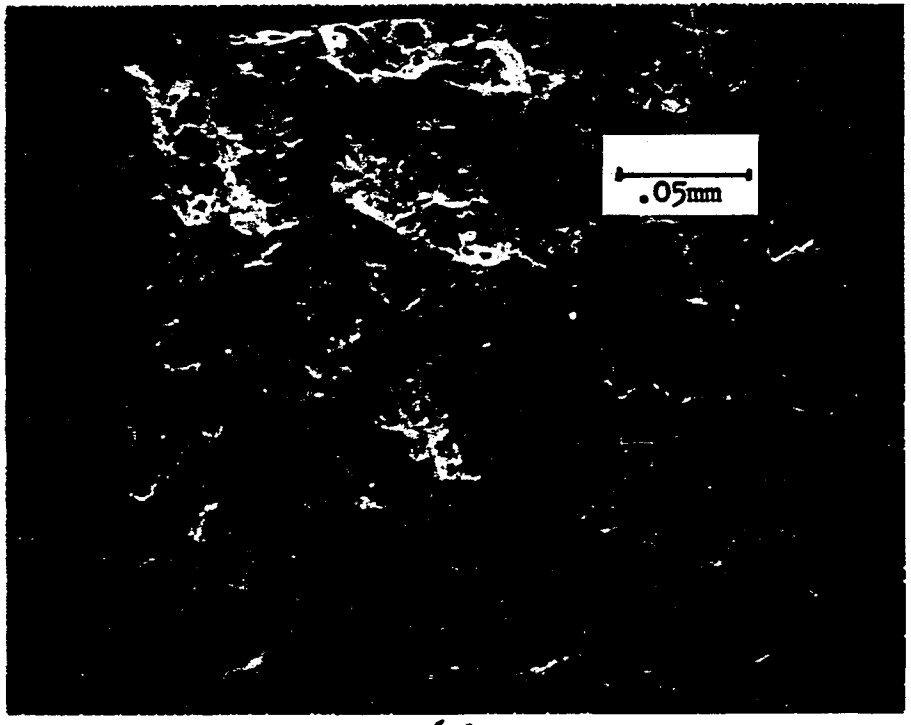

(c)

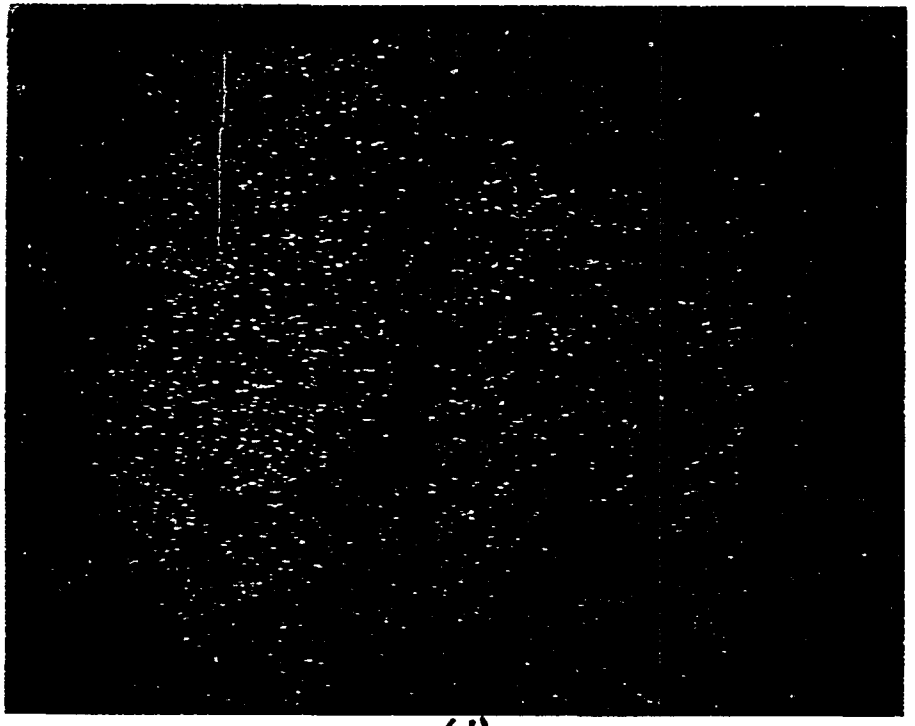

(d)

Figure 29 cont'd. (c) Micrograph of pure crystalline Te (Mag. 340X). (d) X-ray micrograph of Te distribution in (c).

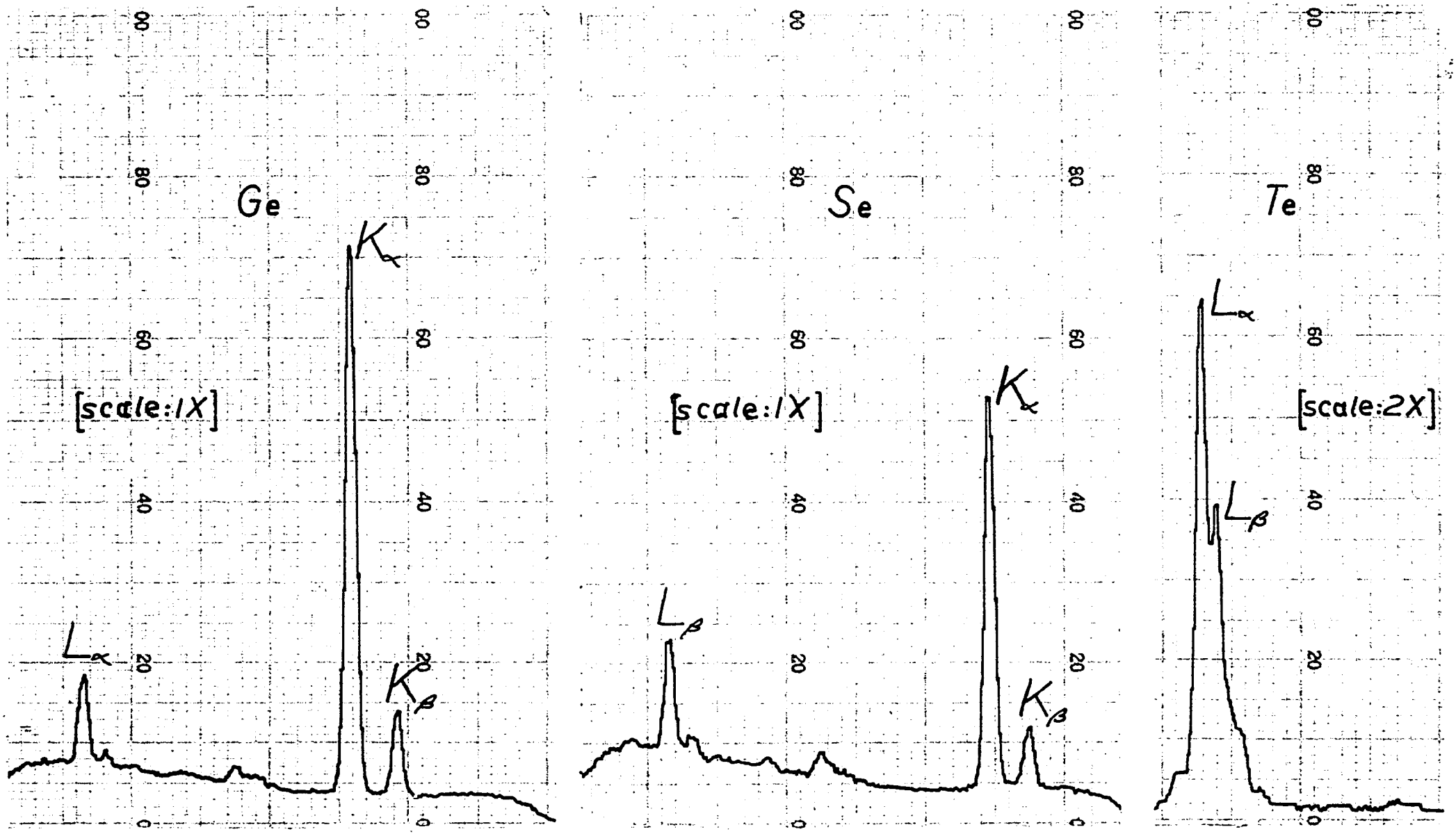

Figure 30. Example of x-ray intensities of pure Ge, Se, and Te standards determined at a magnification of 740X, corresponding to a volume element of ~8 x 10^{-8} cm^3. (2 min. count live time, at count rates of 33, 22, and 62 counts/sec for Ge_{K_α}, Se_{K_α}, and Te_{L_α} respectively; detector dead time ~10%).

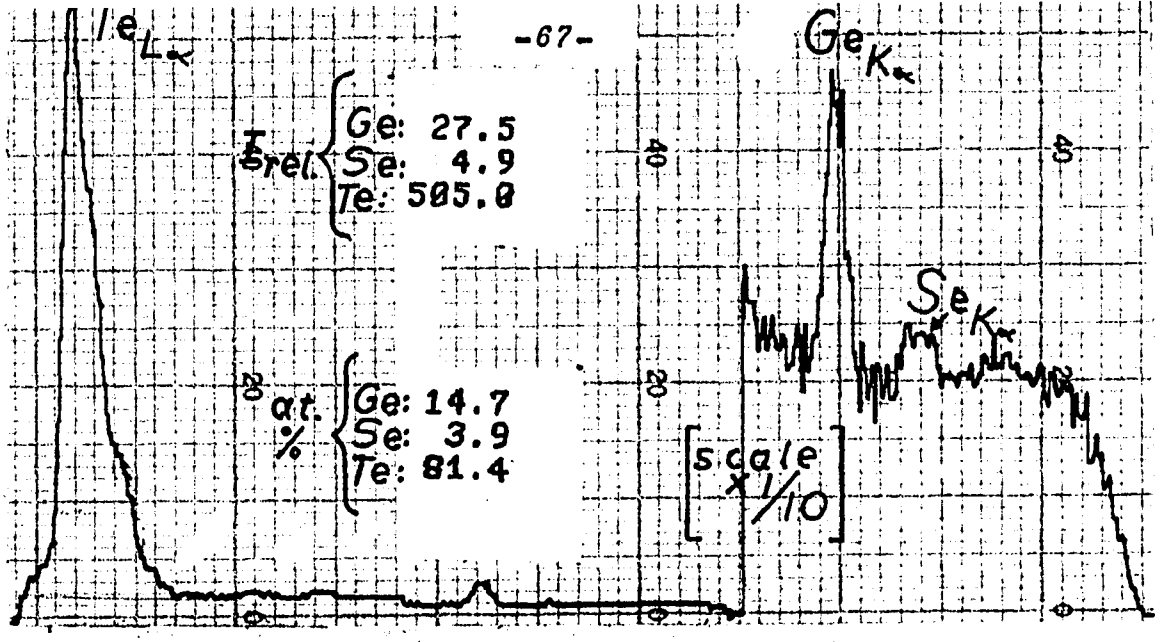

(A)

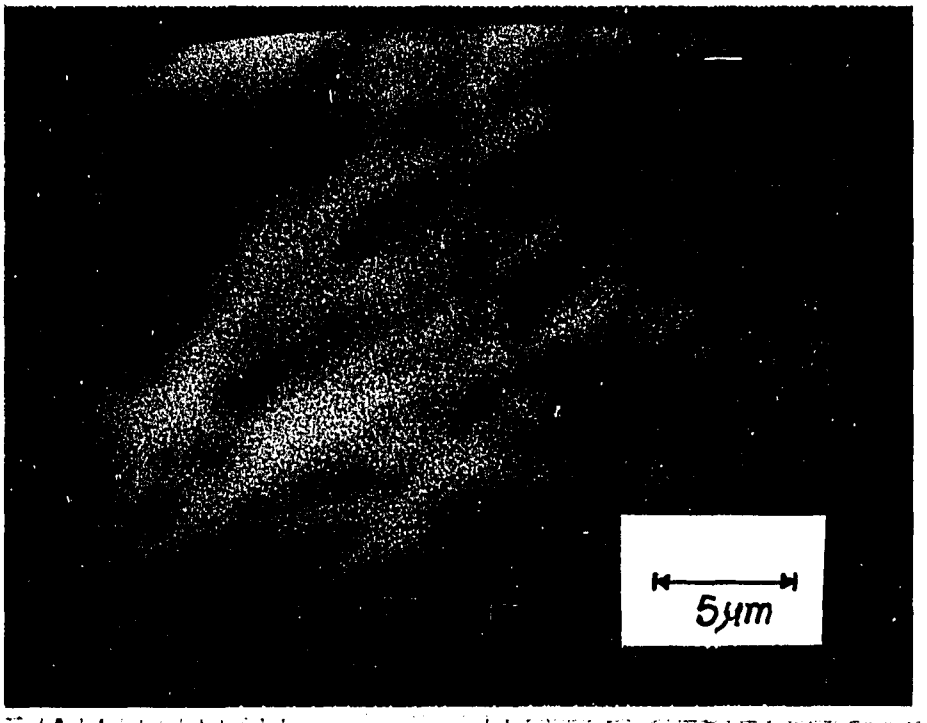

(B)

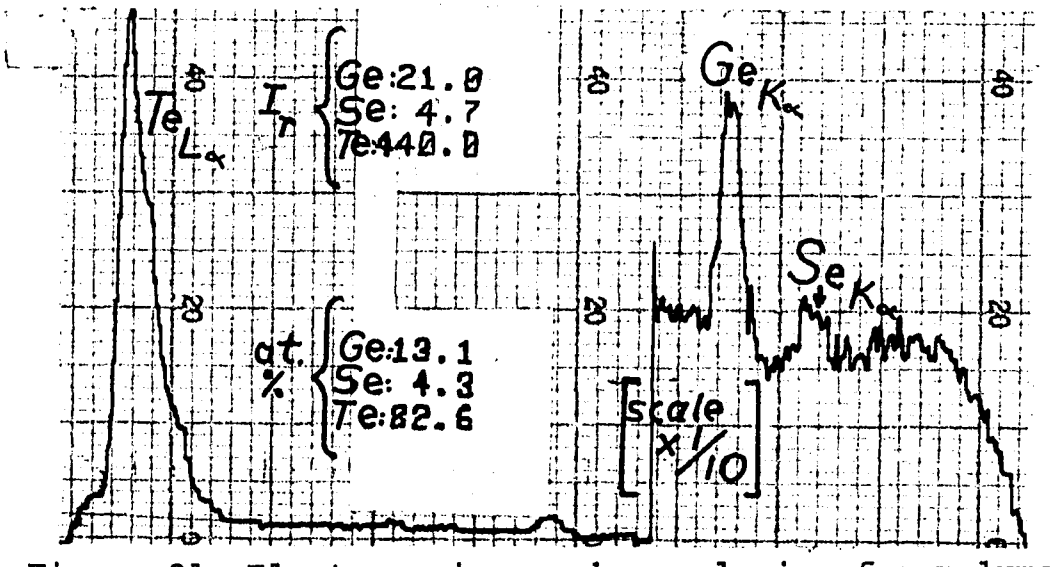

(C)

Figure 31. Electron microprobe analysis of a volume ($\approx 4 \times 10^{-9} cm^3$) of $Ge_{15}Se_4Te_{81}$ bulk sample (a) before and (c) after a switching pulse. (b) Electron micrograph of the area before switching (Mag. 3500X). (2 min. count live time; 10% D.T.; 2, 1, and 54 counts/sec. for Ge, Se, and Te respectively).

peaks, and correction was made for background. A minicomputer program (see Appendix) calculated the relative atomic percent composition from the relative x-ray peak intensities of the $Ge_{K\alpha}$, $Se_{K\alpha}$ and $Te_{L\alpha}$, correcting the $Se_{K\alpha}$ peak at 11.2 keV for the slight overlap from the $Ge_{K\beta}$ peak at 11.0 keV. No corrections were made for matrix effect or x-ray intensity variation with atomic number, both negligible compared with surface inhomogeneity effects.

Figure 30 illustrates the x-ray intensities typical of the standards, while Figure 31 gives EMPA results for an amount of material corresponding roughly to 0.02 micrograms.

D. Electrical Measurements

After formation, the bulk samples, still enclosed by the quartz tubing, were sectioned into cylindrical lengths of 0.5 - 1.0 cm. and 0.05 - 0.1 cm. with diameters of 0.3 cm. Contacts to the sample included evaporated leads of first copper, then aluminum, silver paint and silver cement. The best results, however, were obtained with evaporated gold leads against which copper metal electrodes formed a pressure contact in the sample holder assembly shown in Figure 32. The edges of the electrodes were rounded so as to minimize the voltage drop at the area of contact which was effectively 1.0 mm^2. The conductivity did not change as pressure was increased substantially or decreased slightly on the ends of the sample holder, indicating a fairly good contact.

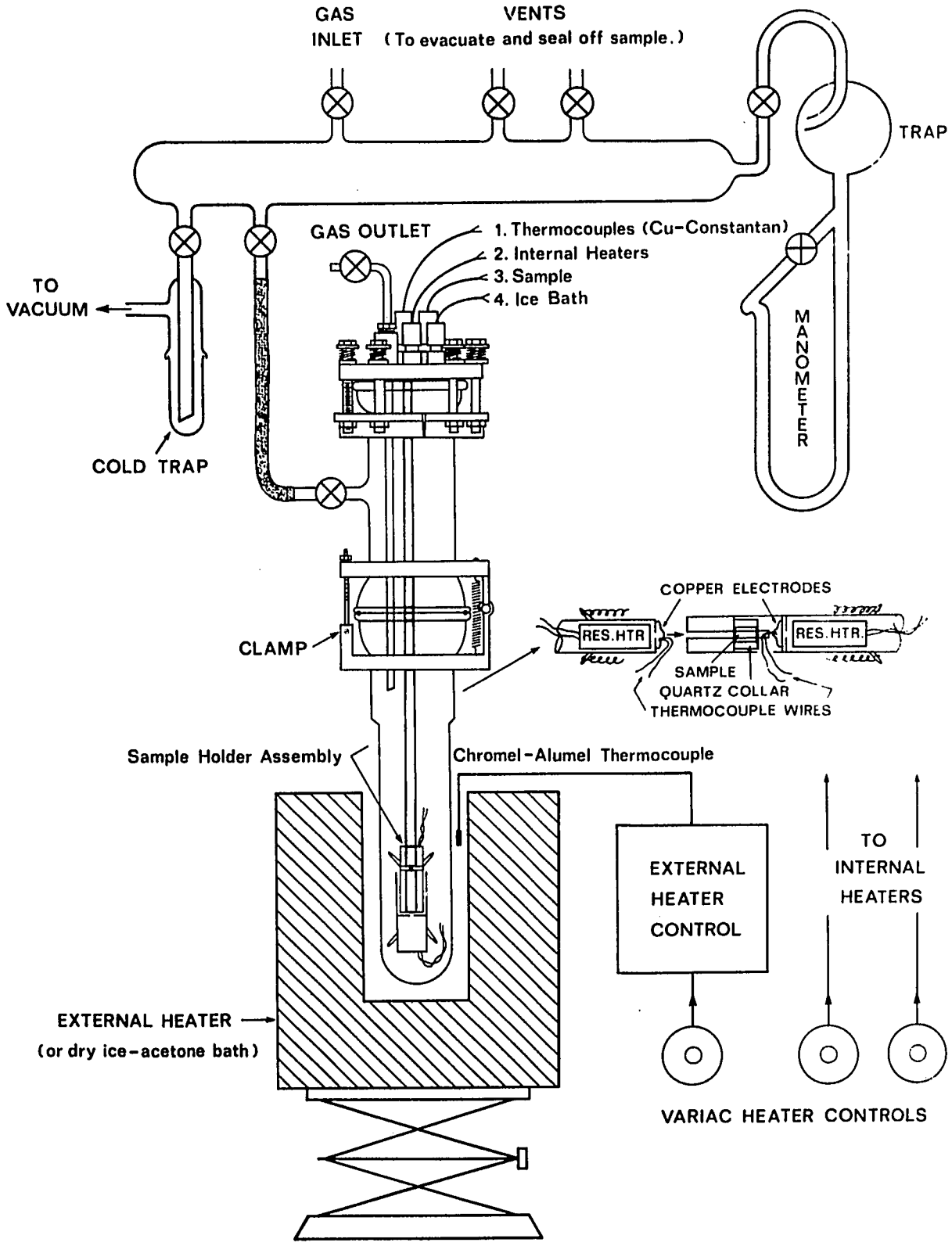

Figure 32. Schematic of experimental apparatus for conductivity and thermoelectric power measurements as a function of temperature and/or pressure.

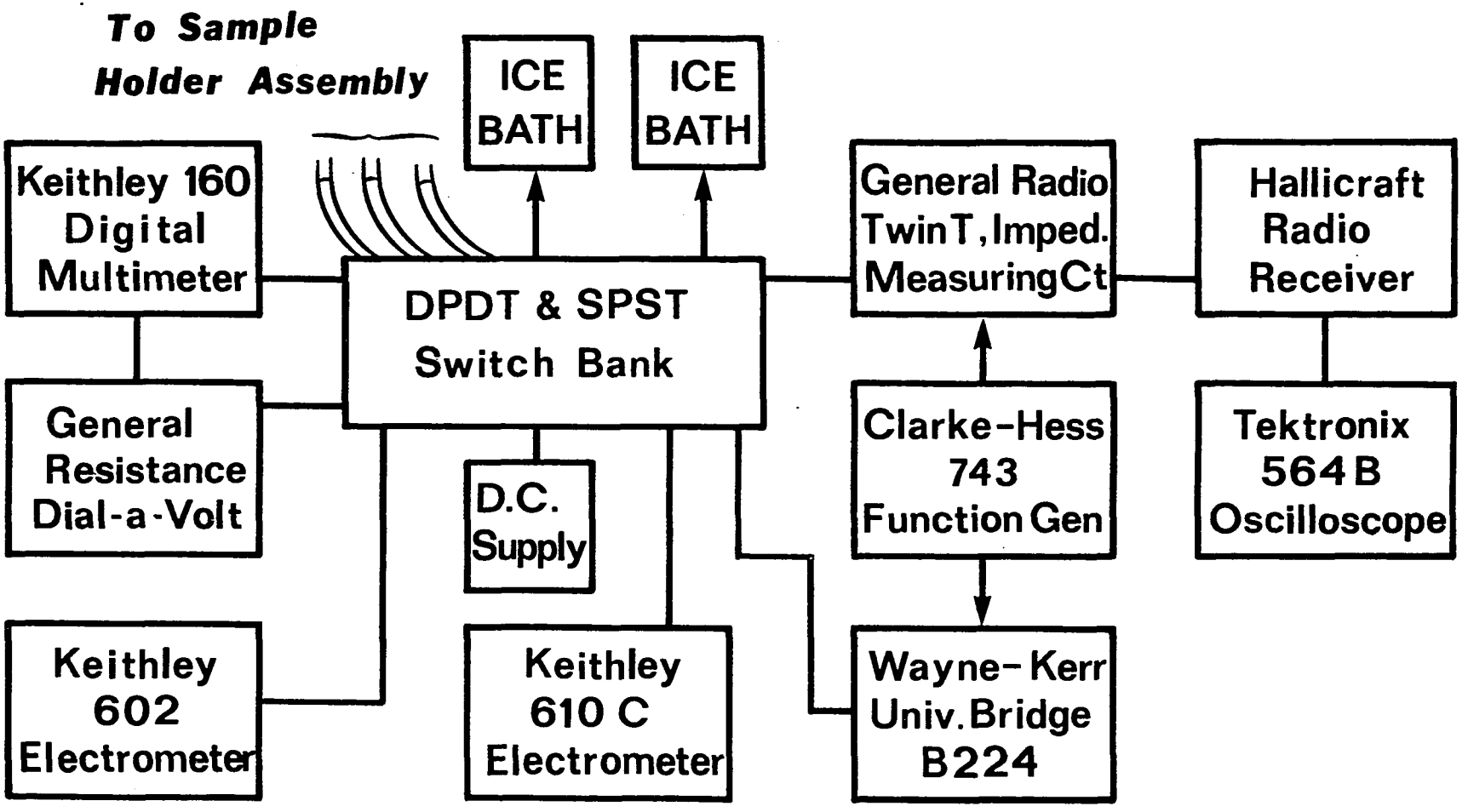

Figure 33. Schematic of instrumentation for d.c. and a.c. conductivity and thermoelectric power measurements.

The copper electrodes enclosed copper-constantan thermocouple wires which served to measure temperature in conductivity vs. temperature measurements as well as temperature gradients in thermoelectric power measurements. The copper wires of the thermocouples also served as the leads to the sample. Two small resistance heaters fit into either end of the assembly to maintain constant temperature or a temperature gradient. The entire unit fit into a large glass jar leading to a mechanically pumped vacuum system, allowing introduction of different gas environments. The jar, in turn, fit into a coil heated furnace which kept the whole apparatus at constant temperature. This setup enabled the determination of d.c. conductivity, a.c. conductivity over a range of frequency, and thermoelectric power successively, all over a range of temperature, and all for the same sample. The system is diagrammed in Figure 32, with the instrumentation given in Figure 33.

Contacts to thin films are usually metals evaporated onto the film surface from either side, as in a *sandwich* geometry, or on the same side separated by a space, as in a *gap* geometry. Copper and silver leads are unsatisfactory since they cause crystallization and alloying in amorphous films[58]. Refractory metals, like molybdenum and tungsten make excellent leads, but require sputtering equipment. Gold, considered a satisfactory if expensive substitute[52,73], was used instead. The metal was evaporated onto glass slides, despite its poor adhesion to glass, then scratched with a very fine hypodermic needle in order to create a narrow gap spacing (≈150μm), and

finally coated with the amorphous glass film. This procedure eliminated the need to expose the formed film to an evaporation of gold (melting point 1063°C) at high filament temperatures; the few non-crystalline film compositions that were exposed in order to create sandwich electrode geometries were all found to have become crystalline.

The gap devices were then coated with a quick-hardening plastic mixture which, when removed from the glass substrate, lifted the evaporated films. The resulting gap device, a plastic disk covered by a thin-film sample (0.2-1.0μm.) of amorphous material covered, in turn, by a thick film (>2μm.) of gold,then had indium wire cold soldered against the surface gold electrodes to form the electrical contacts used in conductivity measurements and switching.

Contact problems such as carrier injection, and rectification which normally occur as a result of Schottky barriers arising due to the different work functions at the metal-insulator junctions are absent in metal-chalcogenide glass junctions. The high density of localized states in the glass accommodates the space charge within 30 Å of the electrodes, thin enough to allow carriers to tunnel through and give an ohmic contact (as in metal-metal junctions)[19]. Indeed, gold-glass contacts have been found to be ohmic[81].

The problem of surface conduction dominating the conductivity as encountered in organic semiconductors is

negligible in these chalcogenides. In the cases of organic molecular crystals, where absorbtion and adsorption of gases at various stages of the experiment may result in charge transfer between the gas and the surface states of the sample creating additional carriers or reaction with the surface to create a more conductive compound, the surface conductivity rather than the bulk conductivity is inadvertently measured[9,51]. The conductivity of these glasses, however, is not affected by either changes in gas pressure in oxygen and in air, or by different environments, oxygen, air, helium, or vacuum. Similarly, the room temperature conductivities of $Ge_{25}Se_{45}Te_{30}$ and $Ge_{33}Se_{33}Te_{33}$ remain unchanged upon introduction of a grounded guard ring.

1. D.C. Conductivity

Early measurements using an electrometer to read sample resistance directly were misleading, as high resistance readings often changed values for different range and multiplier switch settings, the combined effects sometimes exceeding a thirty fold difference between readings at the same temperature. The problem may have been due to the silver cement type contacts. Subsequent satisfactory determinations were made using the copper electrode pressure contacts pressed against the evaporated gold leads on the sample ends. A constant voltage was supplied in alternate directions across the sample by a Power Designs D.C. Source, Model 5005S, and the current in the circuit read from a Keithley 610C electrometer. Standard resistors of up to 1×10^{11} ohms were used

to confirm the circuit operation. The temperature was monitored with copper-constantan thermocouples referenced in an ice bath, with the developing voltage read from a Keithley 160 Digital Multimeter and, at higher temperatures, bucked by a General Resistance Dial-A-Volt voltage to reduce the thermocouple voltage sufficiently to enable it to be read with greater accuracy off the millivolt scale of the multimeter. The system was filled with helium at slightly greater than atmospheric pressure to allow better heat conduction than afforded by a vacuum.

2. A.C. Conductivity

After a d.c. measurement was made, the sample leads were switched so as to connect a Wayne-Kerr Universal Bridge B224 to the sample. Balancing the a.c. bridge to a null point yielded the conductance and capacitance of the system, the conductance being effectively that of the sample, while the capacitance varied with the lead geometry. The internal source of the bridge provided a frequency of 1592 Hz ($\omega=10^4$). For values of 0.5— 50 kHz a Clarke-Hess Model 743 Function Generator was used as an external source, with the input voltage to the bridge monitored on a Tektronix type 564B Oscilloscope to keep the null detector at maximum sensitivity (which, at high sample resistance, at the limit of the bridge's resolution, was not possible at <1 kHz or >20 kHz).

In an effort to obtain conductivity values at higher frequencies, an attempt was made to treat the sample as a resistor, R, and capacitor, C, in series with a variable

inductor, L, used to achieve a resonance R-L-C circuit. At the resonance frequency, f, the Q factor is directly related to the sample resistance by[53],

$$Q = f/\Delta f = \frac{1}{R}\sqrt{L/C} \tag{45}$$

where Δf is the rms value of the frequency bandwidth. In practice, however, L has to be very large to overcome the large value of the sample R and still yield a sharp Q factor. As a result, the resonance frequency has to drop, since

$$f = \frac{1}{2\pi\sqrt{LC}} \tag{46}$$

and a high frequency cannot be attained. Another attempt, using a resonating cavity at microwave frequencies was impractically complicated.

As a compromise, an old Genaral Radio Twin T Impedence-Measuring Circuit was used with the Clarke-Hess function generator as a source, an old Hallicraft radio receiver as a detector, with the ocsilloscope serving as a null detector. The shortcoming of this setup is the limited conductance range of the Twin T circuit, 1-100 μmhos (10^4-10^6 ohms) as well as the sharp dependence of the circuit balance on the lead geometry (but not the length of the leads). Using the apparatus and lead geometries used previously, the a.c. resistance for a series of standard compositional resistors

ranging from 10^4-10^6 ohms at 0.6, 1.0, 1.5, and 2.0 MHz (the limit of the function generator) yielded a variety of values which served as a yardstick for sample resistance in the neighborhood of those values. That is, for a sample whose d.c. resistance compared with the d.c. resistance of a standard resistor, an a.c. value that compared with the a.c. value of the standard resistor was taken as an indication that the sample's d.c. and a.c. resistances were the same at that frequency and temperature. Although admittedly somewhat arbitrary and not altogether satisfying, this method does seem to confirm the conduction mechanism suggested by the results of the a.c. conductivity measurements in the lower audiofrequency range.

3. Thermoelectric Power

The sample leads were switched once more to allow measurement of the thermoelectric power, the voltage developed across the sample over a temperature gradient established between the sample ends. The sign of the TEP voltage, as noted earlier, is important, and follows the convention of Figure 34.

A reversible temperature gradient is set up with the aid of the two small heaters as noted earlier (Fig. 32). Constant ΔT, was established by use of a Honeywell Electronic 19 Recording Potentiometer which produced a pair of parallel voltage traces corresponding to the two temperatures at the ends of the sample.

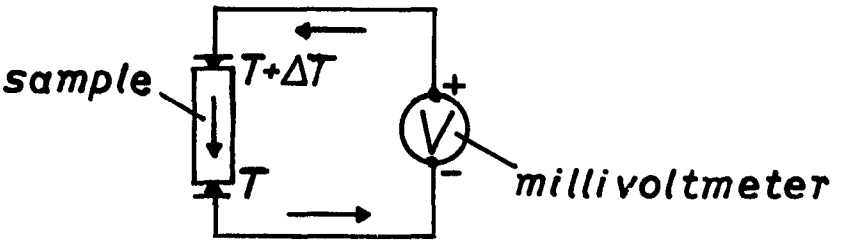

Figure 34. TEP sign convention. Current flowing from hotter end at T + ΔT to cooler one at T yields a positive voltage[54].

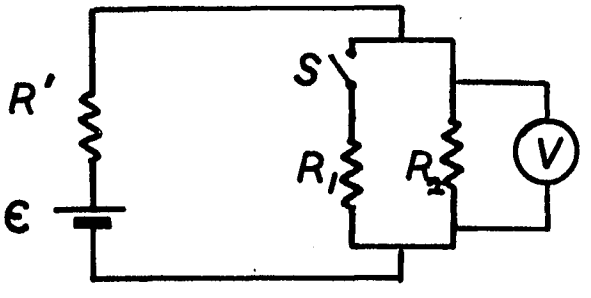

ϵ = TEP Voltage

R' = sample resistance

R_1 = 3.3 x 10^6 ohms

R_2 = 1.0 x 10^6 ohms

Figure 35. Equivalent TEP circuit diagram as described in text.

Early determinations of the TEP were positive, confirming the hole conduction predominance seen in all other chalcogenides. However, the value of the Seebeck coefficient increased exponentially as a function of temperature, instead of decreasing linearly as $1/T$, as predicted by equation (39). Apparently, sample resistance was greater than the input impedence of the Keithley 155 Null Detector Voltmeter (1 MΩ) and, with increasing temperature, was decreasing relative to it, hence the exponential dependence.

Again resorting to elementary theory, the sample was treated as a source of emf with internal resistance, R′. Referring to Figure 35, R_2 was the input impedence of the voltmeter and R_1 a resistor of comparable magnitude. The voltage across the voltmeter was measured at a number of temperature gradients at different average temperatures with the switch open, then with the switch closed. The equations for the value in each case were then solved simultaneously to determine values of ε, the TEP voltage, and R′ the sample resistance at that temperature. In practice, however, the numbers did not work out. The resistance R′ even turned out negative once, as did the value of ε. Besides, even a small error in reading the voltmeter resulted in a tremendous per cent error in the calculated values of R′ as compared to the d.c. conductivity determined values.

The situation was partially resolved by the use of the Keithley 602 Electrometer (input impedence $>10^{13}$) to read the

TEP voltages. The Seebeck coefficient remained positive at all temperatures, regardless of the direction of the temperature gradients which were alternated every few determinations. The actual value of the TEP for the sample at each temperature gradient was calculated by subtracting the TEP of the copper leads corresponding to that temperature gradient. The absolute value for S_{Cu} was determined from the empirical relation

$$S_{Cu} = 5.45 \times 10^{-3} T + 0.2 \qquad (47)$$

which holds in the temperature range 200-450°K[74].

E. Switching

In order to determine the switching characteristics (Fig. 22) of an amorphous sample, a circuit (Fig. 36) was designed to monitor the current passing through it as a function of voltage across the sample. Both current monitored on a Keithley 160 Multimeter, and voltage, monitored on a Keithley 602 Electrometer, were displayed on an HP-7035 x-y recorder to give the current vs. voltage trace.

Contacts to the thin-film gap devices were described earlier. Contacts to the bulk samples were fabricated in the following manner. Thin tungsten rods were etched in a 1:1 solution of nitric and hydrofluoric acids until a very fine tip had formed. The tips were bent nearly to a right angle and the thicker ends wedged into small copper tubes to

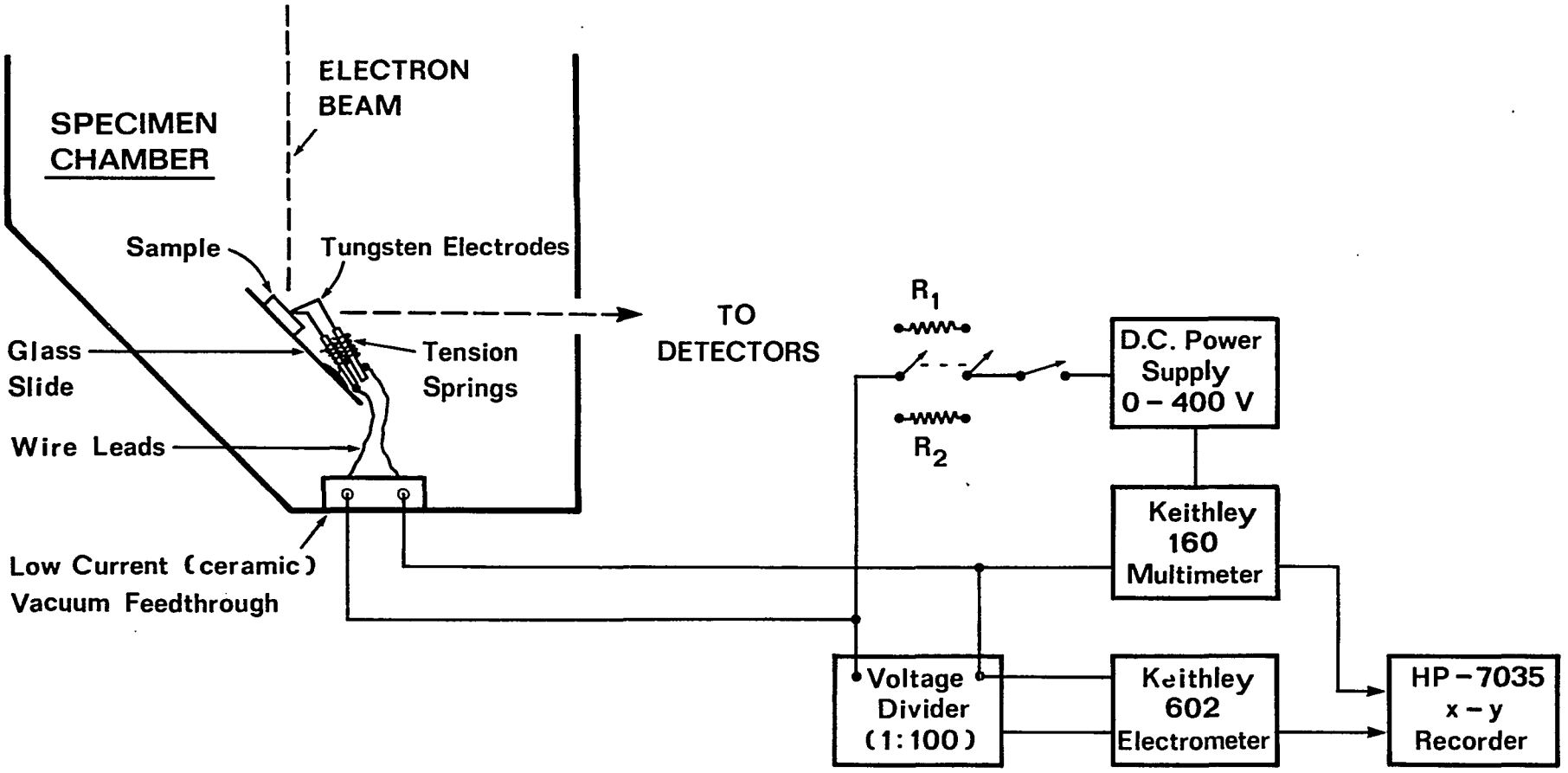

Figure 36. Schematic of circuit used in measuring switching characteristics of bulk samples in SEM. Ratio of R_1 : R_2 was either 100 or 10, with values for R_1 of 100k, 10k, or 1k ohms.

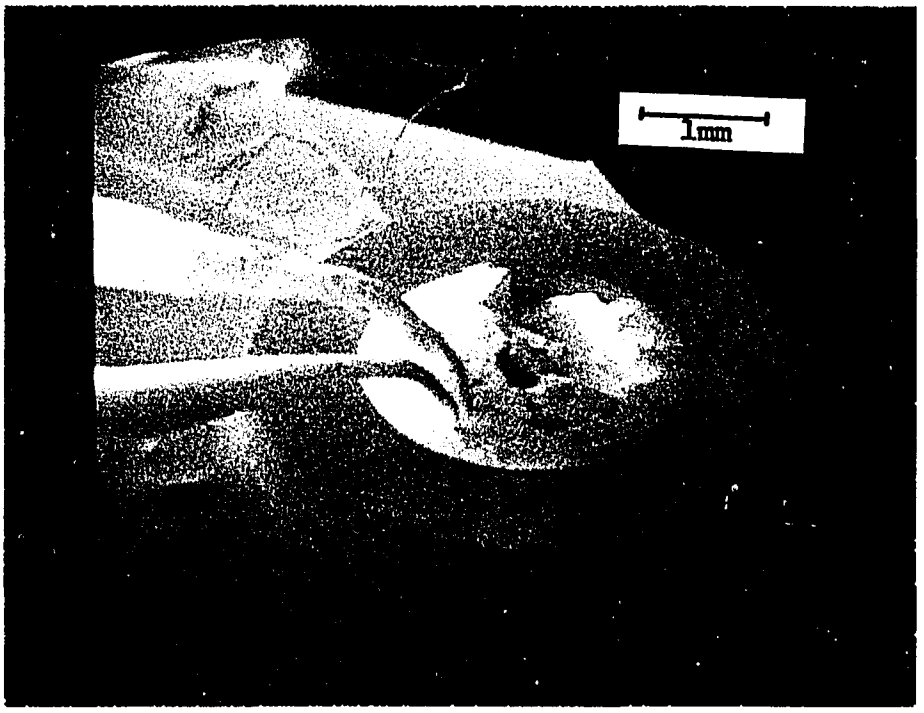

Figure 37. Sectioned bulk sample surrounded by a quartz collar with tungsten point electrodes in place as it appears in the scanning electron microscope before switching (Mag. 15X).

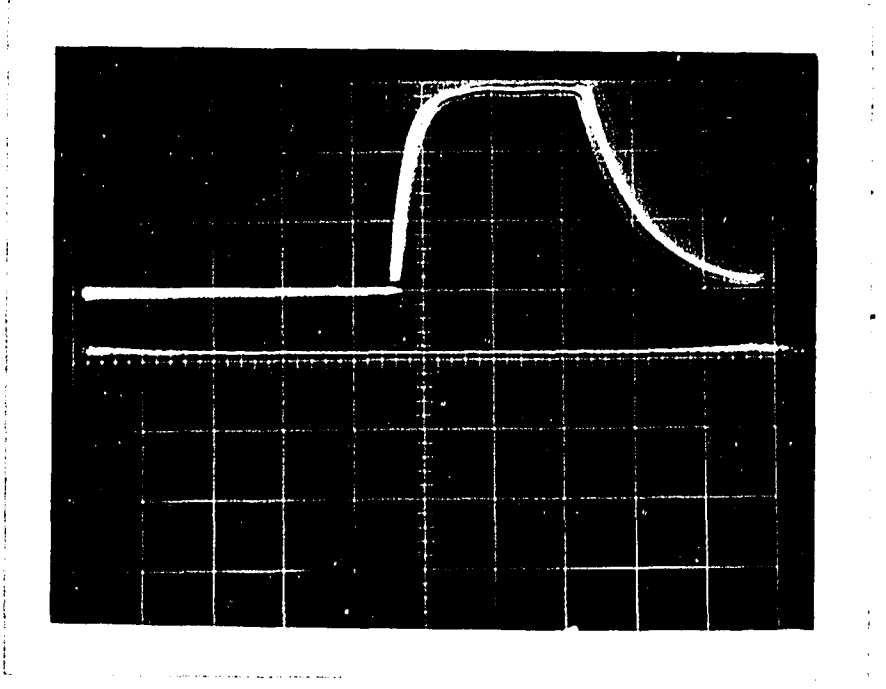

Figure 38. Oscilloscope trace of 300V d.c. pulse (reduced here 1/10 by the voltage divider) used to switch sample out of low resistance state. Horizontal: 20 msec/div. Vertical: 10V/div.

which copper wire leads were soldered. The tubes were mounted on a glass slide with heat sensitive cement (to enable repeated repositioning) and positioned so that the tungsten tips rested on the sample mounted on a double-sided adhesive at the other end of the slide. To be certain of good and continuous contact, the copper tubes were enclosed in tiny coiled springs which were embedded in the cement in such a way as to force the closely spaced (<0.2 mm.) electrodes against the sample surface.

An aluminum flange containing a ceramic current vacuum feed-through was machined to fit the SEM and allow the experiment to be performed in the microscope. Figure 37, an electron micrograph, shows a sample in place.

In a switching experiment,the voltage across the sample with a current-limiting resistor (10kΩ or 100kΩ) in series was increased until, at a high enough field, the current response became non-ohmic. If, after removal of the field, the sample remained in a conducting state, a smaller resistor (0.1-0.01X) was substituted for the load resistor and a higher current pulse (Fig. 38) was passed through the sample. Electron microprobe analysis data and element distribution x-ray micrographs were taken at various points in an effort to monitor compositional and/or structural changes.

F. Differential Thermal Analysis

Because memory switching entails a phase change from

the non-crystalline to the crystalline state, and threshold switching, at least in bulk samples, is to some degree also due to that transition, a DTA study of Ge-Se-Te glasses as a function of their compositions was undertaken.

A duPont 9 9 0 Thermoanalyzer (Fig. 39) calibrated against the various phase transitions of rhombic sulfur in the range 111-445°C was used. The glass samples were run in the range 50-490°C under a flowing nitrogen atmosphere at a heating rate of 20°C/min. against a reference sample of glass beads. The thermocouples were of chromel-alumel, and sample size was approximately 40 mg powdered to 120-325 mesh.

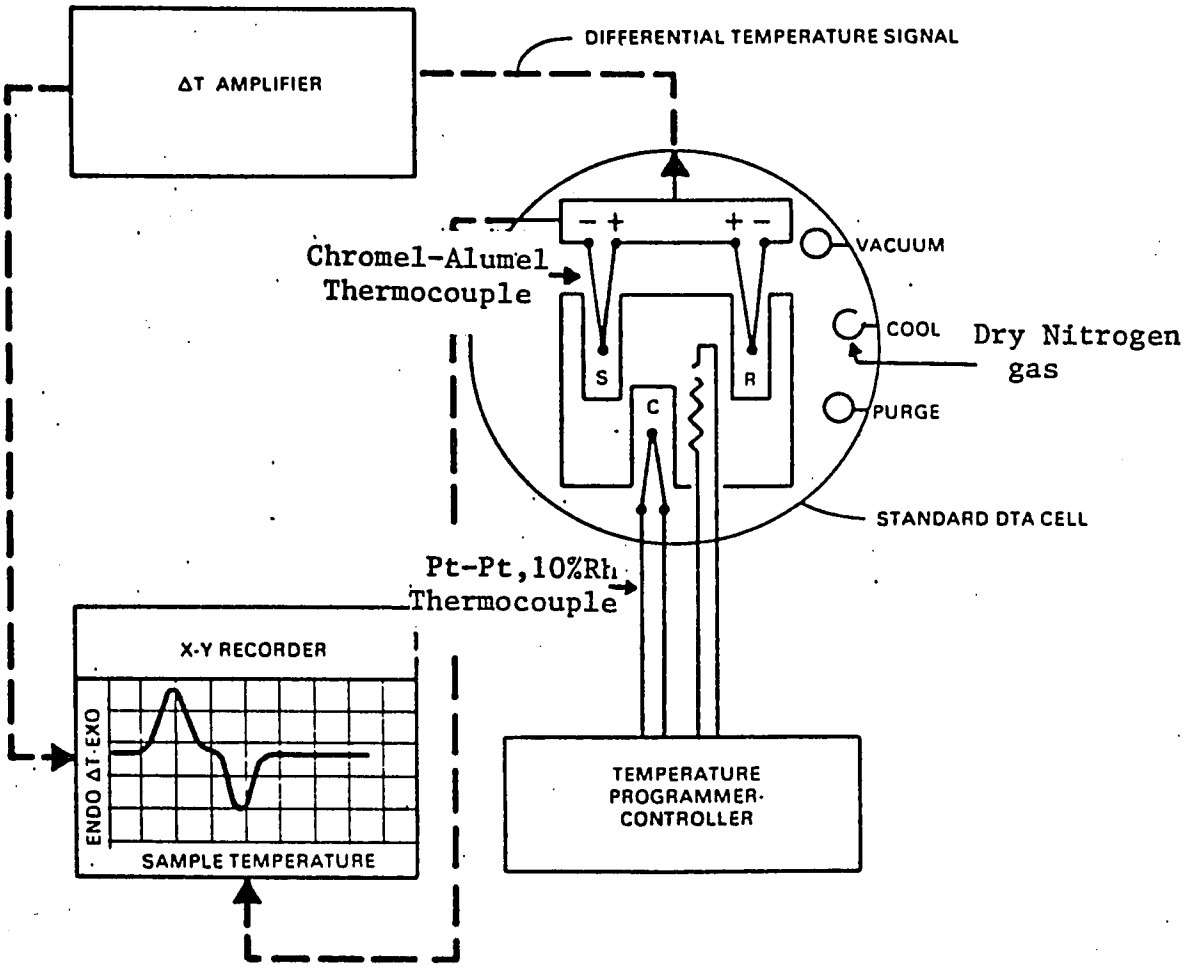

Figure 39. Schematic of the DuPont 990 Thermoanalyzer System with standard DTA cell.

V. EXPERIMENTAL RESULTS

A. Glass-Forming Region

Ge-Se-Te compositions that cooled to an amorphous state upon quenching from the melt appear in the phase diagram of Figure 40. The propensity toward formation of the non-crystalline state seems to increase with Se content and decrease with Te content.

Analysis of the peaks obtained upon x-ray diffraction of the crystalline compositions are illustrated in Figure 41. It is interesting to note that for compositions above the glass-forming region, crystallinity was due to the formation of $Ge_{30.8}Te_{49.2}$ eutectic, while below the glass forming region it was due to crystallized Te only. Within the glass-forming region, compositions that were allowed to cool slowly (by leaving to cool in the oven) exhibited cyrstalline peaks due to both Te and GeTe. Later DTA results confirmed that certain glass compositions undergo two successive crystallizations upon heating beyond their softening points. Annealing samples at each crystallization temperature and analyzing their x-ray diffraction peaks indicated that Te always crystallizes first, followed by GeTe.

B. Electrical Measurements

For d.c. conductivity measurements as a function of temperature, values of the current passed through the sample at a known voltage, usually 50V, were recorded at 10-20°C

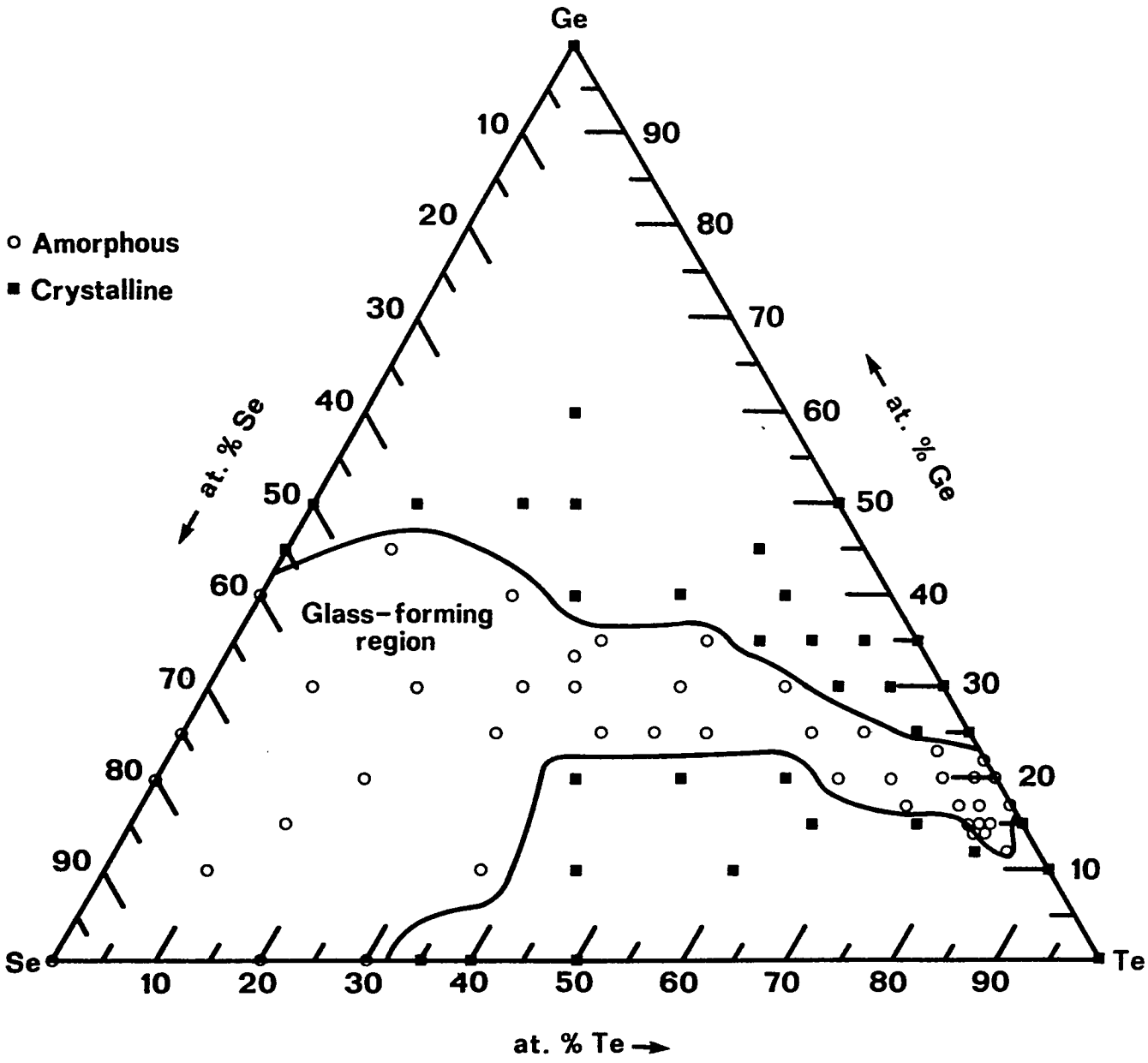

Figure 40. Phase diagram for the glass-forming region in the Ge-Se-Te system for one gram samples quenched from a 950°C melt in an ice bath.

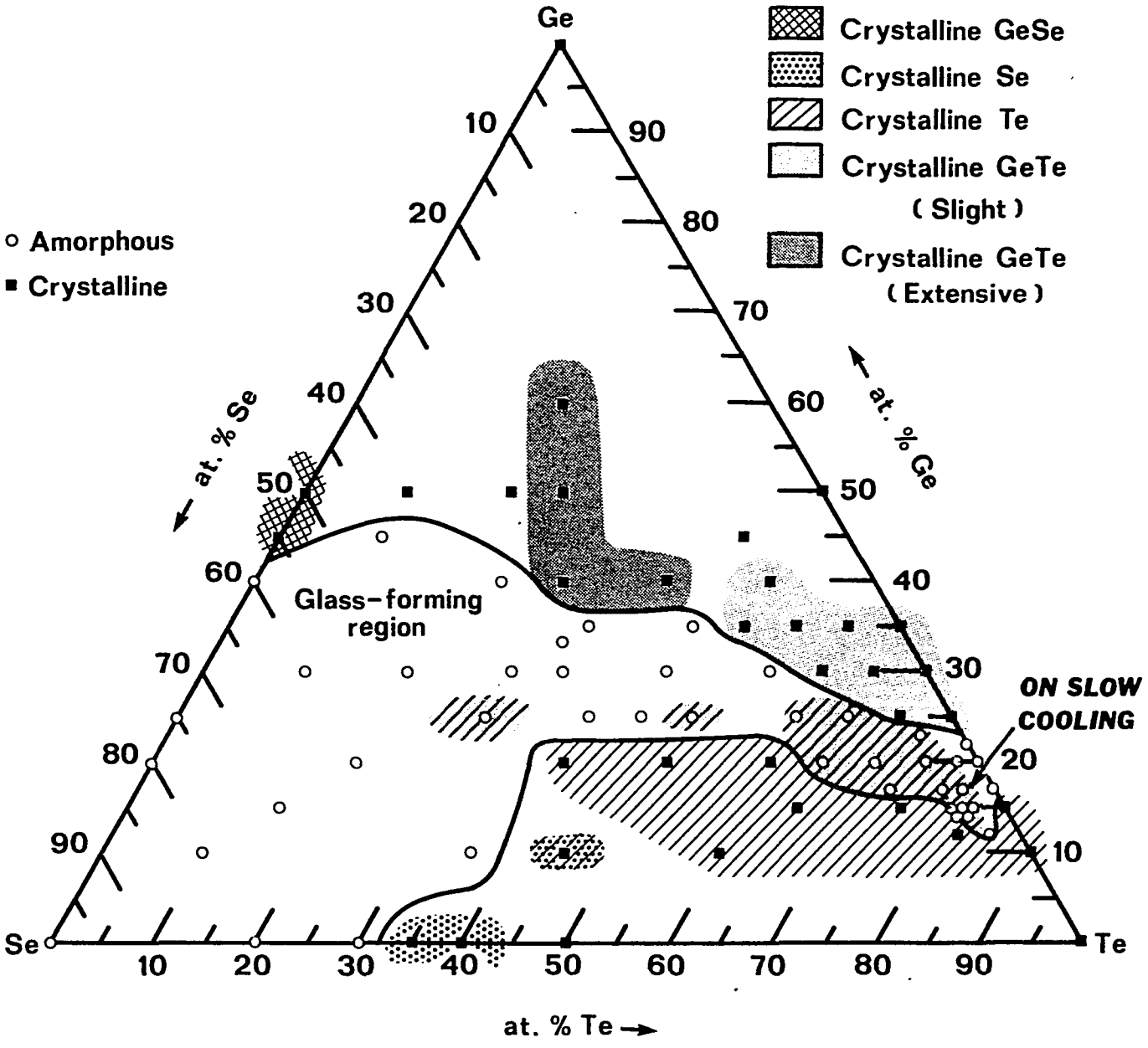

Figure 41. Phase diagram showing the compositions of the crystalline phases, including those obtained on slow cooling of otherwise amorphous compositions.

increments. At no time did the electric field across a sample exceed 100 V/cm. so that the current-voltage relation always remained ohmic.

After recording the d.c. current, the sample leads were switched into the a.c. bridge circuit and readings of the a.c. conductivity at a number of frequencies were taken. One of the small heaters at either end of the sample then raised the temperature at that end by ∿10°C and the TEP voltage across the gradient was measured.

This sequence of electrical measurements was repeated until a range of 100-150°C above the initial temperature had been covered. Depending on sample conductivity and consequent instrumentation sensitivity, initial temperatures ranged from -70°C to +50°C.

A calculator program (see Appendix) converted and plotted the conductivity data as log σ vs. $10^3/T$, and, after analyzing for deviations, calculated an activation energy for conduction from the least-squares slope of Equation (27). The calculated intercept represents the value of σ_o if the function were to remain linear at high temperatures, which it does not—instead, it drops off sharply, becoming temperature independent well before the intercept[67]. Another program (see Appendix) was used to plot the results from different glass compositions on common axes.

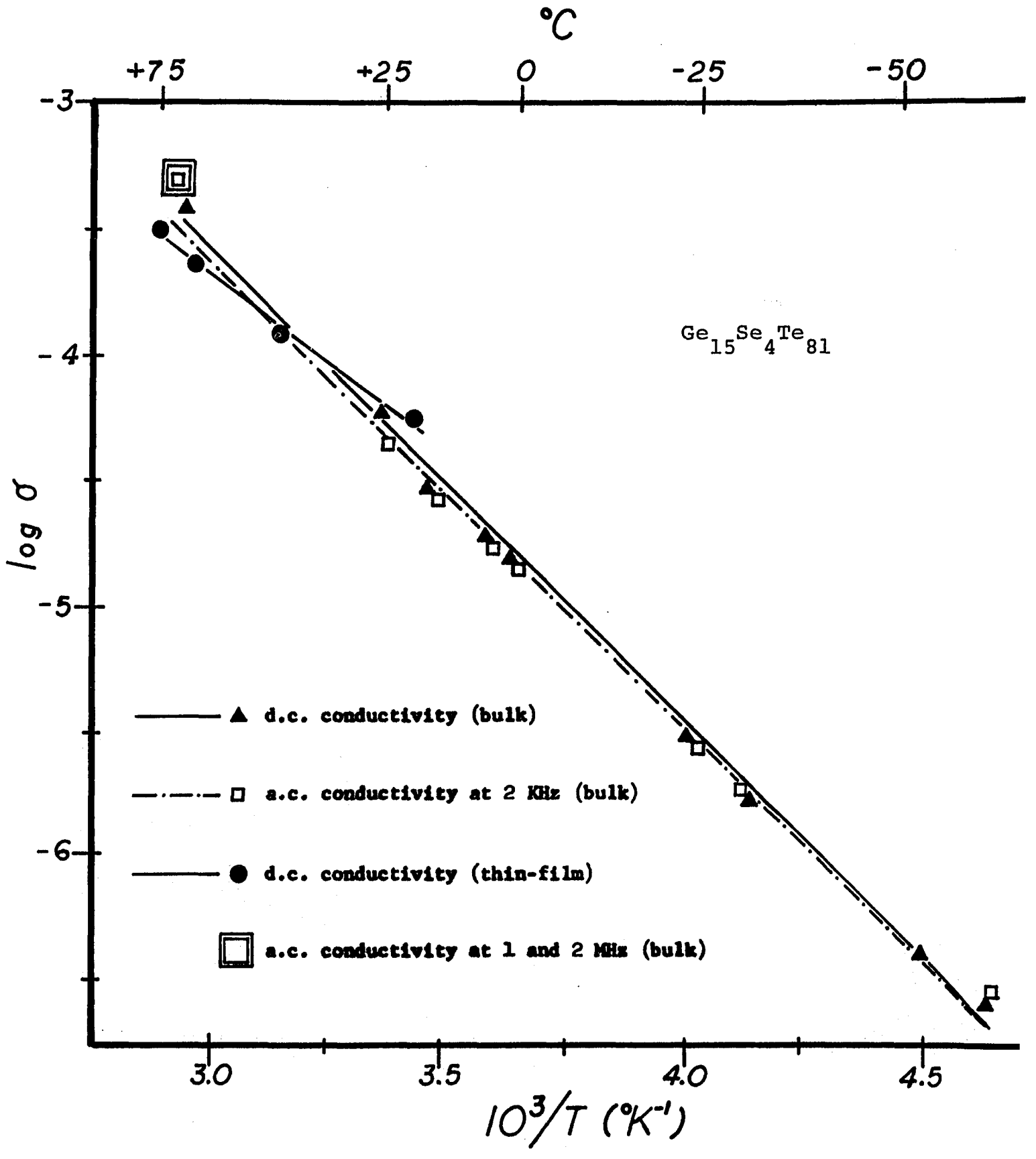

Figure 42. Conductivity as function of reciprocal temperature for bulk and thin-film samples of $Ge_{15}Se_4Te_{81}$.

Sample Composition:

$Ge_{15}Se_4Te_{81}$

	d.c., bulk	a.c., bulk	d.c., thin-film
Activation Energy, $\varepsilon_f - \varepsilon_v$ (in eV)	.38±.01	.36±.02	.26±.01
Intercept	2.106	1.780	.201
Slope	-1.905	-1.831	-1.294
S.D. in slope	.051	.082	.058
S.D. in intercept	.194	.307	.183
r.m.s. dev. in log σ	.070	.100	.019
Room-temperature conductivity, σ_{rt} $(ohm^{-1}-cm^{-1})$	5.8×10^{-5}	4.1×10^{-5}	$\sim 6 \times 10^{-6}$

Table 1. Conductivity data for $Ge_{15}Se_4Te_{81}$.

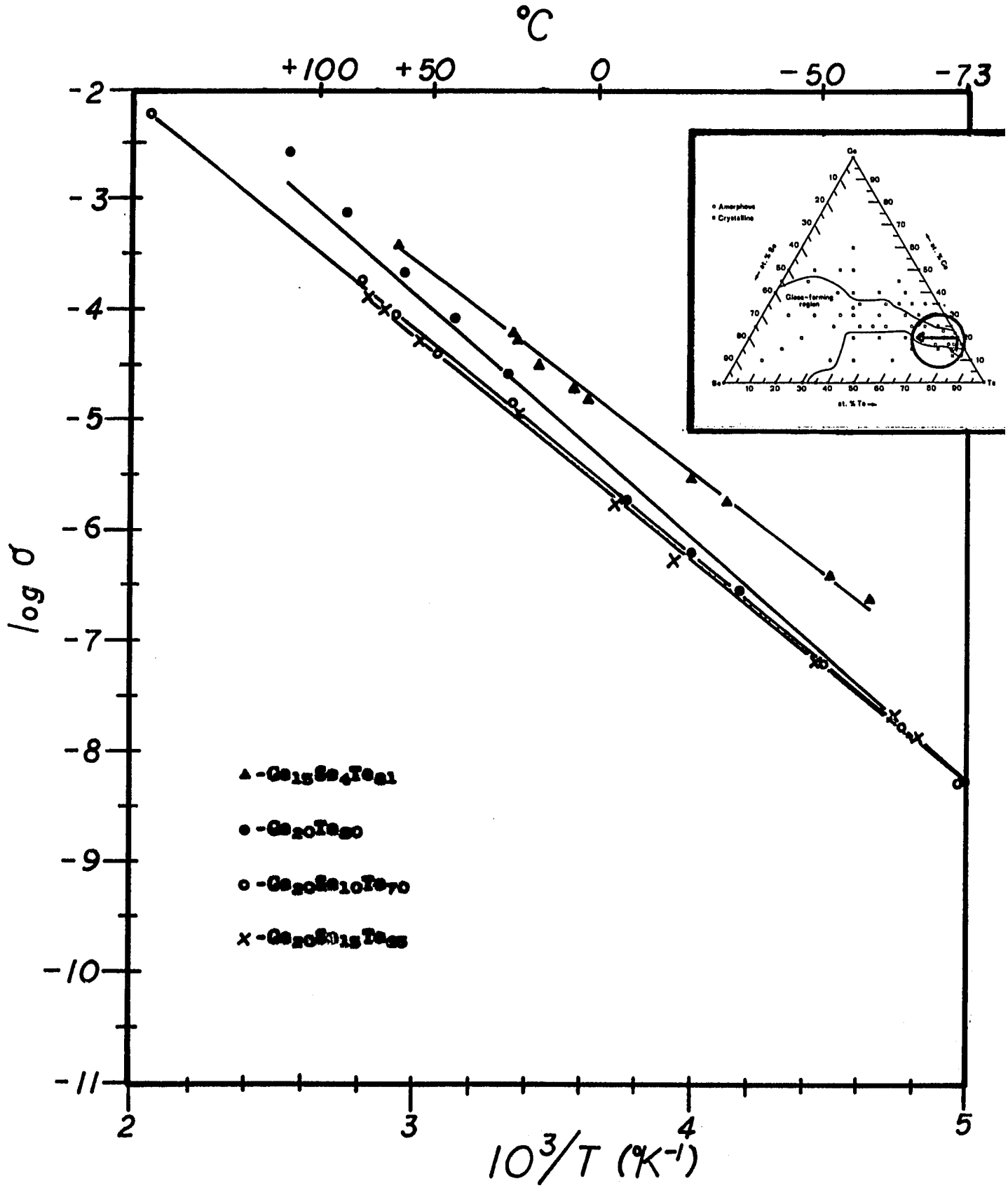

Figure 43. D.C. conductivity as a function of reciprocal temperature for a series of Ge-Se-Te glasses with compositions along the encircled line of the inset.

	$Ge_{15}Se_{04}Te_{81}$	$Ge_{20}Te_{80}$	$Ge_{20}Se_{10}Te_{70}$	$Ge_{20}Se_{15}Te_{65}$
Activation Energy, $\varepsilon_f - \varepsilon_v$ (in eV)	.38 ± .01	.45 ±.01	.42 ± .01	.41 ± .01
Intercept	2.106	3.045	2.218	1.924
Slope	-1.905	-2.287	-2.112	-2.040
s.d. in slope	.051	.067	.066	.067
s.d. in intercept	.194	.243	.208	.251
r.m.s. dev. in log σ	.071	.135	.196	.138
σ_{rt} (ohm^{-1}-cm^{-1})	5.8×10^{-5}	2.5×10^{-5}	1.2×10^{-5}	2.0×10^{-5}
Sign of thermoelectric power	positive	positive	positive	positive
Temperature (^oC) at which a.c. conductivity becomes measurable at:				
2 KHz	-60	-35	-40	---
20 KHz	---	---	+50	---
1 & 2 MHz	+70	+120	+85	+75
Density (g/ml)	5.2	5.4	5.9	5.6

Table 2. Summary of electrical measurements for the series of Ge-Se-Te compositions shown in Fig. 43.

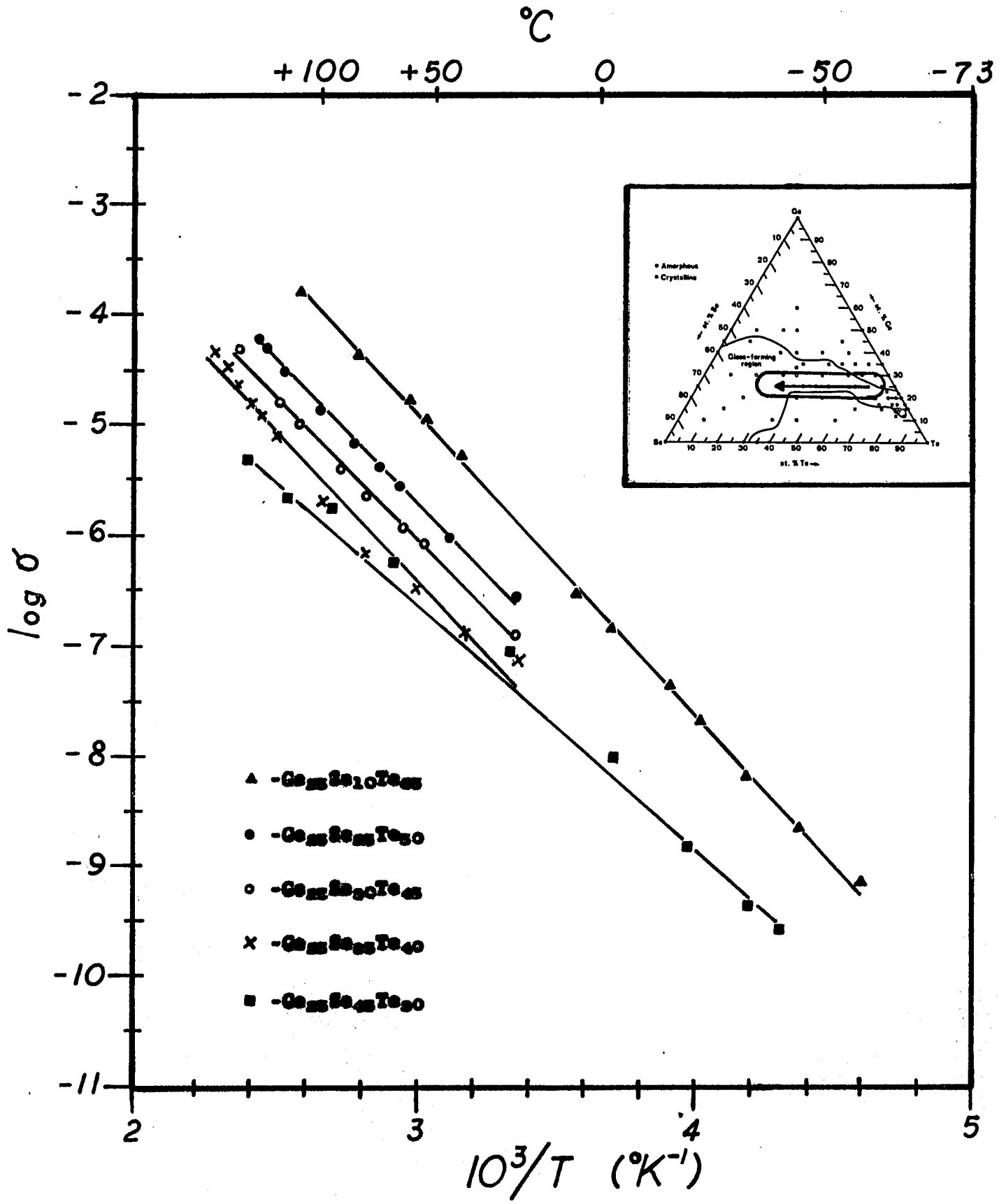

Figure 44. D.C. conductivity as a function of reciprocal temperature for a series of Ge-Se-Te glasses with compositions along the encircled line of the inset.

	$Ge_{25}Se_{10}Te_{65}$	$Ge_{25}Se_{25}Te_{50}$	$Ge_{25}Se_{30}Te_{45}$	$Ge_{25}Se_{35}Te_{40}$	$Ge_{25}Se_{45}Te_{30}$
Activation Energy, $\varepsilon_f - \varepsilon_v$ (in eV)	.54 ± .01	.51 ± .01	.51 ± .01	.53 ± .02	.48 ± .01
Intercept	3.229	1.992	1.583	1.557	.816
Slope	-2.712	-2.571	-2.548	-2.662	-2.413
s.d. in slope	.028	.058	.078	.127	.068
s.d. in intercept	.103	.160	.217	.341	.249
r.m.s. dev. in log σ	.057	.050	.057	.135	.089
$\sigma_{r.t.}$ (ohm^{-1}-cm^{-1})	1.6×10^{-6}	2.7×10^{-7}	1.3×10^{-7}	7.2×10^{-8}	8.5×10^{-8}
Thermoelectric Power	positive	positive	positive	positive	positive
Temperature (C) at which $\sigma_{a.c.}$ becomes measurable at:					
2 KHz	-15	---	+25	+65	+100
1& 1.5 MHz	+85	---	[1]n.s.	n.s.	n.s.
Density (g/ml)	5.4	4.9	4.9	4.5	4.3

[1]n.s. - instrumentation not sufficiently sensitive in temperature range.

Table 3. Summary of electrical measurements for the series of Ge-Se-Te compositions shown in Fig. 44.

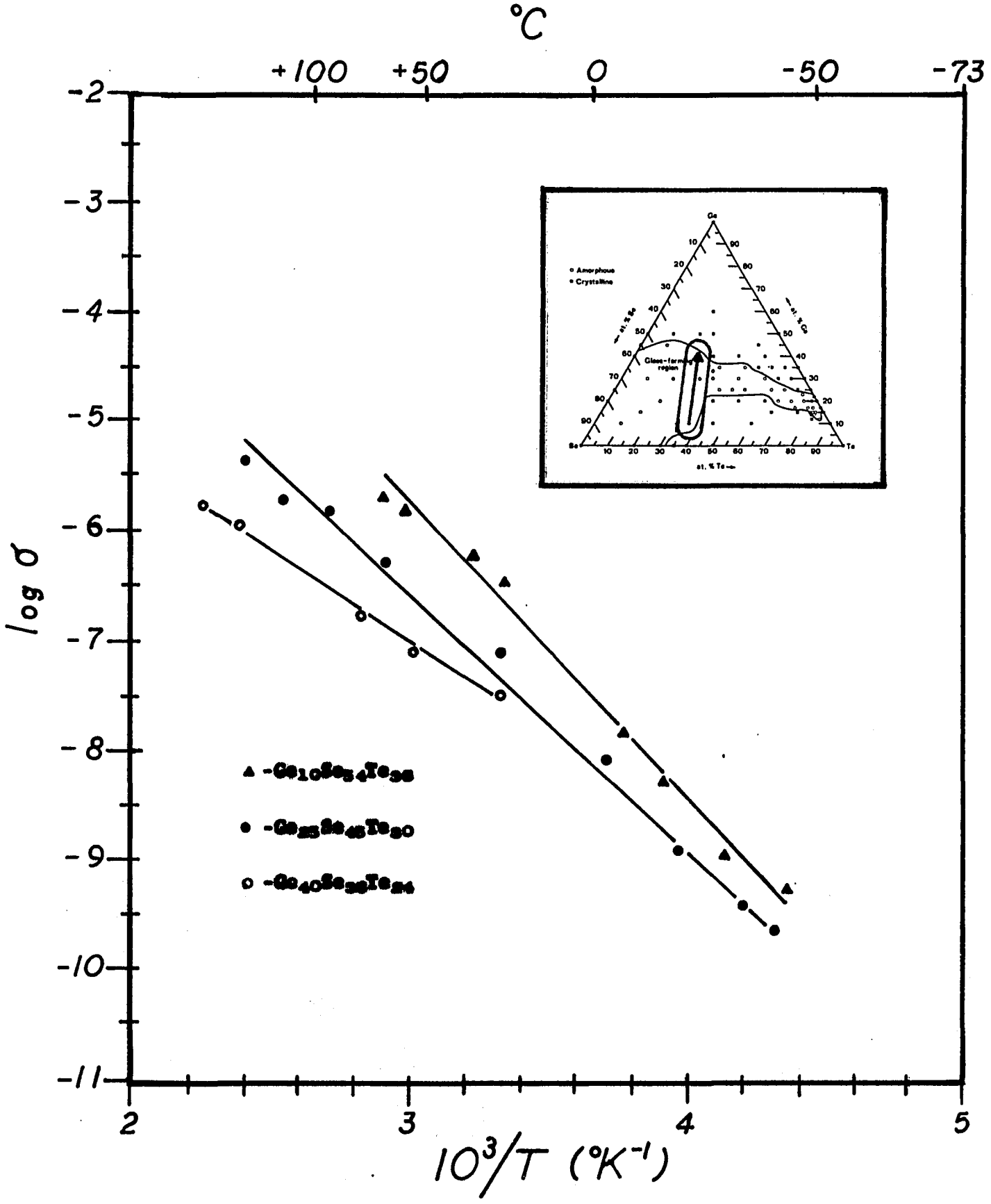

Figure 45. D.C. conductivity as a function of reciprocal temperature for a series of Ge-Se-Te glasses with compositions along the encircled line of the inset.

	$Ge_{10}Se_{54}Te_{36}$	$Ge_{25}Se_{45}Te_{30}$	$Ge_{40}Se_{36}Te_{24}$	$Se_{60}Te_{40}$	$Ge_{50}Se_{30}Te_{20}$
Activation Energy, $\varepsilon_f - \varepsilon_v$ (in eV)	.53 ± .03	.48 ± .01	.32 ± .02	---crystalline--	
Intercept	2.283	.186	-2.121	---	---
Slope	-2.661	-2.413	-1.618	---	---
s.d. in slope	.129	.068	.077	---	---
s.d. in intercept	.460	.249	.197	---	---
r.m.s. dev. in log σ	.166	.089	.050	---	---
$\sigma_{r.t.}$ (ohm^{-1}-cm^{-1})	3.9×10^{-7}	8.5×10^{-8}	3.7×10^{-8}	5.4×10^{-3}	4.2
Thermoelectric Power	positive	positive	[1]n.s.	---	---
Temperature at which $\sigma_{a.c.}$ becomes measurable at:					
2 KHz	+30	+100	+150	---	---
1 MHz	n.s.	n.s.	n.s.	---	---
Density (g/ml)	4.9	4.3	4.7	4.2	4.4

[1]n.s. - instrumentation not sufficiently sensitive in temperature range.

Table 4. Summary of electrical measurements for the series of Ge-Se-Te compositions shown in Fig. 45.

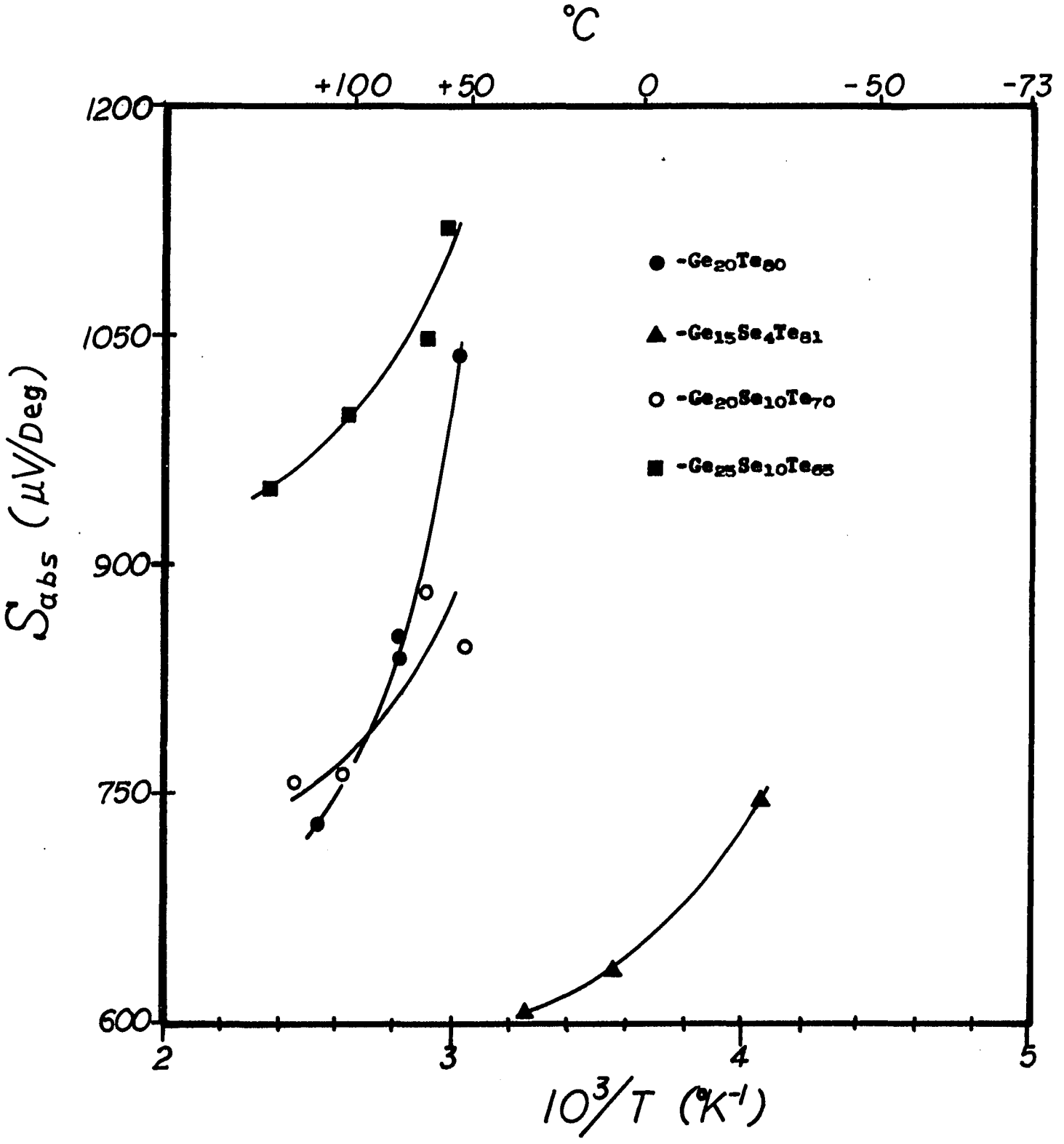

Figure 46. Absolute thermoelectric power, S, as a function of reciprocal temperature for some Ge-Se-Te glass compositions.

An example of the calculator plot made for $Ge_{15}Se_{4}Te_{81}$ appears as Figure 42 with the results appearing in Table 1. Data for different glass compositions are plotted in Figures 43-45 and summarized in Tables 2-4.

From the d.c. conductivity data it appears that the Te content is primarily responsible for the conductivity—the higher the per cent Te, the higher the conductivity (Table 3). This is not unexpected as Te, the most "metallic" of the group, tends to enhance the formation of the crystalline state as evidenced earlier by the phase diagram (Fig. 40) and later by DTA.

The Ge content appears to affect primarily the activation energy—the higher the per cent Ge, the lower the activation energy on an unannealed sample (Table 4). Increased Ge also decreases the conductivity somewhat. The tetrahedrally-bonding Ge forms extensive cross-linked networks which also strengthen the glass structure. As a result, conductivity vs. temperature trials on bulk glass samples with low Ge content found the sample ends indented; for example, $Ge_{10}Se_{54}Te_{36}$ had indented ends after a run reaching 160°C.

In all the trials, the a.c. conductivities paralled the d.c. values over the temperature range in which bridge sensitivity existed at frequencies between 0.5-50 kHz. As mentioned in the previous section, actual conductivities

at MHz frequencies could not be determined, but comparison of the values obtained with those generated by standard resistors indicated that even at these frequencies the a.c. and d.c. conductivities were identical. Besides, if there was a frequency dependence at the elevated temperatures measured, it should have manifested itself at the lower audio-frequencies. For compositions of As_2S_3 , increases of up to an order of magnitude in the conductivity accompany a frequency change of 10^3-10^4 Hz, and continue roughly linearly for each increase in the frequency order of magnitude[32].

In some of the Te-rich compositions, the room-temperature conductivity was slightly higher after a trial run, even though the sample was not heated to the softening temperature indicated by DTA.

Earlier samples of $Ge_{10}Se_{54}Te_{36}$, $Ge_{25}Se_{45}Te_{30}$, and $Ge_{40}Se_{36}Te_{24}$ that were run without evaporated gold electrodes, just copper pressure contacts, exhibited room-temperature conductivities after a run that were sometimes higher, sometimes lower than those before the run by as much as two orders of magnitude. There were also corresponding changes in activation energies. Despite this seemingly haphazard behavior, there were no further changes on subsequent heating of the samples as long as the highest temperatures of preceding runs were not exceeded. Furthermore, the values for the activation energies for the three compositions appeared to approach 0.60 eV, 0.62 eV, and 0.70 eV respectively after a series of runs. Perhaps these metastable glasses with a

substantial Se content (melting point 217°C) were beginning to anneal at the higher temperatures of 120-170°C to a common, more stable structure.

Thermoelectric power measurements, where instrumentation sensitivity permitted, were always positive, indicating holes as the majority carriers. However, some of the plots of S vs. $10^3/T$ were of doubtful value because of the uncertainty in measuring TEP voltages across high-resistance samples, a difficulty encountered by other workers and noted by Mott[14]. The better determinations appear in Figure 46, but activation energies calculated from their slopes according to the linear relation given by Equation (39) appear in parentheses in Table 5.

C. Optical Measurements

In order to obtain satisfactory results on the width of the band gap from optical data, the absorption coefficient α is plotted against photon energy $\hbar\omega$ as in Equation (42), or $(\alpha\hbar\omega)^{1/n}$ vs. $\hbar\omega$ as in Equation (48) where $n = 2$ or 3 depending on the fit, and A is a constant[34].

$$\alpha = \frac{A}{\hbar\omega}(\hbar\omega - \Delta\varepsilon_o')^n \qquad (48)$$

The linear part of the curve is extrapolated to the point at which it intersects the energy axis. The value at that point is taken as $\Delta\varepsilon_{opt}$.

In order, however, to obtain α, Equation (40) must be solved by either measuring T and R as a function of wavelength for a known sample thickness, or by measuring only T as a function of wavelength for different thicknesses of the same sample and solving simultaneously for α. The latter method is valid only if R remains constant for different thicknesses, as is the case in thicker films where R drops off rapidly beyond the front surface and the rear surface is too far to contribute.

Figure 47 illustrates the transmission spectra of different thicknesses of $Ge_{1.5}Se_4Te_{8.1}$ film. Note that the second peak in the thicker film is lower than that in the thinner film. This is as it should be, indicating greater absorption with increasing film thickness. The first peak, by analogy to Ge amorphous films[75], is due primarily to changing reflection with wavelength, and is obviously not constant for these two thicknesses. Apparently, still thicker films are required. Determinations with thin bulk sample disks were unsuccessful as their small diameters did not permit sufficient light through to activate the spectrophotometer.

Figures 48 and 49 show the transmission spectra of different samples cast as thinner films in an earlier attempt to measure both T and R for a specific thickness. Reflectance spectra of these samples were made with different standards, first MgO, then half-silvered slides,

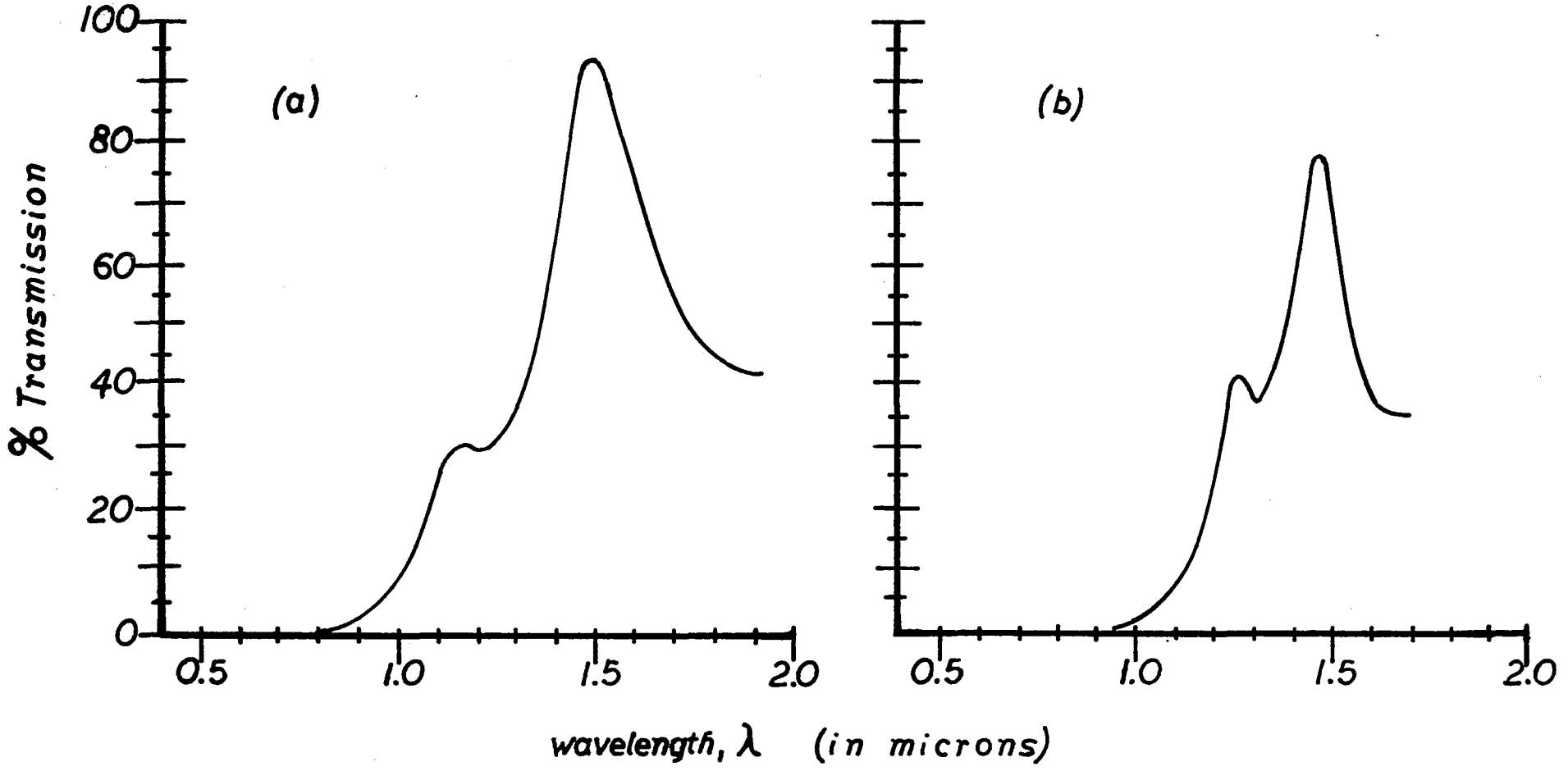

Figure 47. Optical transmission as afunction of wavelength for thin films of composition $Ge_{15}Se_4Te_{81}$ with thicknesses of (a) 5600 Å and (b) 11200 Å.

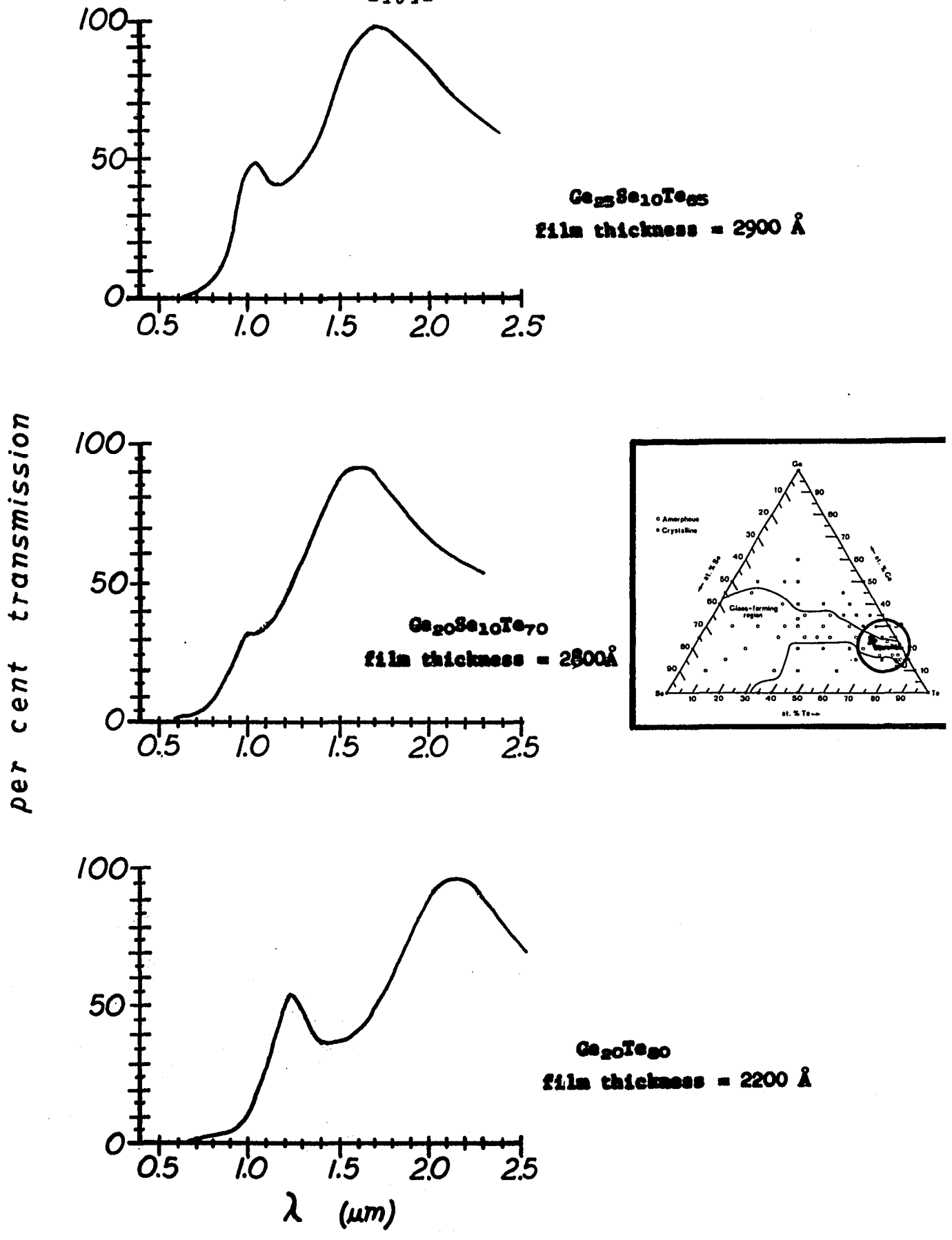

Figure 48. Optical transmission as a function of wavelength for a series of Ge-Se-Te thin films with compositions along the encircled line of the inset.

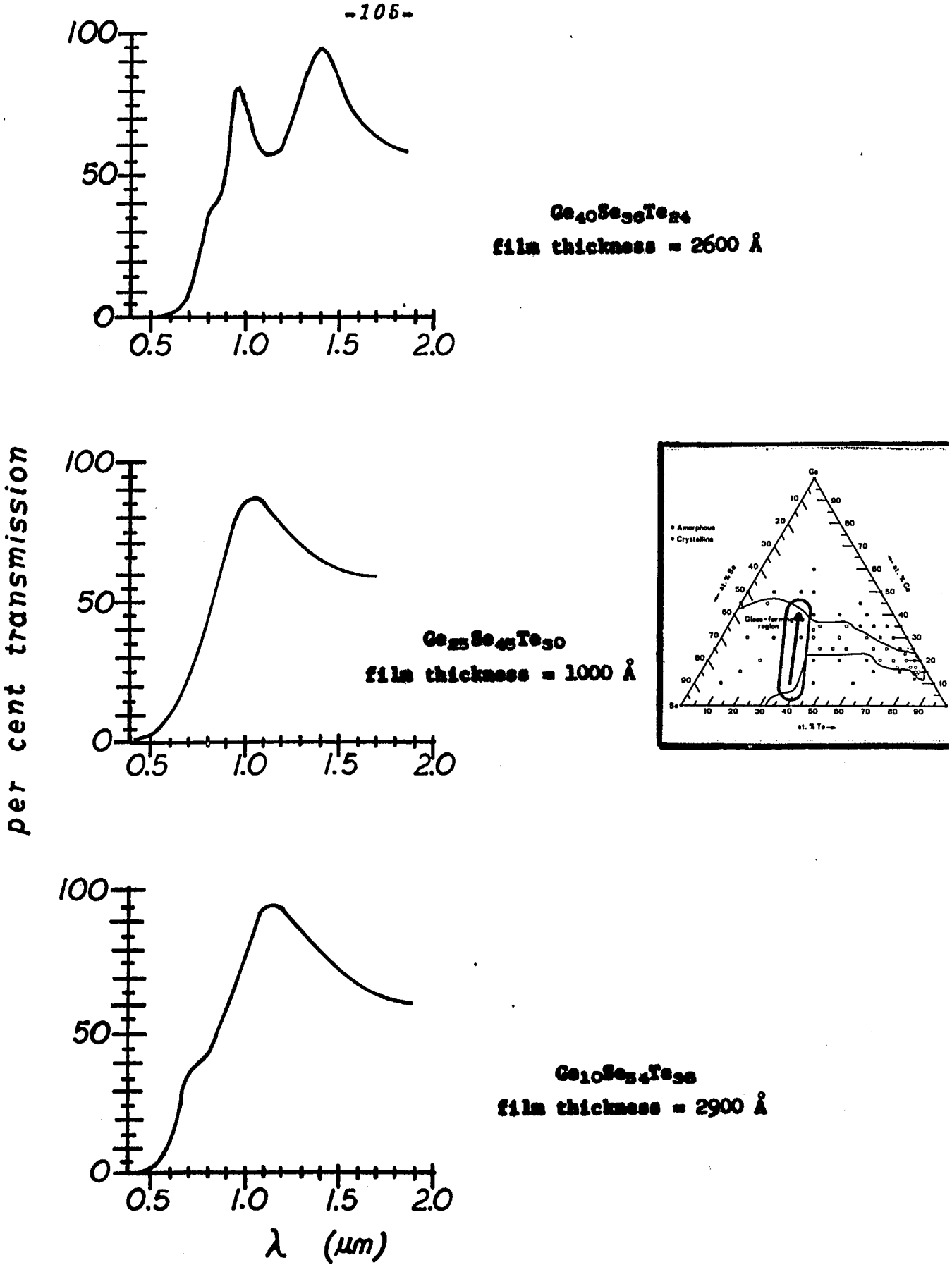

Figure 49. Optical transmission as a function of wavelength for a series of Ge-Se-Te thin films with compositions along the encircled line of the inset.

followed by full-silvered slides. The results indicated that, while reflectance peaks occurred in the right places, their magnitudes were meaningless and could not be used in Equation (40).

Nevertheless, an estimate of $\Delta\varepsilon_{opt}$ can be made by assuming that absorption is near maximum at or slightly to the right of the first peak. Taking the energy at which the first peak occurs as the band gap, yields values for an activation energy, $\Delta\varepsilon_{opt/2}$ given in Table 5,that correspond to a band gap which would have its Fermi level midway between the valence and conduction bands.

Before comparing values determined from film compostions to those determined from bulk samples, EMPA was used to confirm the concentrations of the bulk and film samples. The results in Table 6, listed in order of film preparation, indicate that Te-poor bulk samples that were evaporated later, nevertheless, yielded films which were overly rich in Te. This was probably due to the fact that Te-rich vapor from earlier Te-rich bulk compositions condensed in and on the quartz chute leading to the hot crucible, and on subsequent evaporations vaporized, enriching the Te content of the vapor from the last few samples. With this established, Table 7 compares $\Delta\varepsilon_{opt/2}$ with the conductivity-determined activation energies for the bulk samples closest in composition to the EMPA-determined film compositions.

Subtracting the activation energy for hole conduction from the energy band gap $(\varepsilon_c-\varepsilon_v)_{opt}$, yields the activation energy for electron conduction, $\varepsilon_c-\varepsilon_f$. The result in all

At. % Ge	Se	Te	$(\varepsilon_f - \varepsilon_v)_{\sigma_{d.c.}}$	$\Delta\varepsilon_{opt}/2$	[1] $(\varepsilon_f - \varepsilon_v)_{TEP}$
[2] 15	4	81	.26	.492	---
15	4	81	.38	.492	(.26)
20	0	80	.45	.504	(.43)
20	10	70	.42	.620	(.44)
20	15	65	.41	---	---
25	10	65	.54	.590	(.32)
25	25	50	.51	---	---
25	30	45	.51	---	---
25	35	40	.53	---	---
10	54	36	.53	.530	---
25	45	30	.48	.602	---
40	36	24	.32	.626	---

[1] ( ) - Calculated from the slopes of the thermoelectric power data curves assuming the points lie along a straight line.

[2] Thin-film sample

Table 5. Activation energies, $\varepsilon_f - \varepsilon_v$ (in eV), for hole creation in the valence band of Ge-Se-Te glasses, as determined from d.c. conductivity, optical absorption, and TEP measurements.

Element	Atomic %			
	Unreacted Mixture	Powdered Sample Bulk[1]		After Evaporation Thin-film[2]	
Ge	15	16.6	16.5	13.4	12.7
Se	4	5.6	5.9	5.5	5.3
Te	81	77.8	77.6	81.1	82.0
Ge	20	19.2	19.3	16.7	14.4
Te	80	80.8	80.7	83.3	85.6
Ge	20	19.9	18.6	17.2	15.7
Se	10	12.4	10.2	10.4	10.6
Te	70	67.7	71.2	72.4	73.7
Ge	25	27.0	26.6	21.8	20.2
Se	10	11.2	11.6	10.3	8.5
Te	65	61.8	61.8	67.9	71.3
Ge	10	29.7		20.7	
Se	54	41.4		38.7	
Te	36	28.9		40.6	
Ge	25	27.8		21.4	
Se	45	42.1		41.0	
Te	30	30.1		37.6	
Ge	40	40.7		22.0	
Se	36	33.1		17.6	
Te	24	26.2		60.4	

[1] Analysis performed on different particles of powdered sample.
[2] Analysis performed at different points on film surface separated by ∿1 cm.

Table 6. Electron microprobe analyses of powdered bulk samples and the films prepared from them by evaporation. (Analyses performed at Mag. 740X, corresponding to volume elements of ≈8 x 10^{-8} cm^3).

Assumed film Composition	EMP Analysis	Closest bulk Composition	$\Delta\varepsilon_{opt}/2$	$(\varepsilon_c - \varepsilon_v)_{opt}$	[1] $(\varepsilon_f - \varepsilon_v)_\sigma$	$(\varepsilon_c - \varepsilon_f)$
			(eV)	(eV)	(eV)	(eV)
At.% Ge-Se-Te	At.% Ge-Se-Te	At.% Ge-Se-Te				
15-04-81	13-05-82	15-04-81	.492	.984	.38	.60
20-00-80	15-00-85	20-00-80	.504	1.008	.45	.56
20-10-70	16-11-73	20-10-70	.620	1.240	.42	.82
25-10-65	21-09-70	20-10-70	.590	1.180	.42	.76
40-36-24	22-18-60	20-15-65	.626	1.252	.41	.84
10-54-36	21-39-40	25-35-40	.530	1.060	.53	.53
25-45-30	21-41-38	25-35-40	.602	1.204	.53	.67
	Mean Value:		.566 ±.049	1.132 ±.098	.45 ±.05	.68 ±.10

[1] The value used for $(\varepsilon_f - \varepsilon_v)_\sigma$ is the one obtained for the bulk sample composition closest to that given by EMP analysis of the thin film.

Table 7. Approximate values for $\varepsilon_c - \varepsilon_v$ and $\varepsilon_c - \varepsilon_f$ for a number of Ge-Se-Te glass compositions as determined from d.c. conductivity and optical absorption data.

cases gives $\varepsilon_c - \varepsilon_f > \varepsilon_f - \varepsilon_v$ as proposed by the various density-of-states models advanced to describe amorphous semiconductors (Sec. II, B.). The resulting number of holes outnumber the electrons since $e^{-(\varepsilon_f - \varepsilon_v)} > e^{-(\varepsilon_c - \varepsilon_f)}$ and hole conduction predominates as evidenced by the TEP data.

Of course, this is all predicated on the assumption that the absorbance maximum lies near the first peak in the transmission spectrum. It would, however, have to be at or beyond the second peak in order that $\varepsilon_c - \varepsilon_f \leq \varepsilon_f - \varepsilon_v$, which is not likely as these glasses transmit readily in the infrared[49].

D. Switching

Use of EMPA[76] and x-ray mapping was extended to switching experiments to determine whether sample composition in the area of the electrodes changes as a result or perhaps the cause of the formation of conducting crystalline filaments in the low resistance state of the glass. A composition. for example, rich in Te content and lying near the edge of the glass-forming region might, upon switching, become further enriched in Te content just sufficiently to place it on the crystalline side of the region. A small crystalline channel thus formed would be responsible for the "memory" in a memory device[77]. Many of the devices mentioned in the literature do contain disproportionately large amounts of Te, 48 at. % in quaternary (threshold) devices[3], and up to 82 at. % in ternary (memory) devices[43].

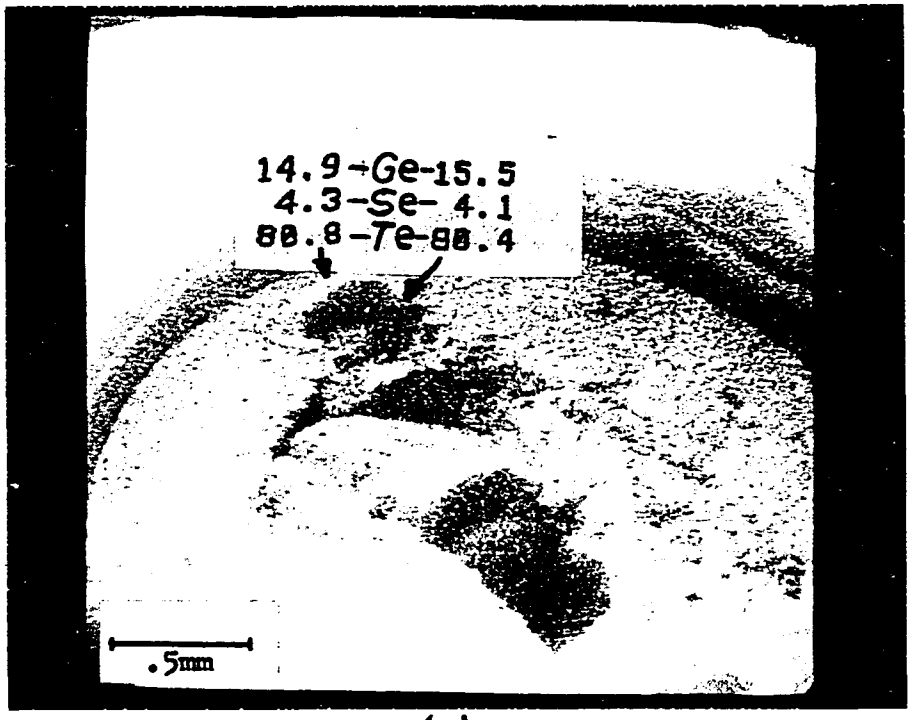

(a)

(b)

Figure 50. (a) Electron microprobe analysis and electron micrograph of a $Ge_{15}Se_4Te_{81}$ disk in its quartz collar (Mag. 35X). (b) Micrograph made by collecting $Te_{L_{\alpha,\beta,\gamma}}$ x-rays. (Without restorer/rejector; 1 min. count).

In Figure 50, electron and x-ray micrographs of a Te-rich glass, together with microprobe analysis results of the glass composition at two nearby points on the glass surface are given.

Before performing a switching experiment within the SEM, a number of trials were first made using a light microscope to monitor changes in the surface near the electrodes. Figure 51 illustrates a series of current vs. voltage curves generated for a sample of $Ge_{15}Se_{4}Te_{81}$ using the circuit diagrammed in Figure 36 ($R_1 = 10^5$ kΩ; $R_2 = 10^3$ kΩ). Curves (1) and (2) represent the high resistance state. A quick pulse of 150 V across the sample at this point resulted in a very fine filament between the electrodes, visible under the light microscope; resistance was still high. Gradual increase of the voltage this time led to switching along curve (3) to a lower resistance state [curve (4)]. A high current pulse delivered at 350 V across a 100Ω resistor in series with the sample partially restores the high resistance state [curve (5)]. Replacing the resistor with a larger one, 10 kΩ, and again applying a 350 V pulse yields curve (6), the lowest resistance state. At this point, the light microscope reveals the formation of an elliptical ring on the sample surface with one electrode on the ring and the other at a focal point. Curves (7), (8), and (9) represent unsuccessful attempts to restore the original high resistance state with high current pulses, which seemed to only heat the electrode area, broadening the ring and causing the outer

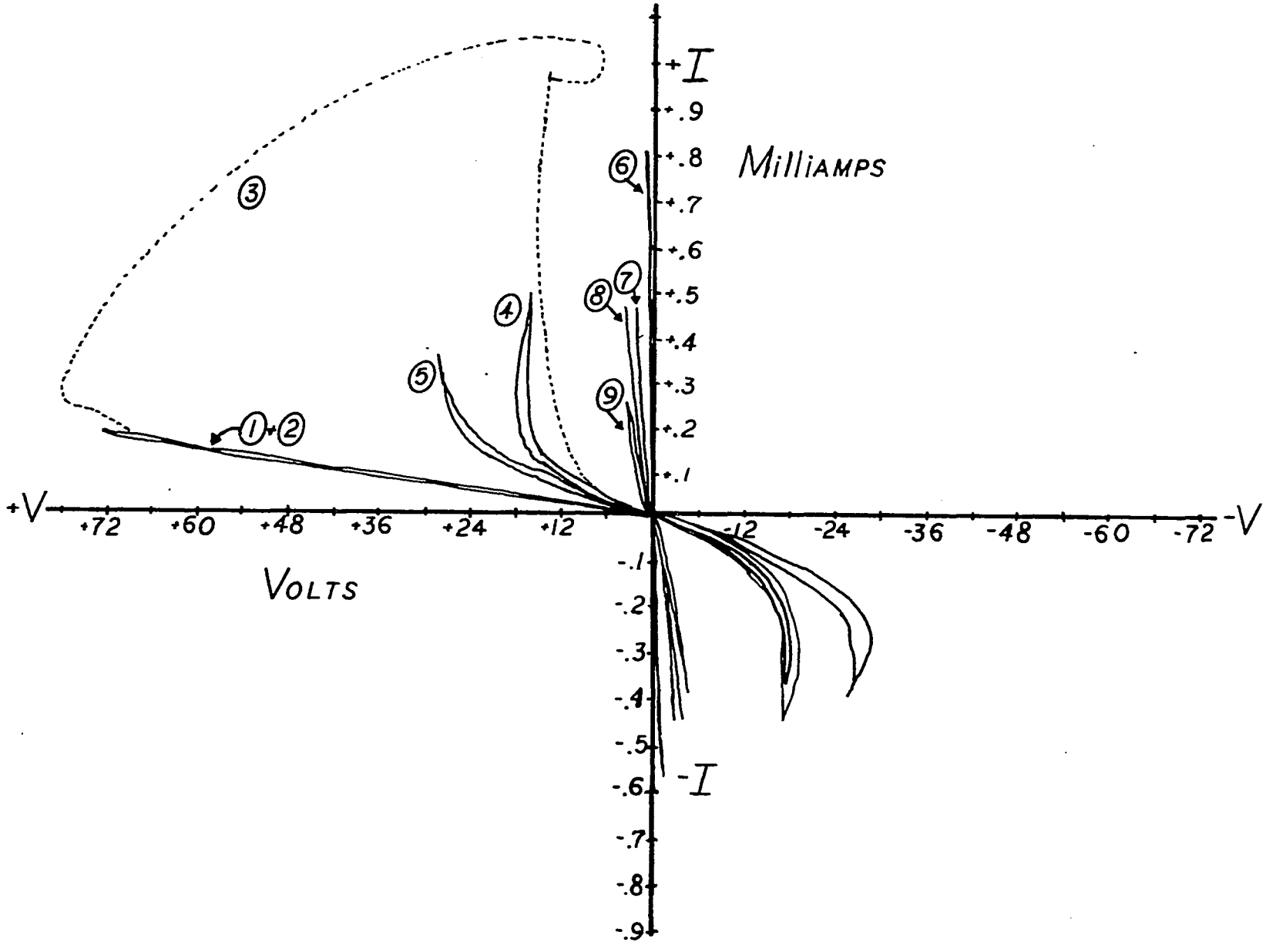

Figure 51. X-Y recorder trace of nine successive current vs. voltage curves for a bulk sample of $Ge_{15}Se_4Te_{81}$ with tungsten point contacts 170μm. apart.

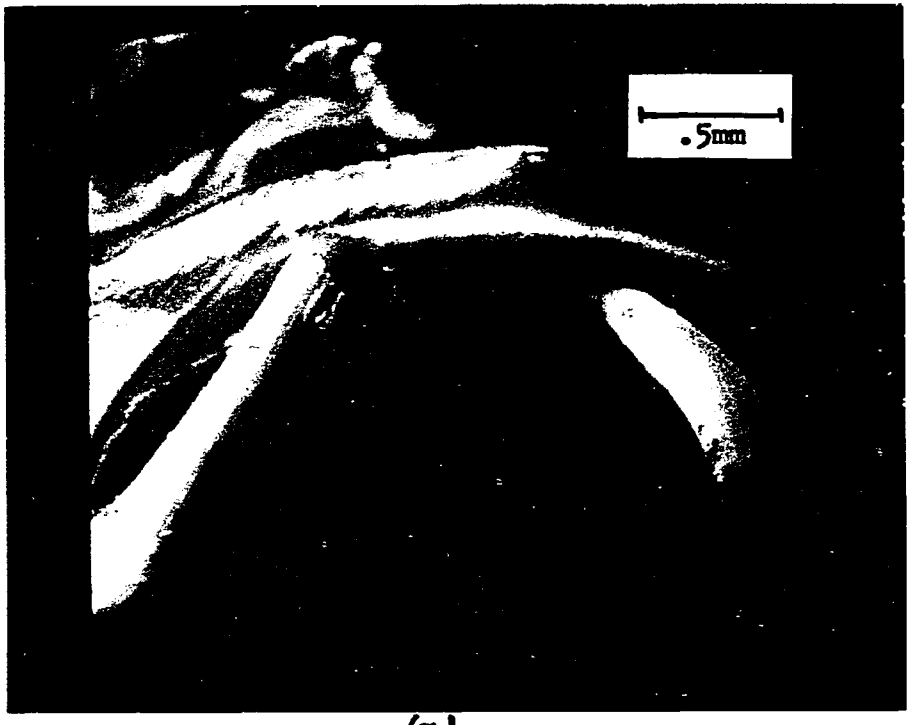

(a)

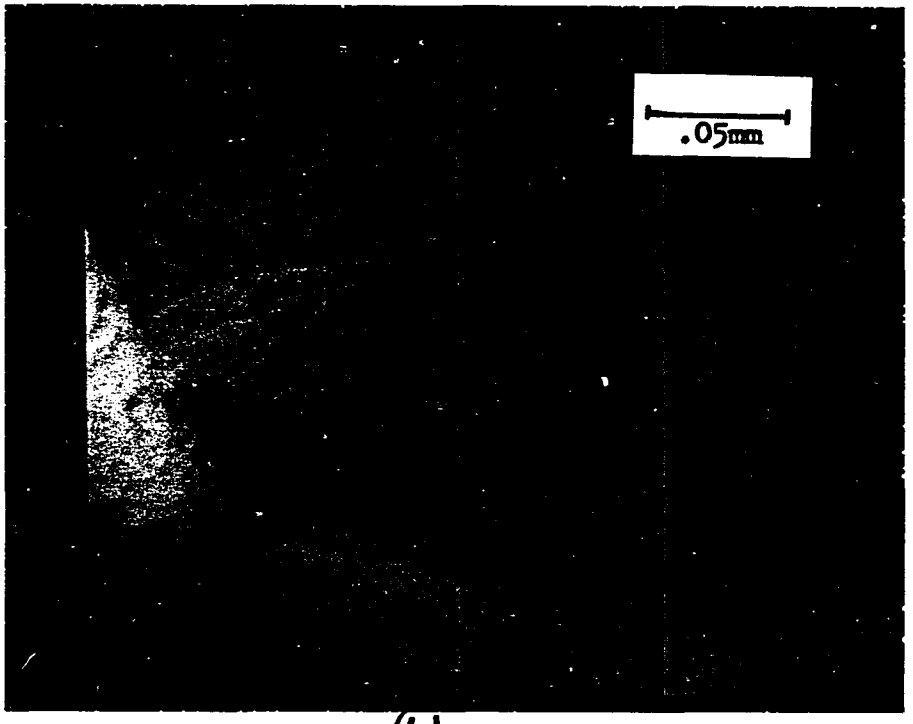

(b)

Figure 52. Electron micrographs of bulk sample of $Ge_{15}Se_4Te_{81}$ in low resistance state after multiple switching events of Fig.51, showing extensive heating effects. (a) Tungsten electrodes 170μm apart (Mag. 35X). (b) Closeup view of area between the electrodes (Mag. 350X).

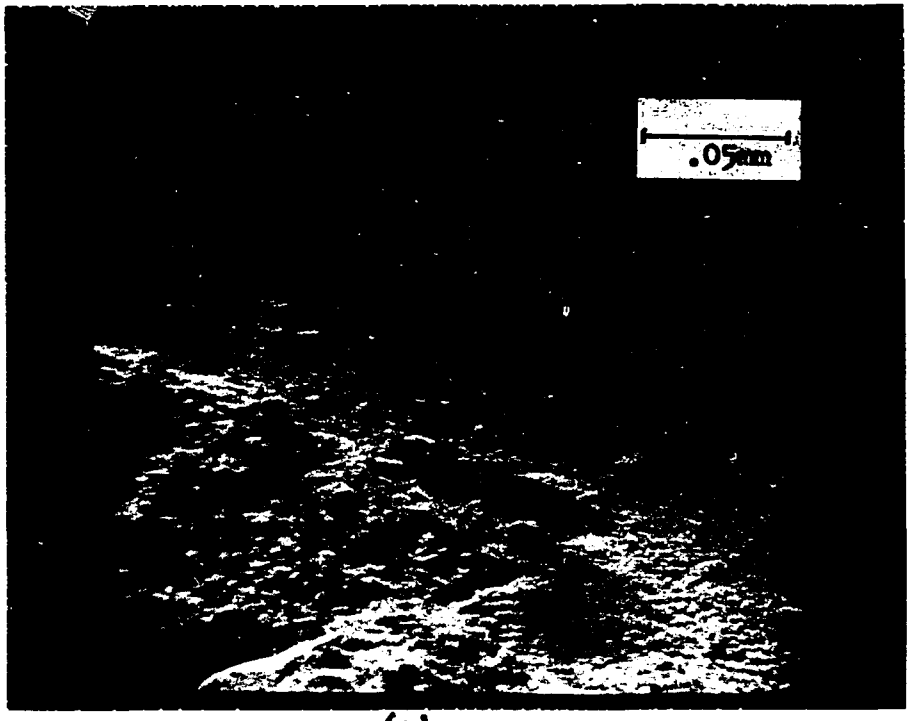

(c)

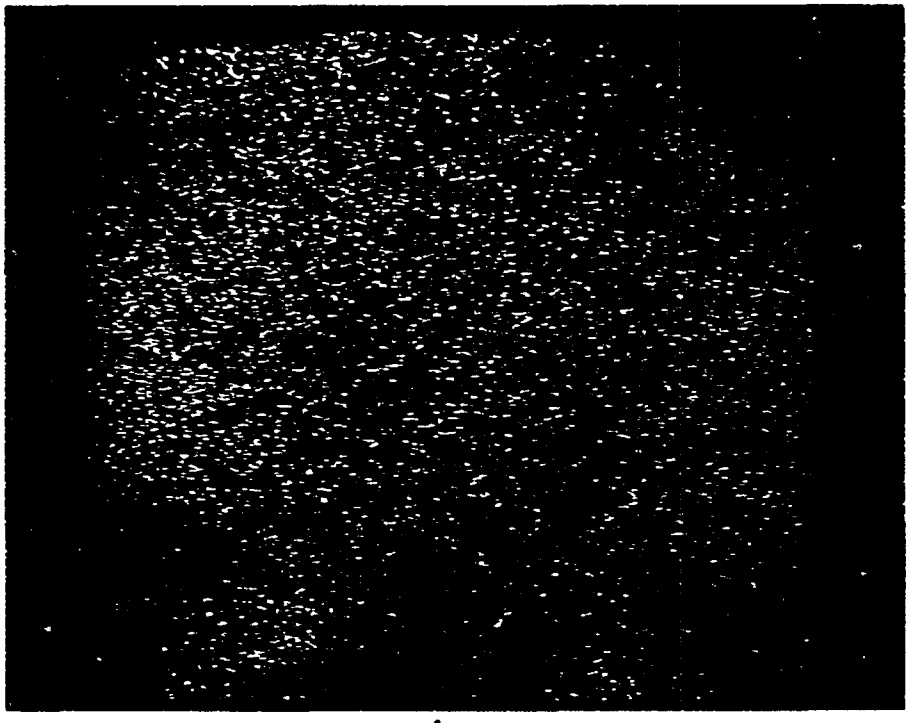

(d)

Figure 52, cont'd. (c) Area to the upper right of micrograph (b) viewed with the electrode removed (Mag. 360X). (d) X-ray micrograph of Te distribution in area (c). (Without restorer/rejector; 10 sec. exposure).

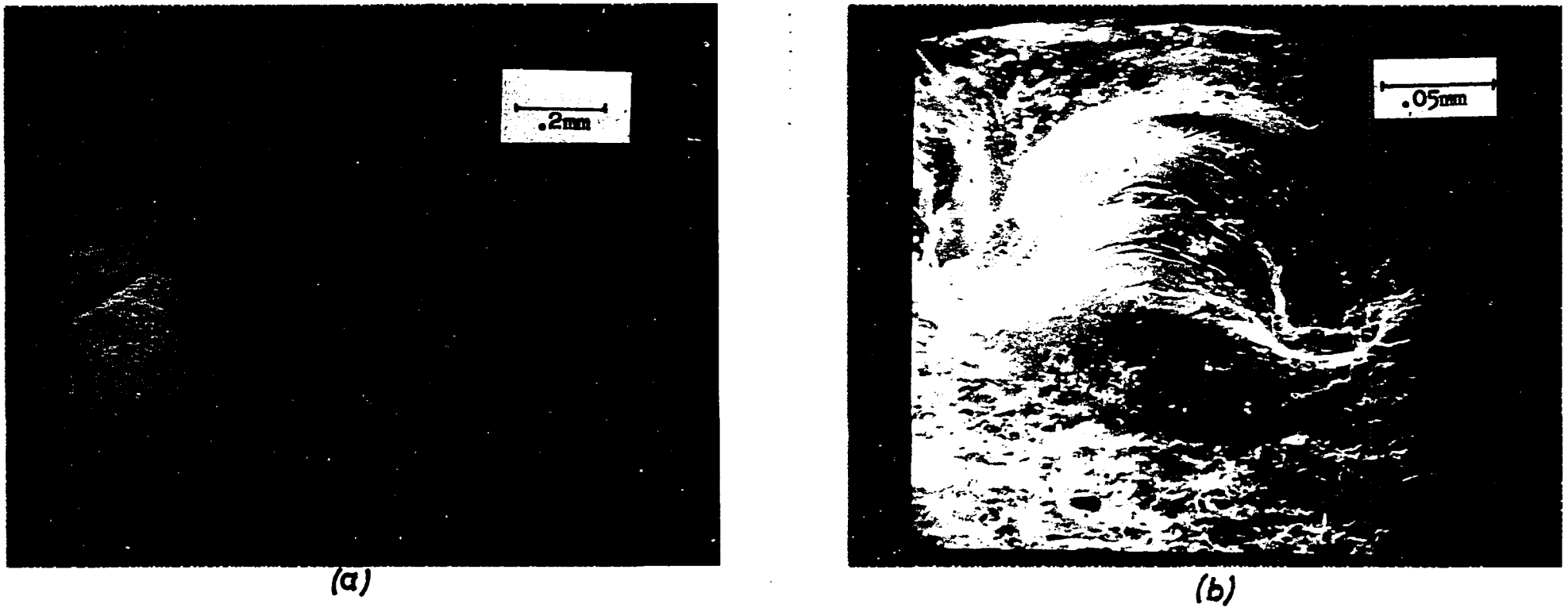

Figure 53. Electron micrograph of bulk sample of $Ge_{15}Se_4Te_{81}$ at a different spot, again in a low resistance state after a sequence of pulses similar to those in Fig. 51. (a) Low magnification (73X) of indented area where point electrodes made contact. (b) Close-up view of area between the electrodes (Mag. 360X; 170μm. between indentation centers).

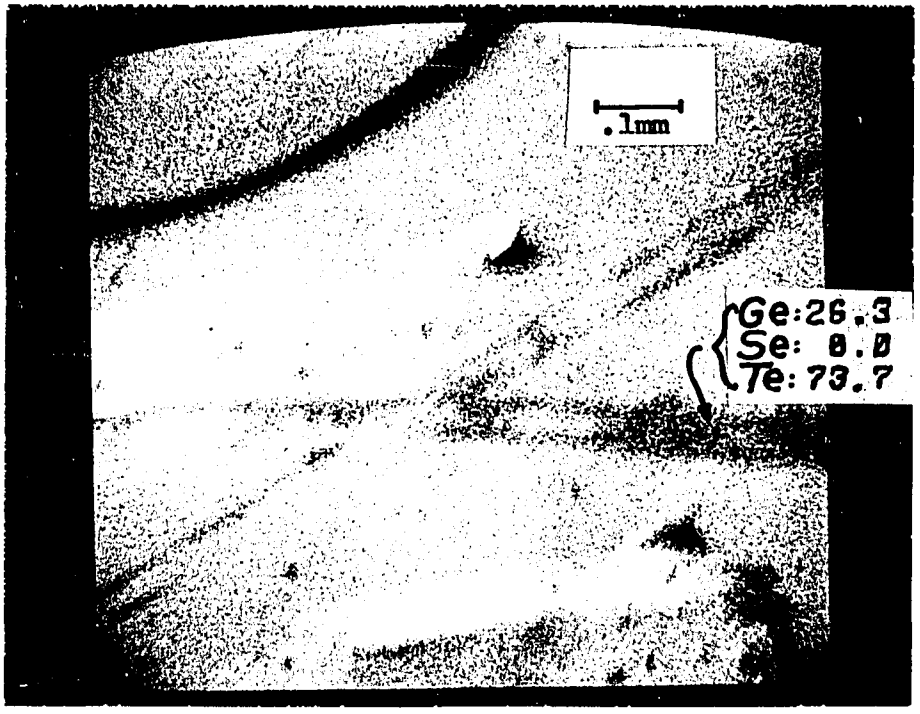

Figure 54. Electron micrograph of a thin film of $Ge_{20}Te_{80}$ (dark area in X) beneath thin-film gold electrodes with a gap spacing of 50μm. Seen here after device failure due to excessive heating of plastic substrate under a switching pulse. Indium bulk electrodes cold-soldered to the gold surface appear at the top and bottom of the picture (Mag. 100X).

electrode to burrow into the surface. Figure 52 shows the electrode area, where the ring appears to be an area fused from the heat. Figure 52(d) does not shed any light on whether the ring, presumably crystalline, contains a particularly rich vein of tellurium.

The results of other switching trials appear in Figures 53 and 54. In the latter, the plastic substrate supporting the thin-film sample apparently melted. This is not surprising, as estimates of the temperature jump during switching range from 500°C[46] to 900°C[66] (the plastic softens at 175°C).

Figure 55 represents a trial *in situ* in the SEM. As before, the current vs. voltage relation is ohmic before and after switching and is independent of polarity.

Figures 56.1 - .4 follow the transitions between the high resistance state and the low one. Note the heating effect opening up a successively larger crevice beneath the upper right electrode. The lack of filament formation may be attributed to the fact that the tungsten points of the electrodes where the electric field is greatest lie beneath the sample surface. Structural changes relegated to that area are, therefore, not seen visually—nor readily detected as composition changes by EMPA or x-ray mapping. By Figure 56.4, after a number of switching events, a filament between the electrodes appears as an indentation of the surface. EMPA of the area indicates a slight enrichment in the Te

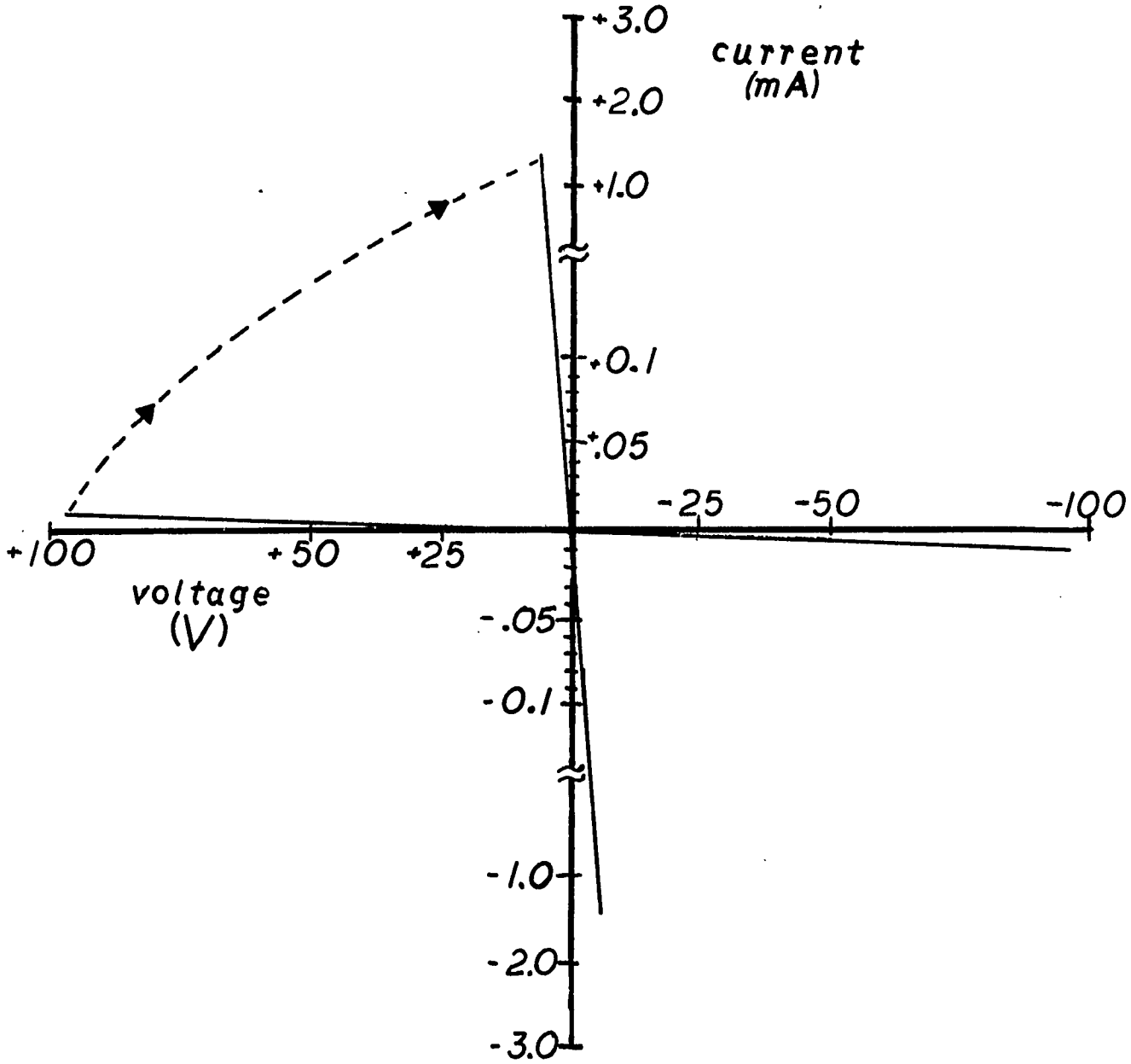

Figure 55. Current vs. voltage curve for a bulk sample of $Ge_{15}Se_4Te_{81}$ before and after switching along the dashed line.

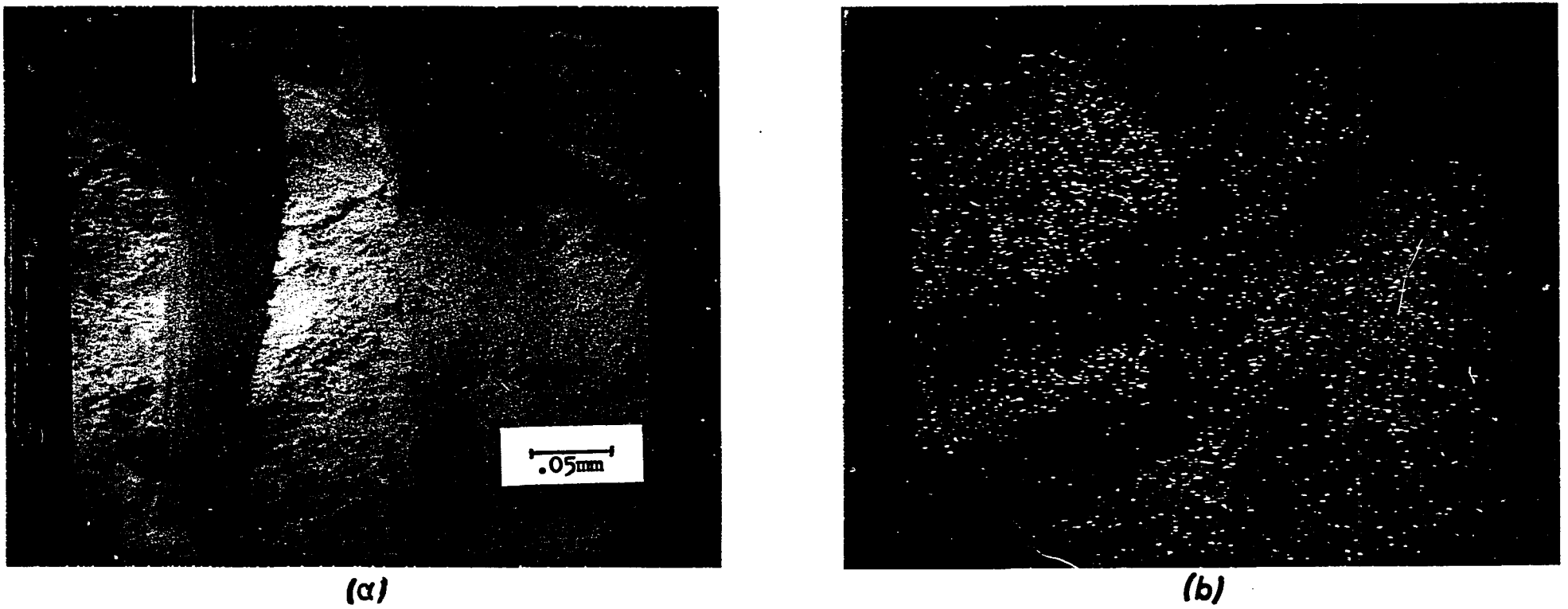

Figure 56.1 (a) Electron micrograph of the area near the electrodes (200μm. apart) for sample $Ge_{15}Se_4Te_{81}$ before switching (Mag. 250X). Sample resistance was $1.3 \times 10^7 \Omega$. (b) X-ray micrograph of Te distribution.

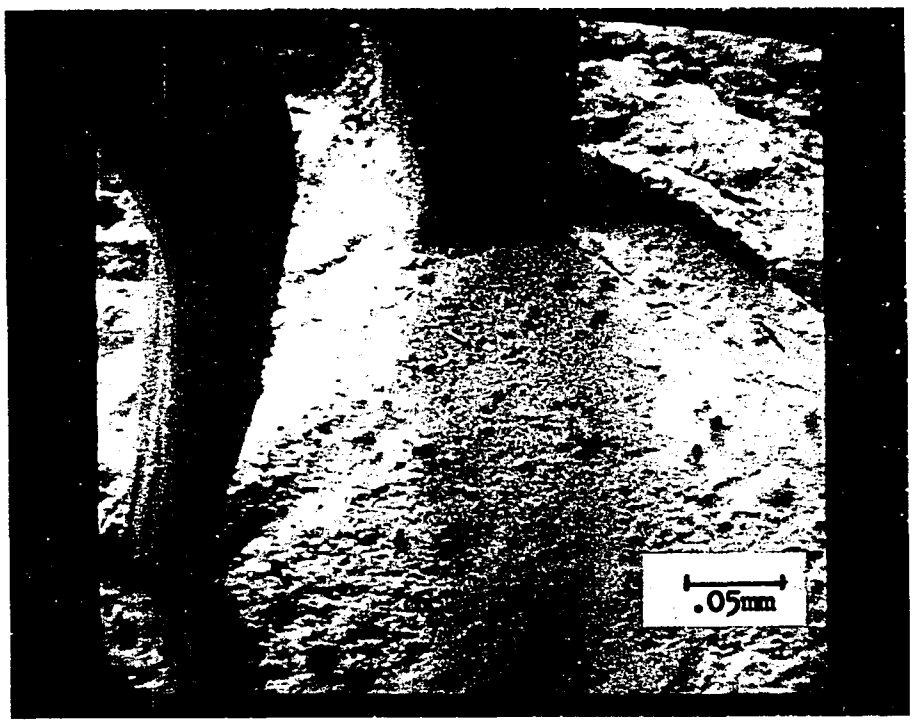

(a)

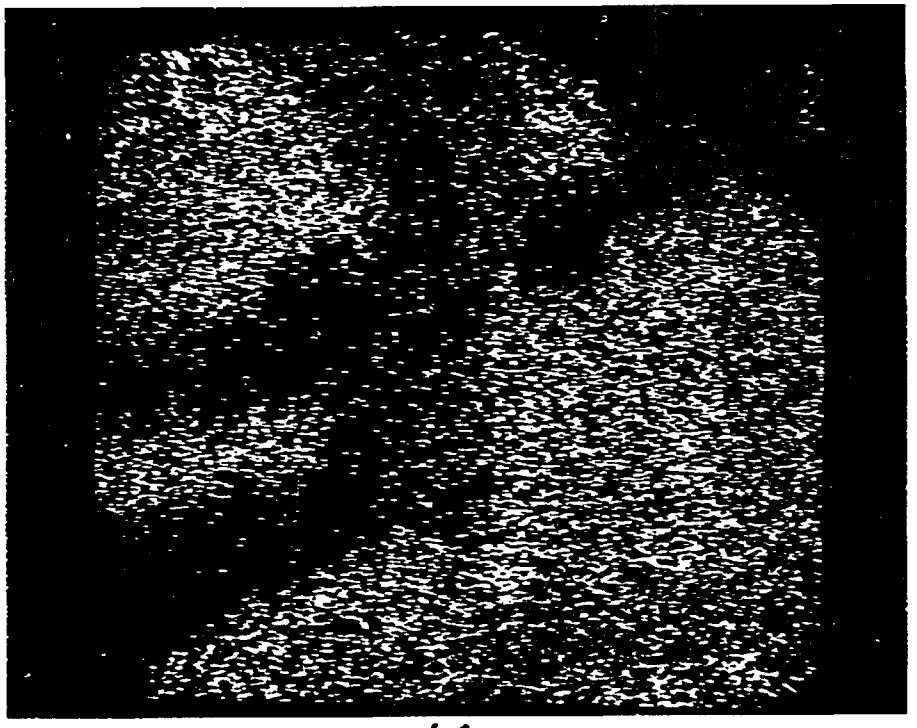

(b)

Figure 56.2 (a) Sample after switching to lower resistance state, 1.4×10^4 Ω (Mag. 250X). (b) Te distribution.

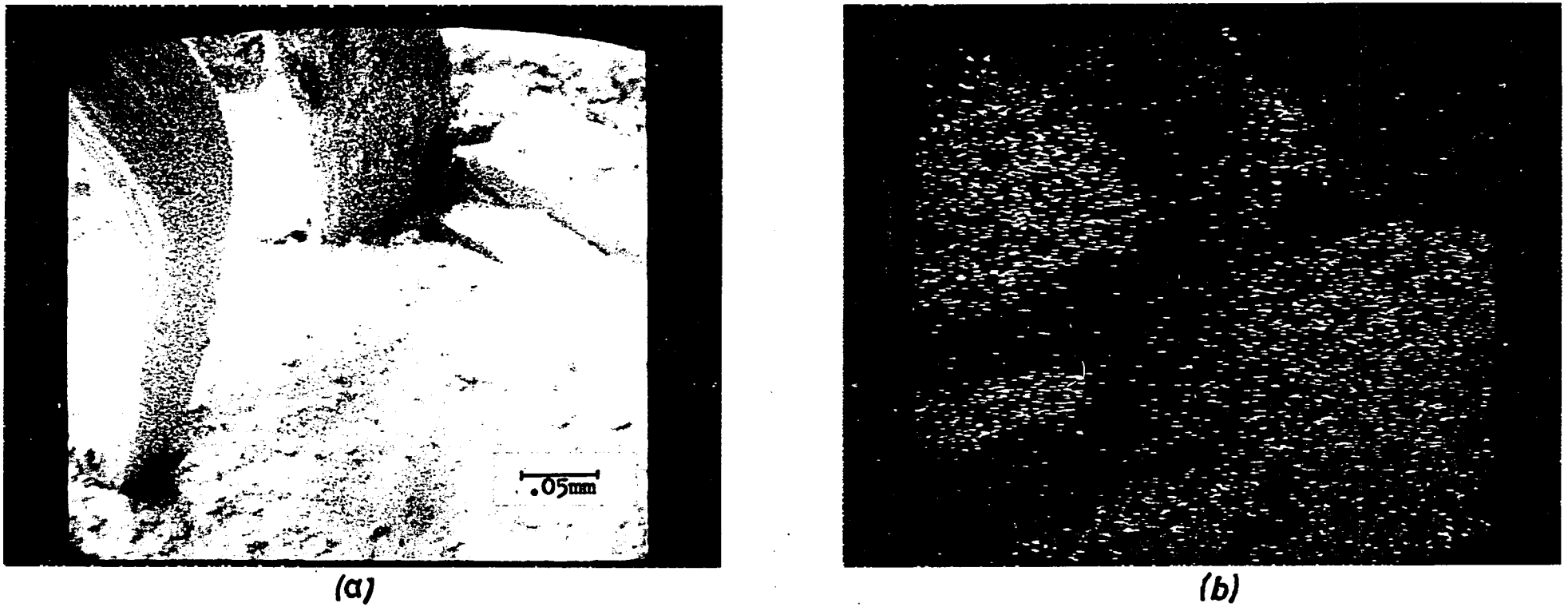

Figure 56.3 (a) Sample after being switched to slightly higher resistance state, 5 x 10^5 Ω, then back to 1.5 x 10^4 Ω (Mag. 250X). (b) Te distribution.

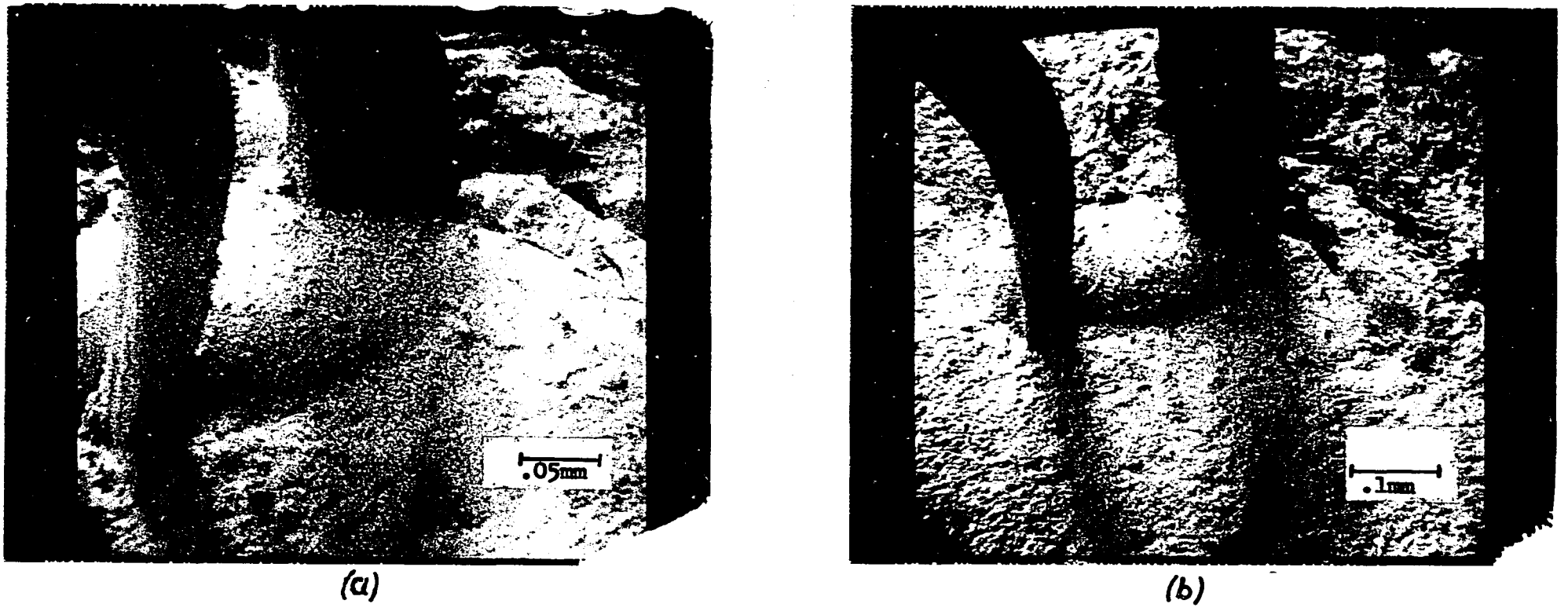

EMPA, At.%: Ge: 8.9 Se: 3.7 Te: 87.3

Figure 56.4. (a) Sample after higher current pulse lowers resistance to 3.6 x 10^3 Ω (Mag. 250X). (b) Same area, larger view (Mag. 140X). Note indentation between electrodes and widened crevices about upper electrode indicating extensive heating.

content (87 instead of 81 at. %) and a corresponding decrease in Ge (9 instead of 15 at. %).

Figure 57 represents a similar trial for a composition alleged to give threshold switching characteristics[69]. $Ge_{20}Se_{15}Te_{65}$ obviously behaves quite like a memory switch, although twice the voltage is required to effect its transition to the low resistance state as compared to that for $Ge_{15}Se_4Te_{81}$. (The load resistor R, for both samples in the initial switch was 10 kΩ).

Figures 58.1 - .3 again follow the transitions between the high resistance state and the low one. This time, a clearly visible filament appears between the electrodes after the switch to the lower resistance state [Fig. 58.2(a)]. EMPA results in the area of the electrodes and, at higher magnification , within the filament itself indicate a slight increase in the Te content, though so slight as to be within experimental error of the original composition. Unfortunately, the x-ray micrographs again do not show whether any ordering has occurred to form the conducting state.

After a high current pulse (200 V across a 100Ω resistor) the material near the positive electrode appears to have melted out from underneath it and quenched back to the glassy state [Fig. 58.3 (a)]. EMPA results at this point show a decrease in Te and increase in Ge back to their original atomic per cent concentrations.

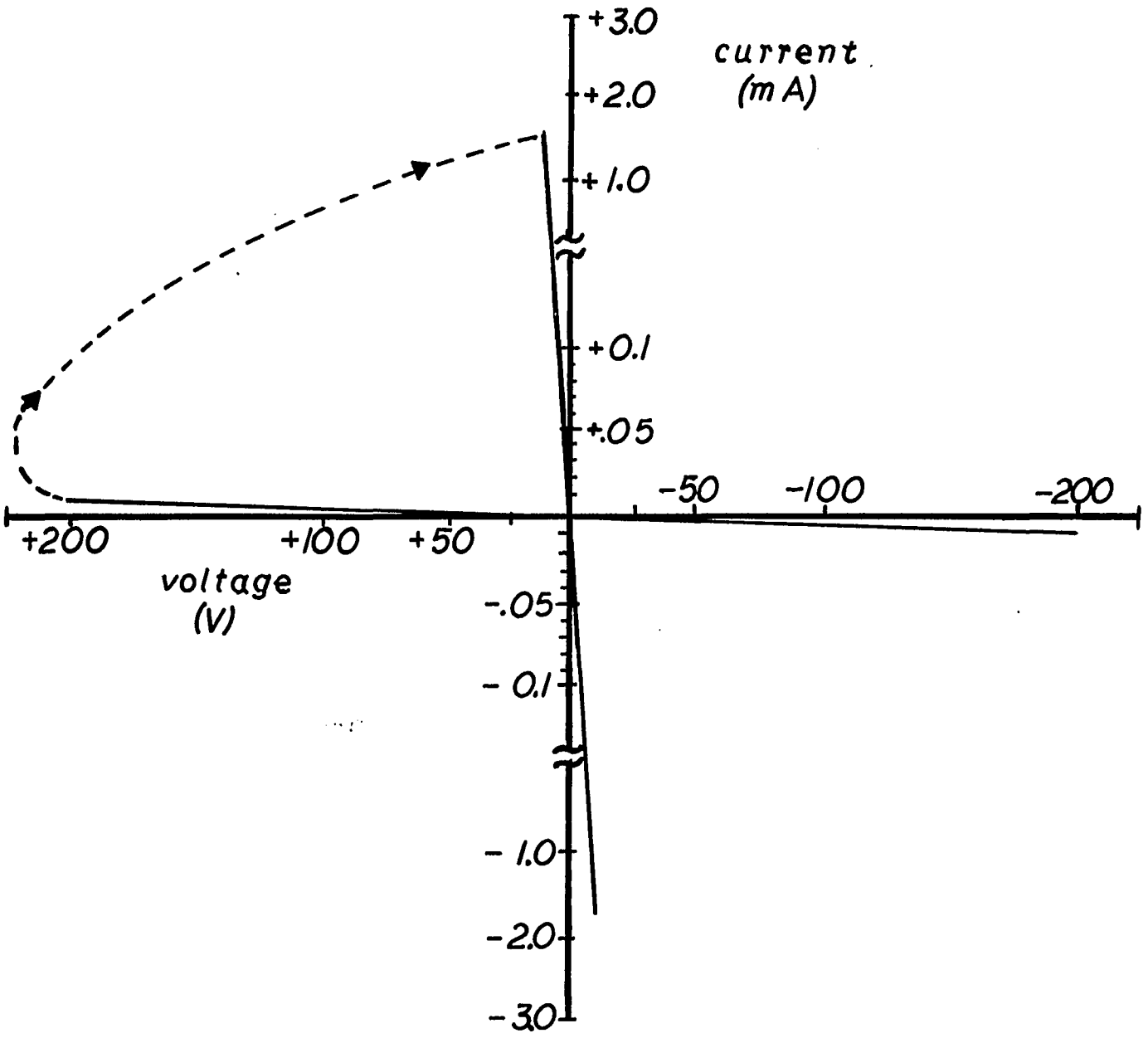

Figure 57. Current vs. voltage curve for a bulk sample of $Ge_{20}Se_{15}Te_{65}$ before and after switching along the dashed line.

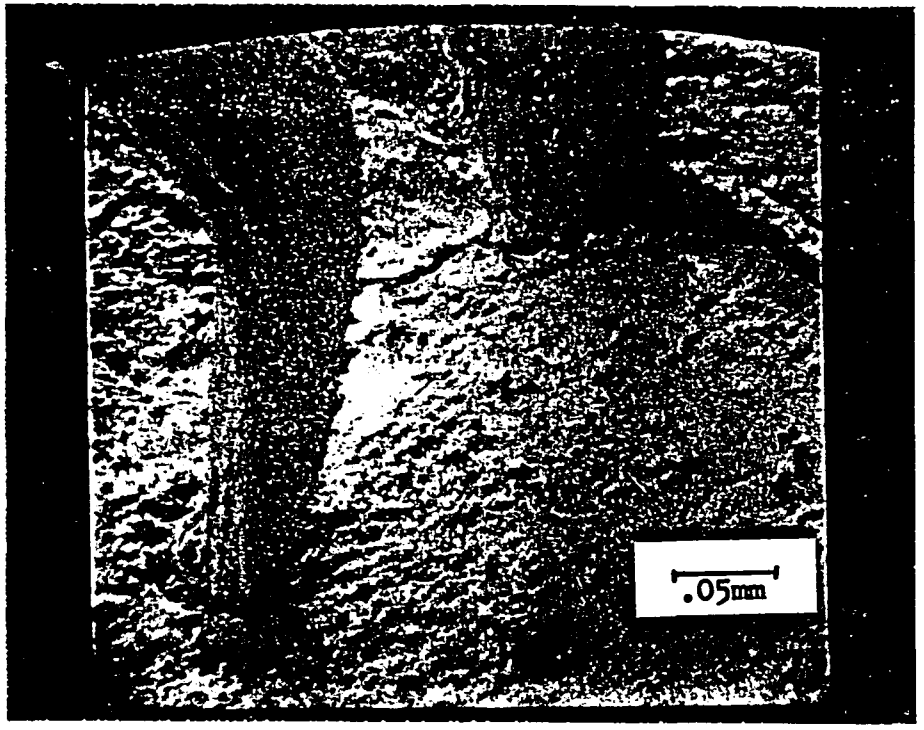

(a)

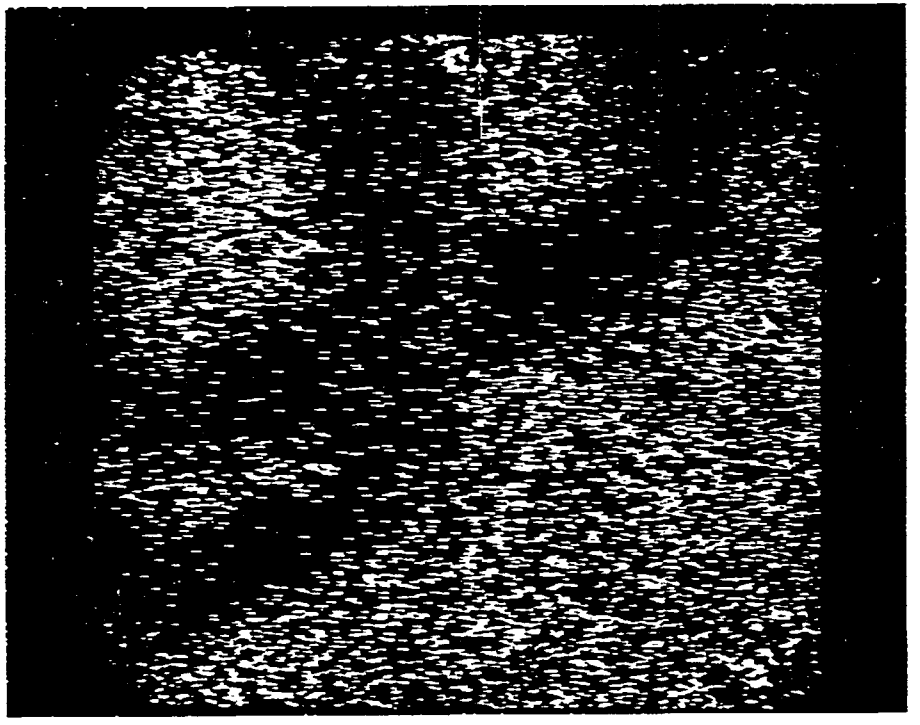

(b)

EMPA, At%: Ge: 20.2 Se: 14.7 Te: 65.1

Figure 58.1. (a) Electron micrograph of area near the electrodes (185μm. apart) for sample $Ge_{20}Se_{15}Te_{65}$ before switching (Mag. 250X). Sample resistance was 3×10^8 Ω. (b) X-ray micrograph of Te distribution.

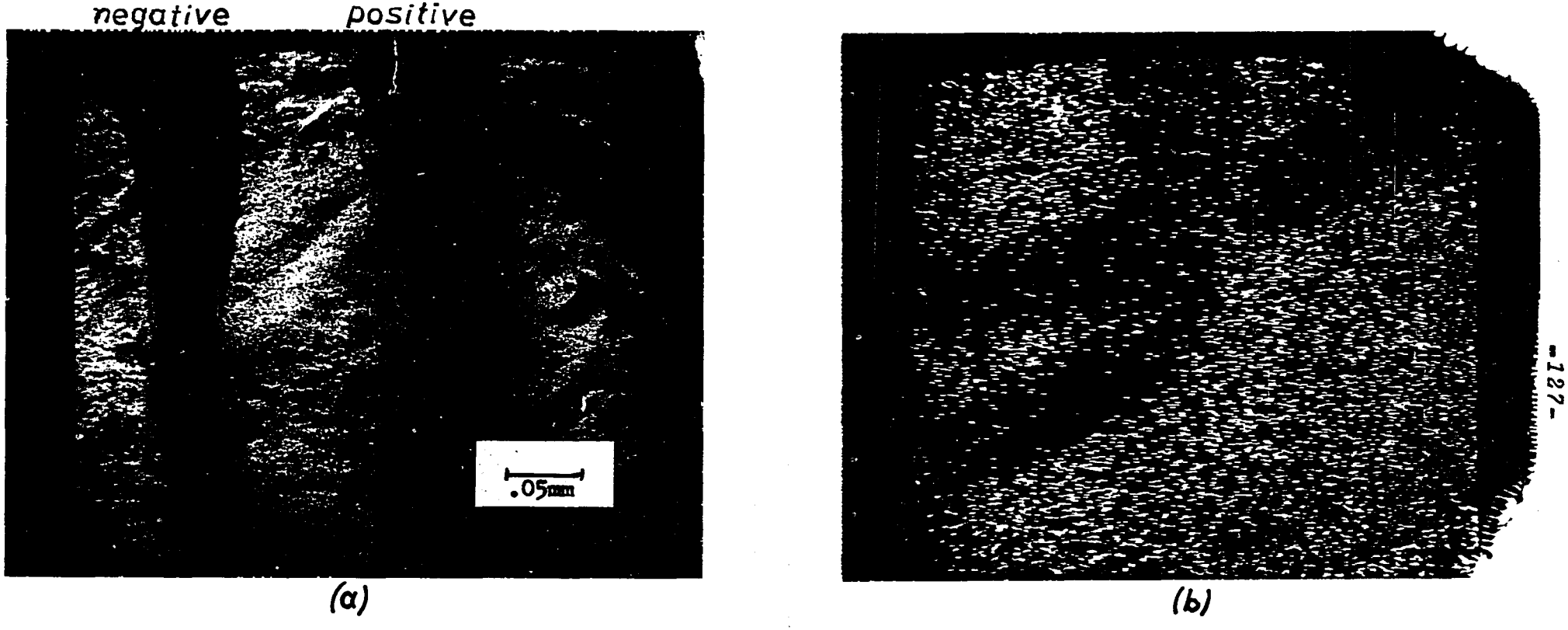

EMPA, At.%: Ge: 19.3 Se: 14.7 Te: 66.0 (at Mag. 250X)
Ge: 19.4 Se: 12.0 Te: 68.6 (at Mag. 2500X)-within filament

Figure 58.2. (a) Sample after switching to lower resistance state, 6×10^4 Ω (Mag. 250X). (b) Te distribution.

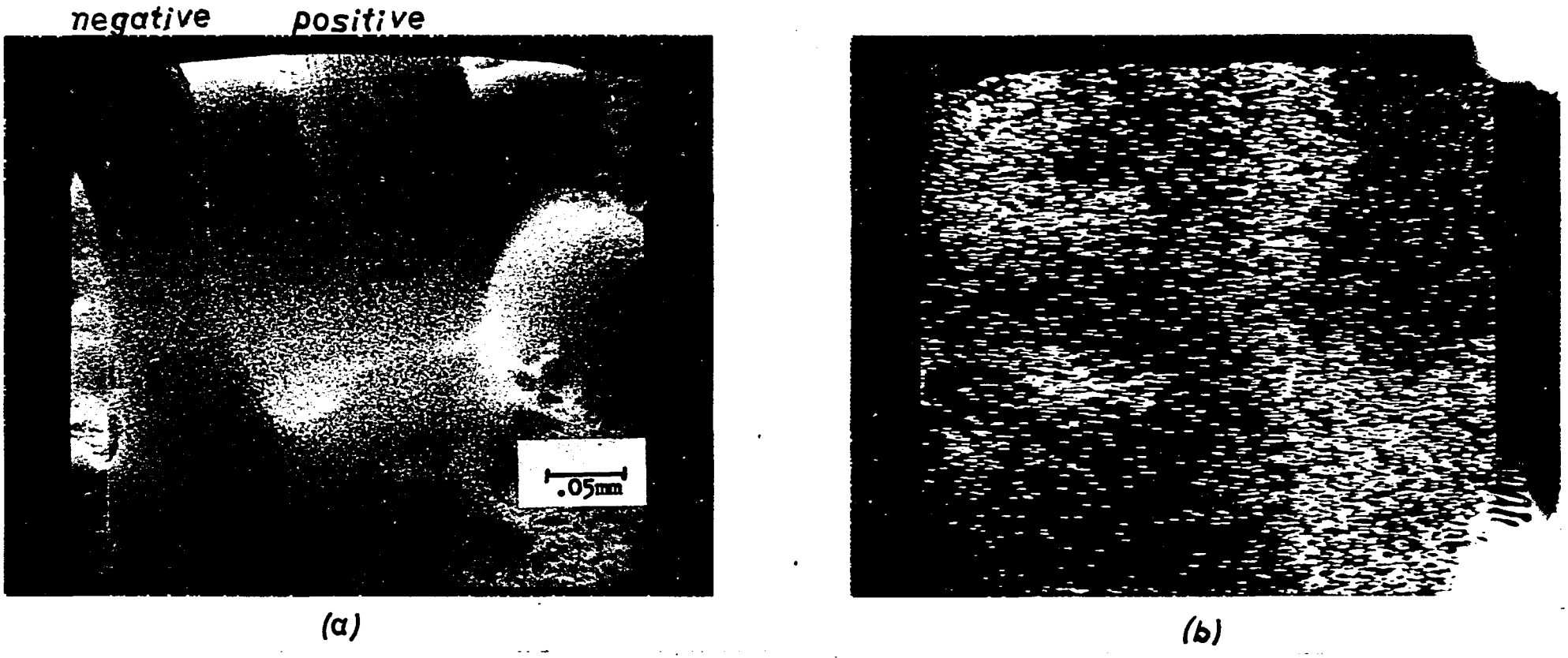

EMPA, At.%: Ge: 21.3 Se: 14.2 Te: 64.4 (at Mag. 250X)

Figure 58.3. (a) Sample after high current pulse caused extensive melting with quenching back to the amorphous state (Mag. 250X). Heating effect apparently greatest at the positive electrode. (b) Te distribution.

E. Differential Thermal Analysis

Powdered bulk samples (∿40 mg each) of various compositions yield the DTA traces given in Figures 59-64 and summarized in Table 8. Structural changes as a function of composition are self-evident from the different series of curves.

The softening temperature T_g increases with increasing Ge content as does the first exothermic cyrstallization peak T_{x_1} as seen in Figures 59 and 62. The eutectic melting point T_m does not change. No change in the Ge content, with only slight changes in Se and Te, results in little change in T_g and T_x as in Figure 60. Keeping Ge constant and moving across the phase diagram by increasing Se and decreasing Te sees a decreasingly distinct crystallization peak moving toward increasingly higher temperatures (Fig. 61). This is probably due to the decreasing Te, since in Figure 63 a sharp increase in Se content brings about early crystallization of Se in $Se_{70}Te_{30}$.

In the DTA curves where two exothermic peaks occur as in Figure 59, x-ray diffraction indicates that the first is due to the crystallization of Te, while the second corresponds to the formation of crystalline GeTe. For some compositions where only one peak occurs, as in $Ge_{20}Te_{80}$, $Ge_{20}Se_{10}Te_{70}$, $Ge_{25}Se_{10}Te_{65}$, and $Ge_{25}Se_{45}Te_{30}$, both Te and GeTe appear to have crystallized simultaneously. (This

situation for $Ge_{20}Te_{80}$ has also been noted by Savage[79].

The DTA results are in excellent agreement with earlier x-ray diffraction results obtained in mapping out the glass-forming region (Fig. 41). Again, the higher the Te content and lower the Ge content, the more readily does the amorphous phase undergo crystallization.

An interesting development occurs for glasses containing ∿4 at. % Se in that their DTA curves (Fig. 59) contain a pronounced endothermic peak followed closely by exothermic activity, T', all between the crystallization of GeTe, T_{x_2}, and the melting point of T_m. This is aparently unique in glasses containing Se, as other glasses with similar amounts of As, Sb, and Si do not exhibit this endotherm (Fig. 64).

A series of Te-rich glass compositions which have been mentioned in the literature by various groups in connection with switching experiments have DTA curves shown in Figure 64. $Ge_{15}Sb_2S_2Te_{81}$ exhibits memory switching, while $Ge_{10}Si_{12}As_{30}Te_{48}$, often referred to by the acronym STAG, serves as a threshold device (note the lack of any distinct crystallization peaks). Quaternary devices are preferred for commercial purposes over ternary ones with similar electronic characteristics since they last longer. Addition of only 2 at. % of a fourth constituent to a three-element glass improves memory device lifetime to the point where it can withstand 10^{12} switching operations, far more than the number that cause breakdown in the three-element device[80].

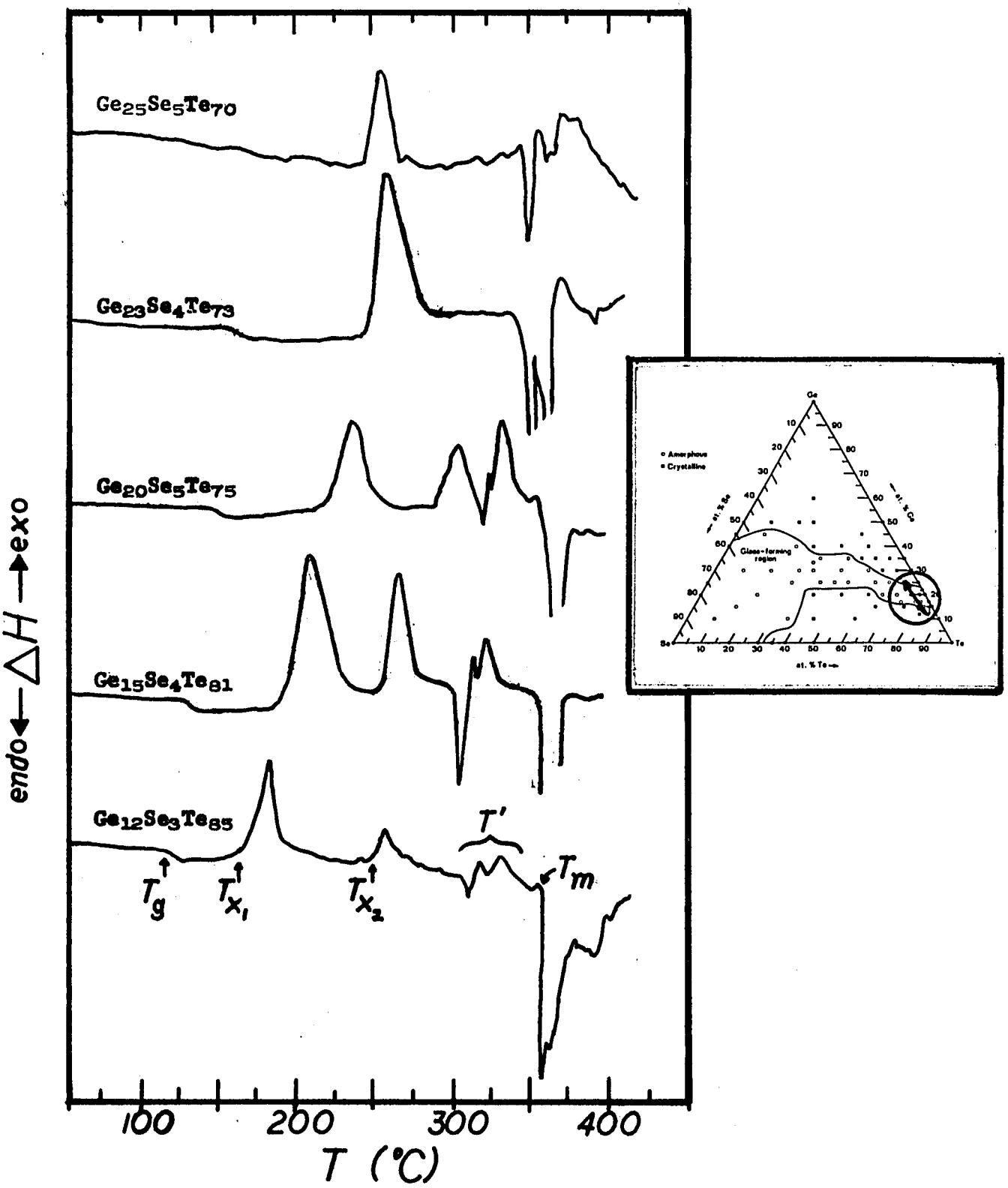

Figure 59. DTA curves for a series of Ge-Se-Te glasses with compositions along the encircled line of the inset. Heating rate: 20°C/min.

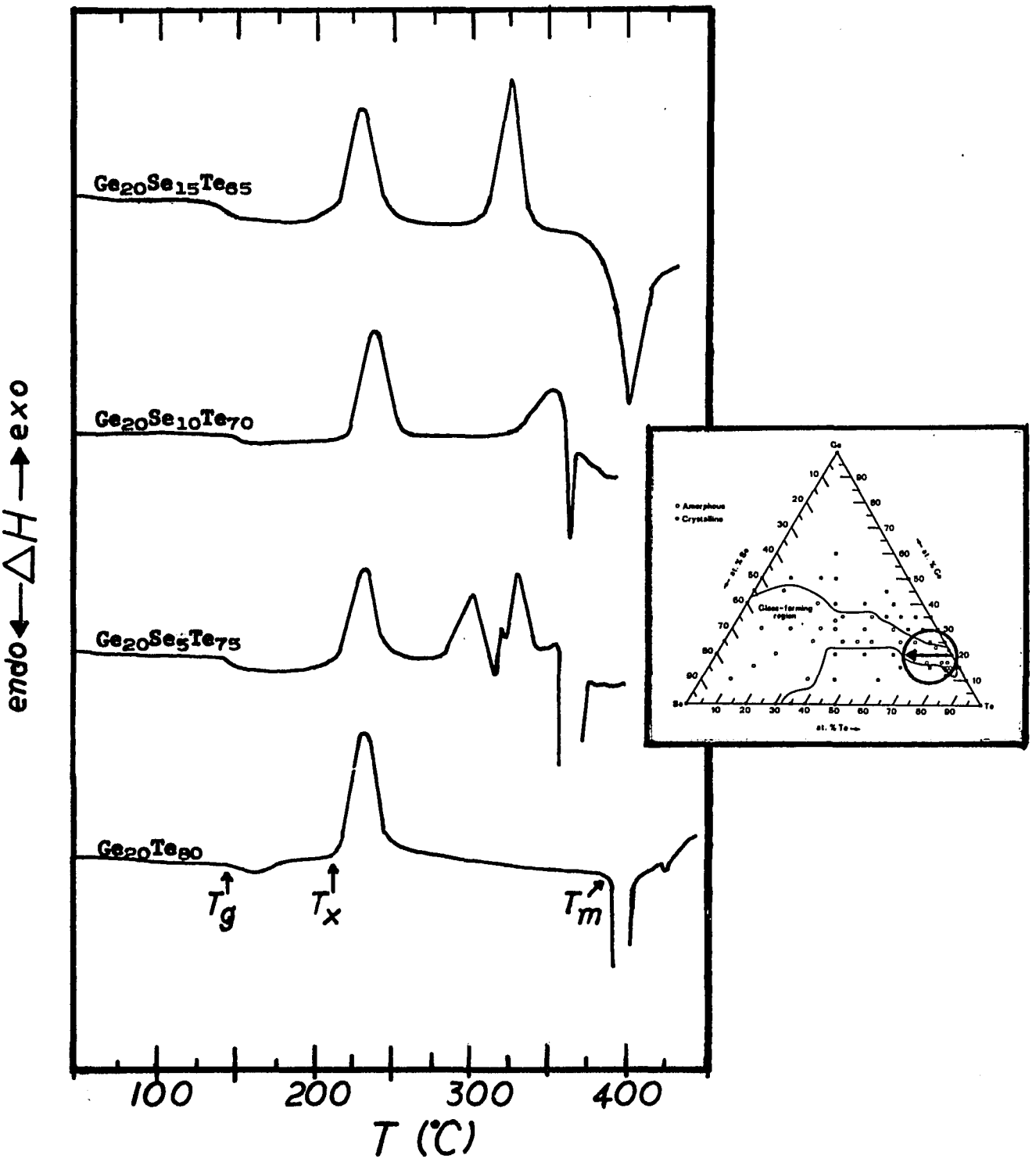

Figure 60. DTA curves for a series of Ge-Se-Te glasses with compositions along the encircled line of the inset. Heating rate: 20°C/min.

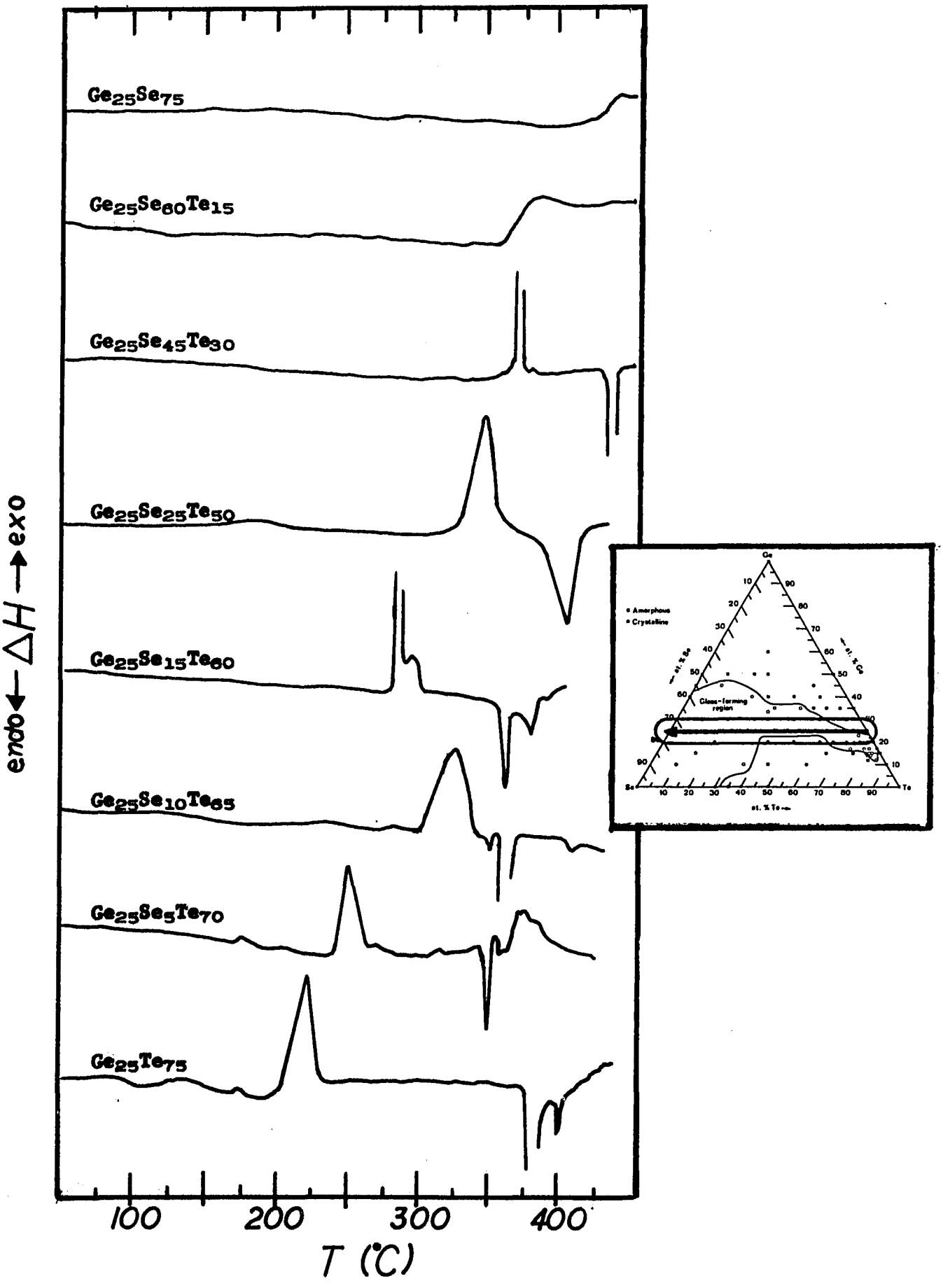

Figure 61. DTA curves for a series of Ge-Se-Te glasses with compositions along the encircled line of the inset. Heating rate: 20°C/min.

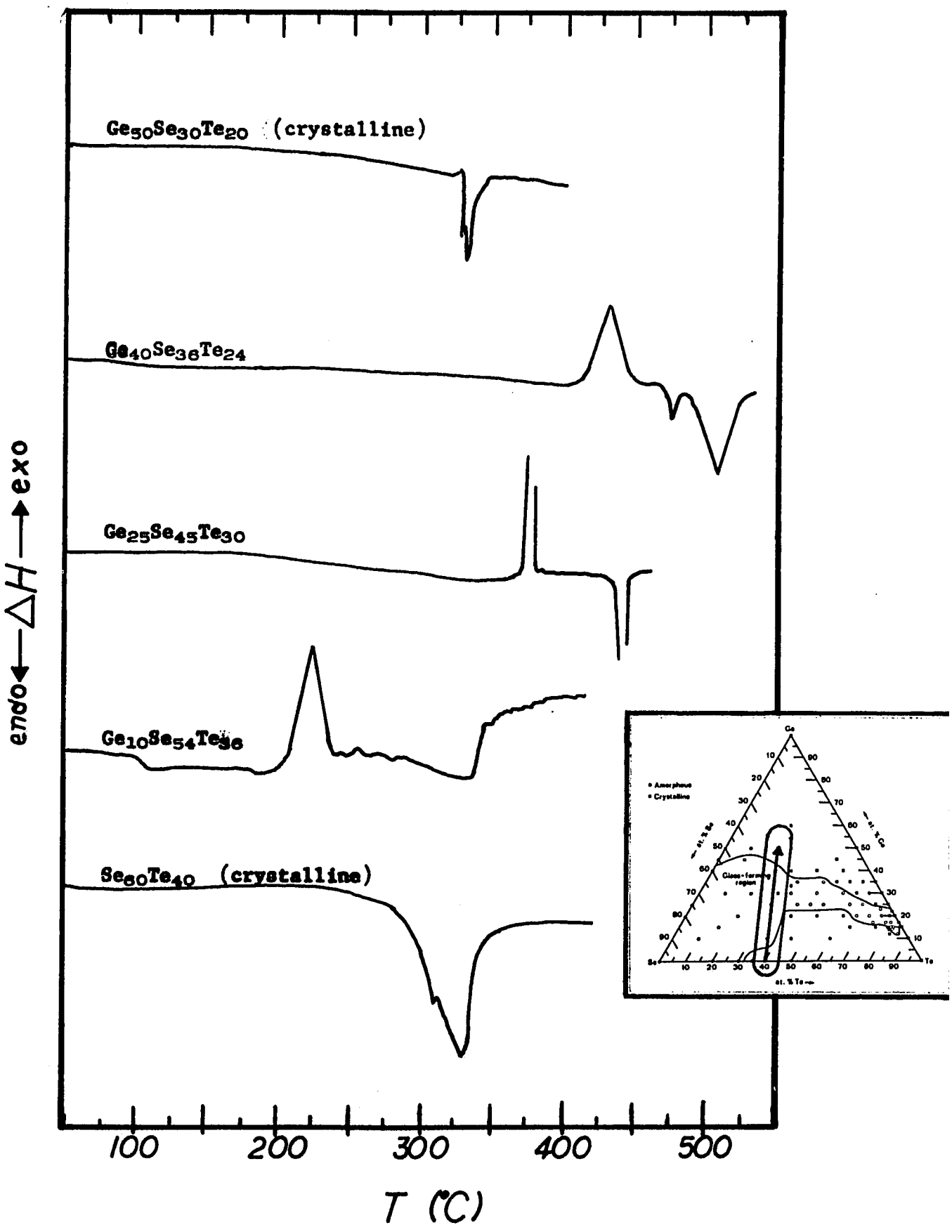

Figure 62. DTA curves for a series of Ge-Se-Te glasses with compositions along the encircled line of the inset. Heating rate: 20°C/min.

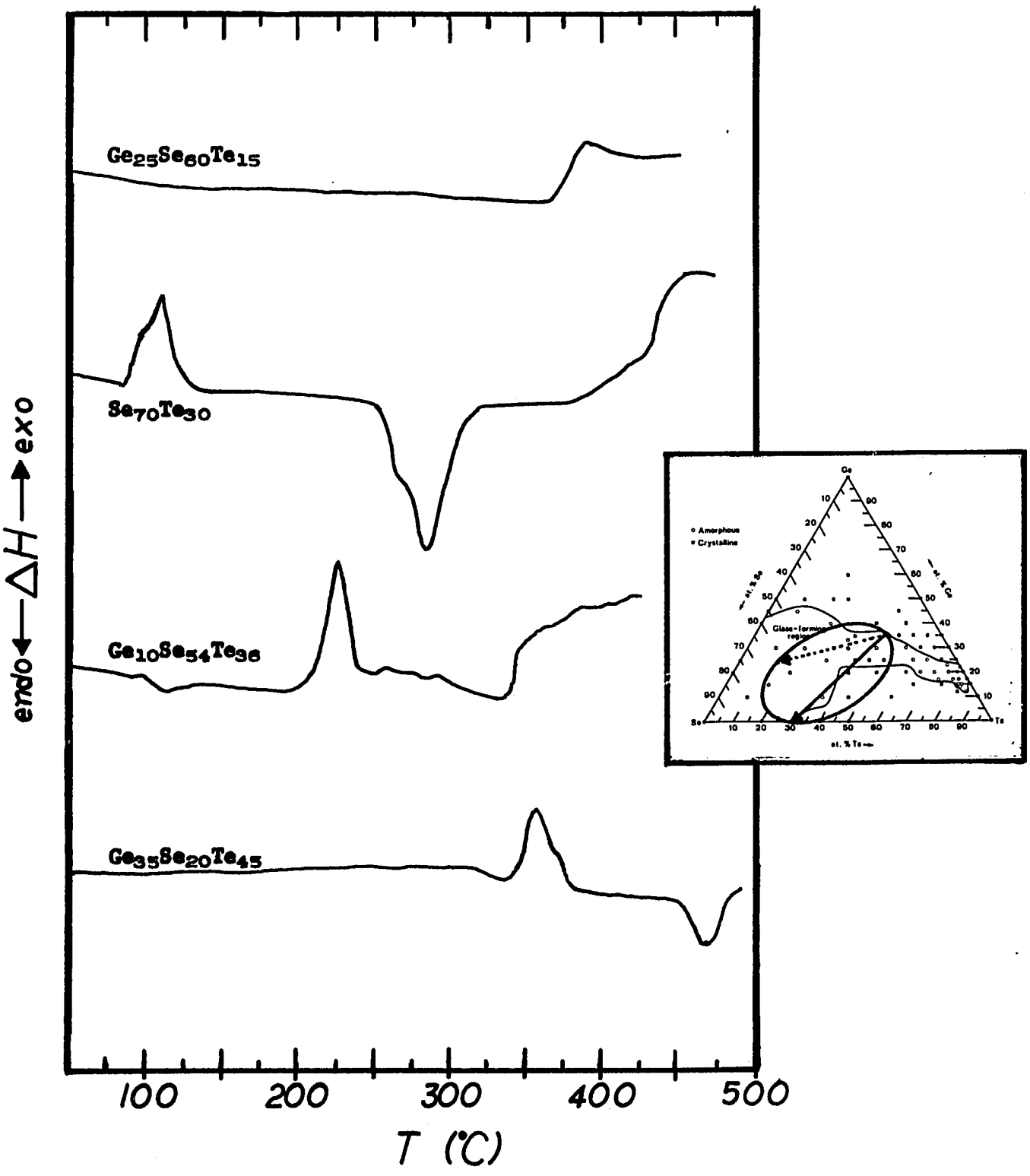

Figure 63. DTA curves for a series of Ge-Se-Te glasses with compositions along the encircled line of the inset. Heating rate: 20°C/min.

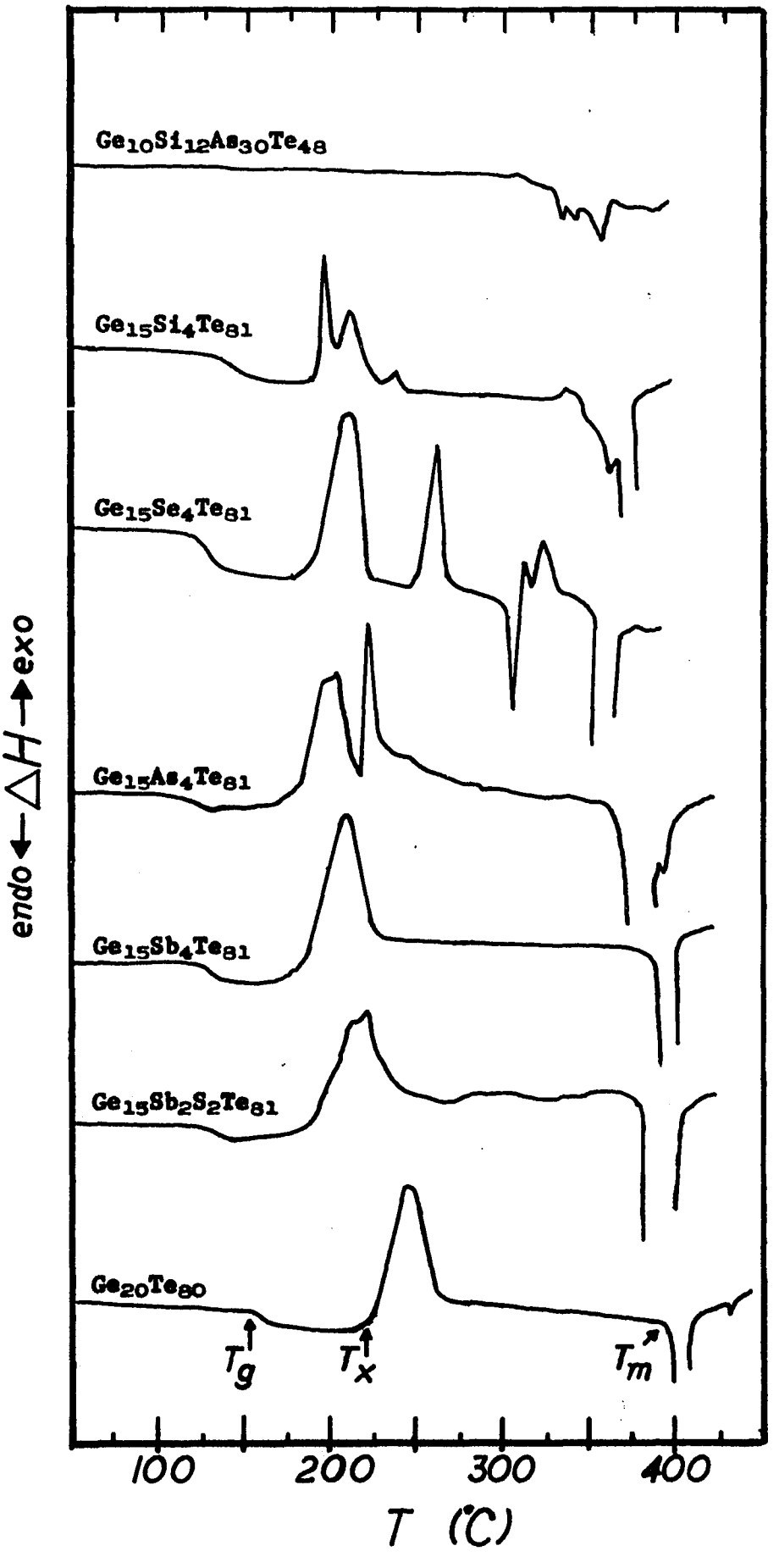

Figure 64. DTA curves for binary, ternary, and quaternary glasses rich in Te. Heating rate: 20°C/min.

At. % Ge	Se	Te	T_g	T_{x_1}	T_{x_2}	T'	T_m (°C)
12	3	85	123	165	245	297-313	348
15	4	81	128	189	253	306-321	355
20	5	75	140	208	277	301-315	349
23	4	73	168*	232	---	---	353
25	5	70	170*	245	---	---	352
20	0	80	150	220[1]	---	---	390
20	5	75	140	208	277	301-315	349
20	10	70	148	223	327	---	365
20	15	65	138	217	308	---	395

[1]Both crystalline Te and GeTe phases are present after annealing for 1 hr. at 250°C.

25	0	75	140*	208			373
25	5	70	170*	245			352
25	10	65	( )*	312[2]			360
25	15	60	( )*	273			345
25	25	50	197*	328			389
25	45	30	268*	362			424
25	60	15	---	354			---
25	75	0	---	390			---

[2]Both crystalline Te and GeTe phases were present after slow cooling from the melt and also after annealing for 1 hr. at 350°C.

*poorly defined point.

Table 8. Softening, crystallization, and melting point temperatures for amorphous Ge-Se-Te compositions as determined by differential thermal analysis. (from Figs. 59-61).

At. % Ge	Se	Te	T_g	T_{x_1}	T_{x_2}	T'	T_m (°C)
0	60	40 (cryst.)	---	---	---		283
10	54	36	102	198	325		---
25	45	30	268*	---	362		424
40	36	24	( )*	---	410		487
50	30	20 (cryst.)	---	---	---		320
35	20	45	( )*	---	335		442
10	54	36	102	198	325		---
0	70	30	82*	93	---		270
25	60	15	---	---	354		---
$Ge_{15}Sb_2S_2Te_{81}$			127	188	---	---	375
$Ge_{15}Sb_4Te_{81}$			126	184	---	---	387
$Ge_{15}As_4Te_{81}$			123	182	218	---	366
$Ge_{15}Se_4Te_{81}$			128	189	253	306-321	355
$Ge_{15}Si_4Te_{81}$			147	198, 208,	235	---	340,356,368
$Ge_{10}Si_{12}As_{30}Te_{48}$			---	---	---	---	336,350,362

*poorly defined point.

Table 8, cont'd. (from Figs 62-64).

F. Annealing

In order to determine how structural changes affect electrical conductivity and switching and to determine whether these changes manifest themselves on visual observation, EMPA, or x-ray mapping, an annealing experiment was performed. Samples of amorphous $Ge_{15}Se_{4}Te_{81}$ were annealed for one hour in vacuum-sealed quartz ampoules, each at a temperature determined by DTA to be an onset of crystallization. The samples were then sliced to ∿1 cm. long cylindrical sections (0.3 cm. diameter) and their conductivities measured. Part of each sample was powdered and submitted for x-ray diffraction, while larger granules were subjected to SEM observation, EMPA,and x-ray mapping.

Figure 65.1 shows the unannealed amorphous sample. Note the pockmarks on the otherwise smooth surface under higher magnification, probably due to rapid cooling from the melt. The pockmarks are gone, but the surface is no longer smooth in Figures 65.2 - .3,as sharply defined features appear after crystallization of Te and GeTe. Figures 65.4 and 65.5 represent samples annealed at temperatures beyond the first endothermic peak after which recrystallization has occurred. Note the reappearance of pockmarks in Figures 65.4 and 65.5(a) along with the distinct crystalline features. This may indicate cooling from a second melt that occurred at

the first endothermic peak. A melt occurring after the first crystallizations and cooling to give more crystallization may be the reason why $Ge_{15}Se_4Te_{81}$ switches readily to the low resistance state but not as readily back to the disordered state. The second melt allows crystallization to proceed beyond a narrow filament between the electrodes and the larger crystalline area formed is too large to be quenched by the surrounding non-crystalline environment.

EMPA and x-ray mapping are not useful on these non-flat surfaces as x-ray intensities are affected to a greater degree by surface variations than by slight composition changes. For example, the bright curved area in the secondary electron micrograph of Figure 65.5(a) appears as the bright curved area in the Te x-ray and Ge x-ray micrographs (b) and (c). EMPA results consequently do not accurately reflect changes in composition as a result of structural change.

Figure 66 gives the x-ray diffraction peaks for the annealed samples, while Table 9 summarizes the annealing results. It seems that, while crystallization of Te increases the conductivity substantially and crystallization of GeTe enhances it somewhat more, further crystallization beyond the endothermic peak does not affect the conductivity directly. However, in an extremely short heating interval as in switching, the molten state preceding recrystallization probably allows for more extensive ordering to take place than could otherwise occur in the softened but not molten state.

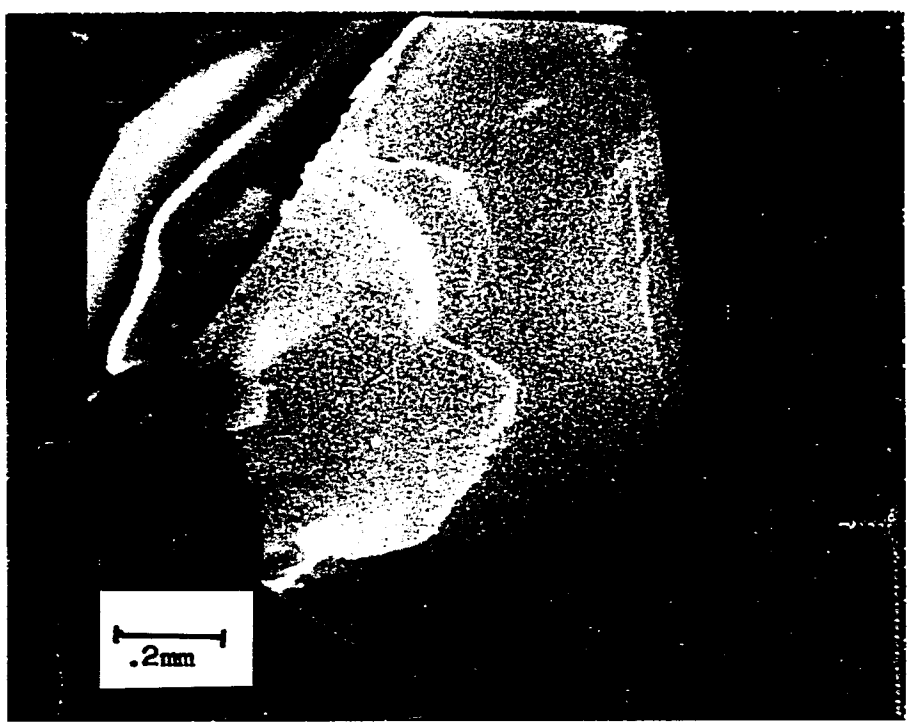

(a)

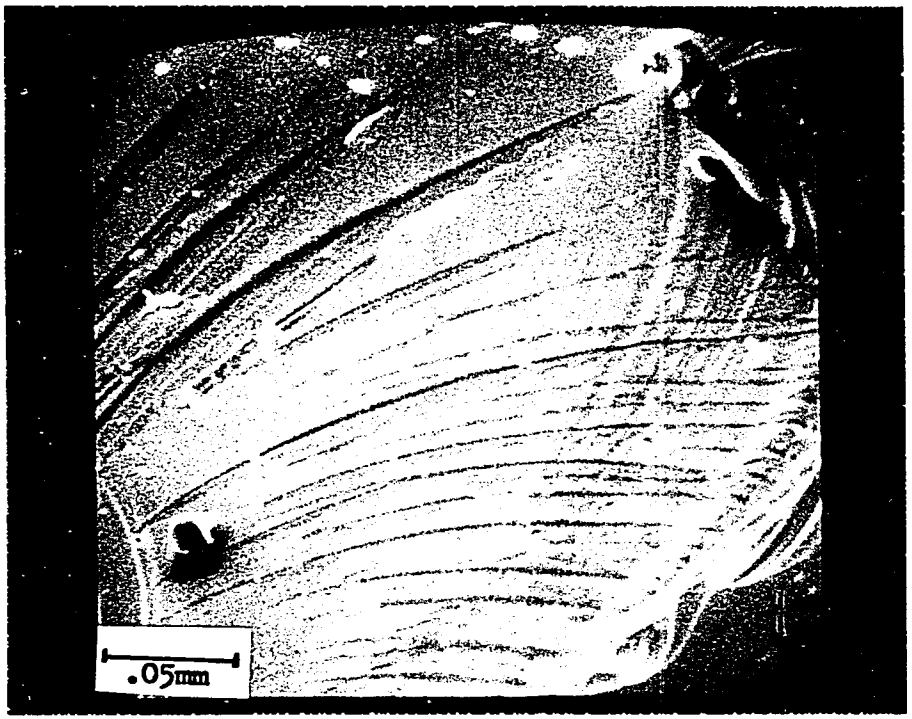

(b)

Figure 65.1. Electron micrograph of amorphous $Ge_{15}Se_4Te_{81}$, SAMPLE A, unannealed (a) at Mag. 70X and (b) at Mag. 350X.

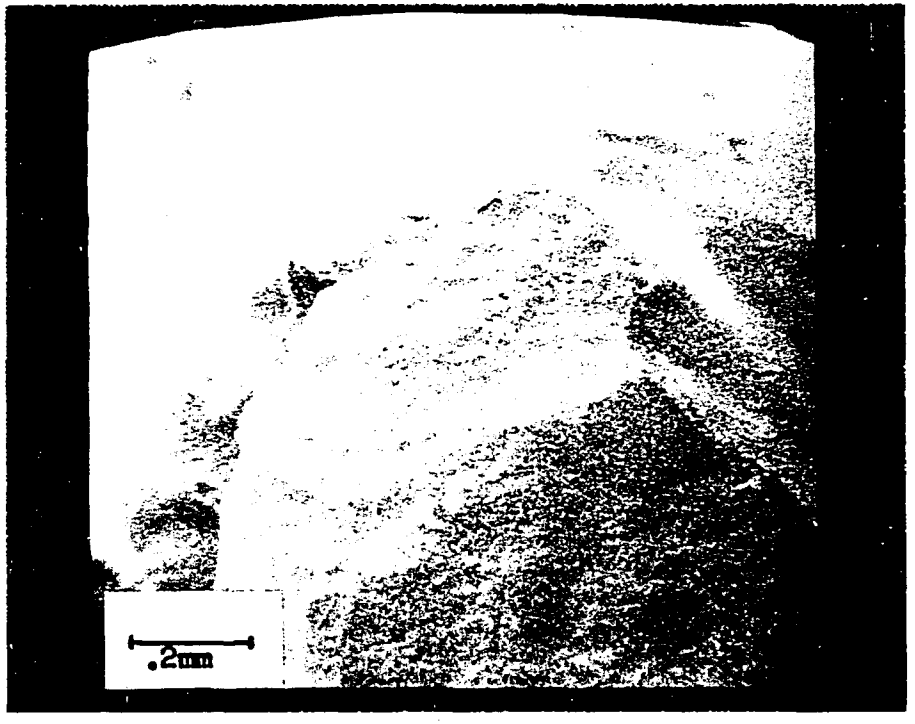

(a)

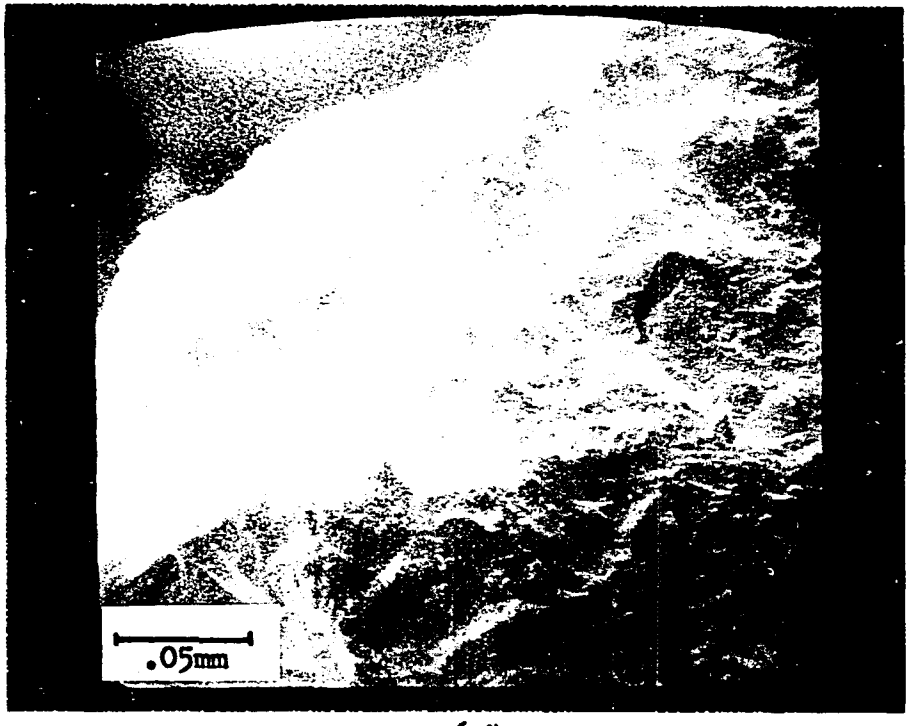

(b)

Figure 65.2. SAMPLE B, annealed for 1 hr. at 220°C in vacuum. Seen at (a) Mag. 80X with (b) close-up view of upper left edge at Mag. 350X.

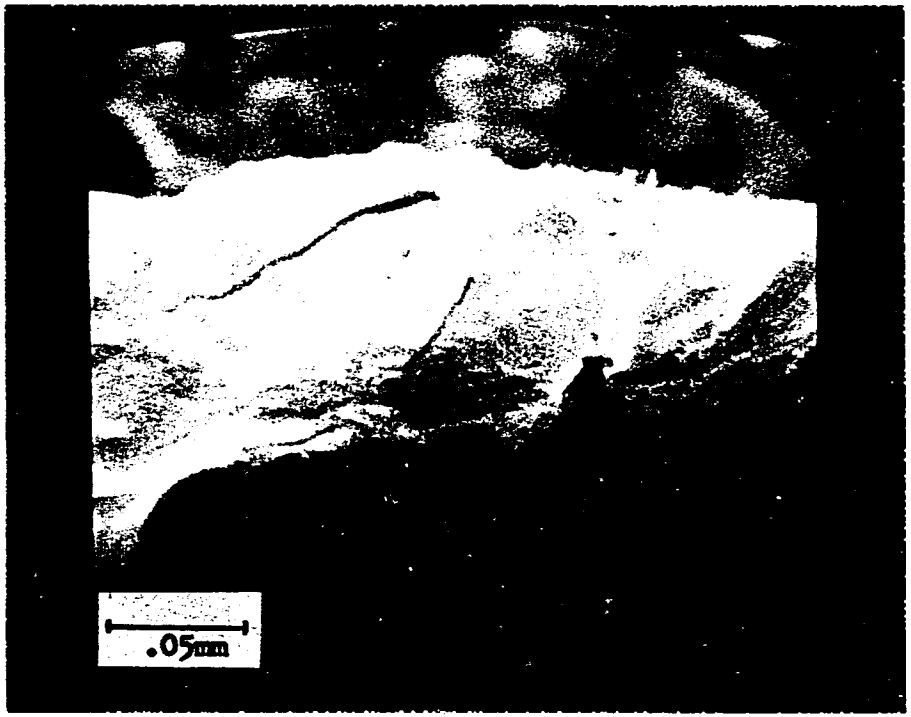

Figure 65.3. SAMPLE C, annealed for 1 hr. at 285°C in vacuum. Seen at Mag. 350X.

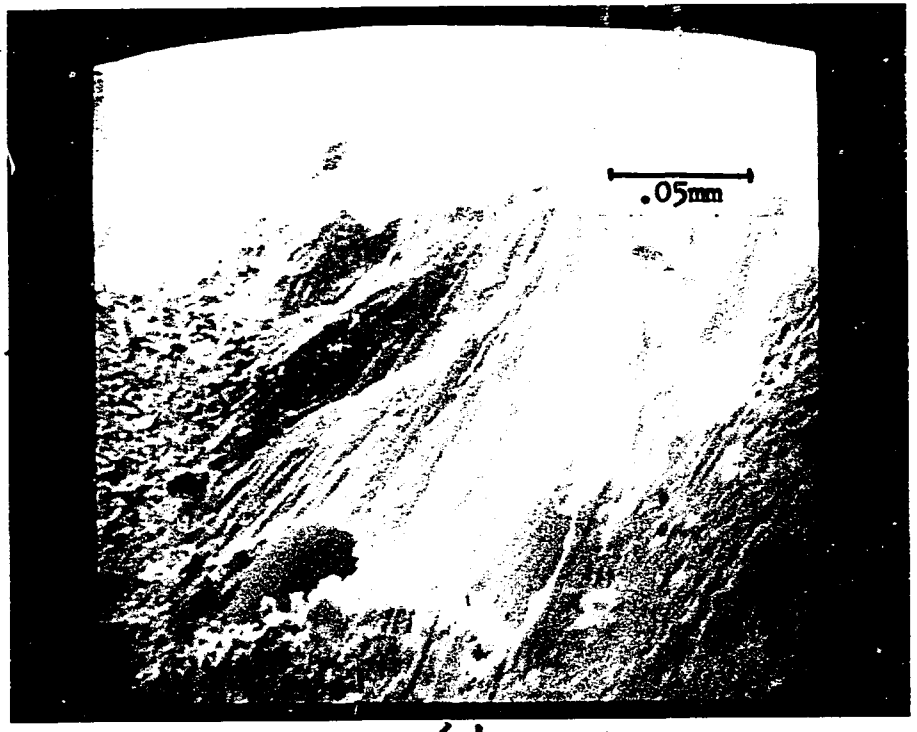

(a)

(b)

Figure 65.4. SAMPLE D, annealed for 1 hr. at 316°C in vacuum. Seen at (a) Mag. 350X and (b) at a different point,also at Mag. 350X.

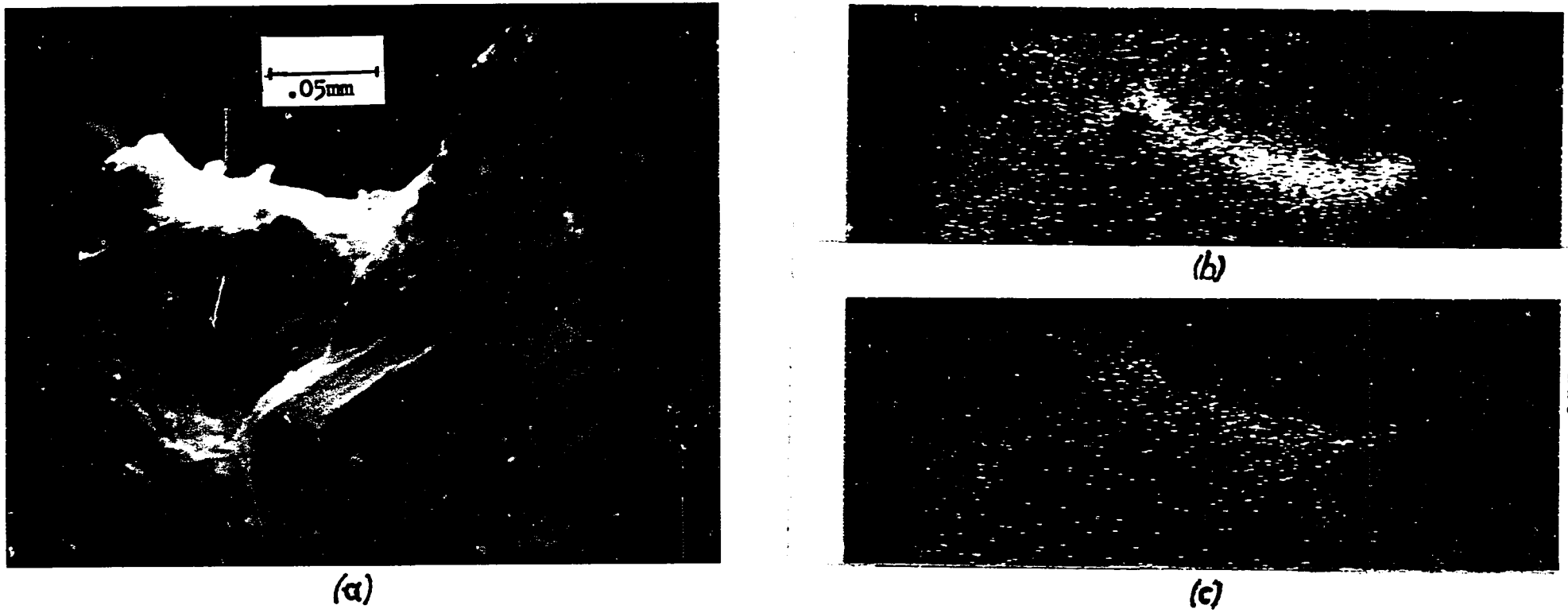

Figure 65.5. SAMPLE E, annealed for 1 hr. at 335°C in vacuum. (a) Electron micrograph at Mag. 350X. (b) X-ray micrograph of Te distribution (6 min. exposure). (c) X-ray micrograph of Ge distribution (12 min. exposure).

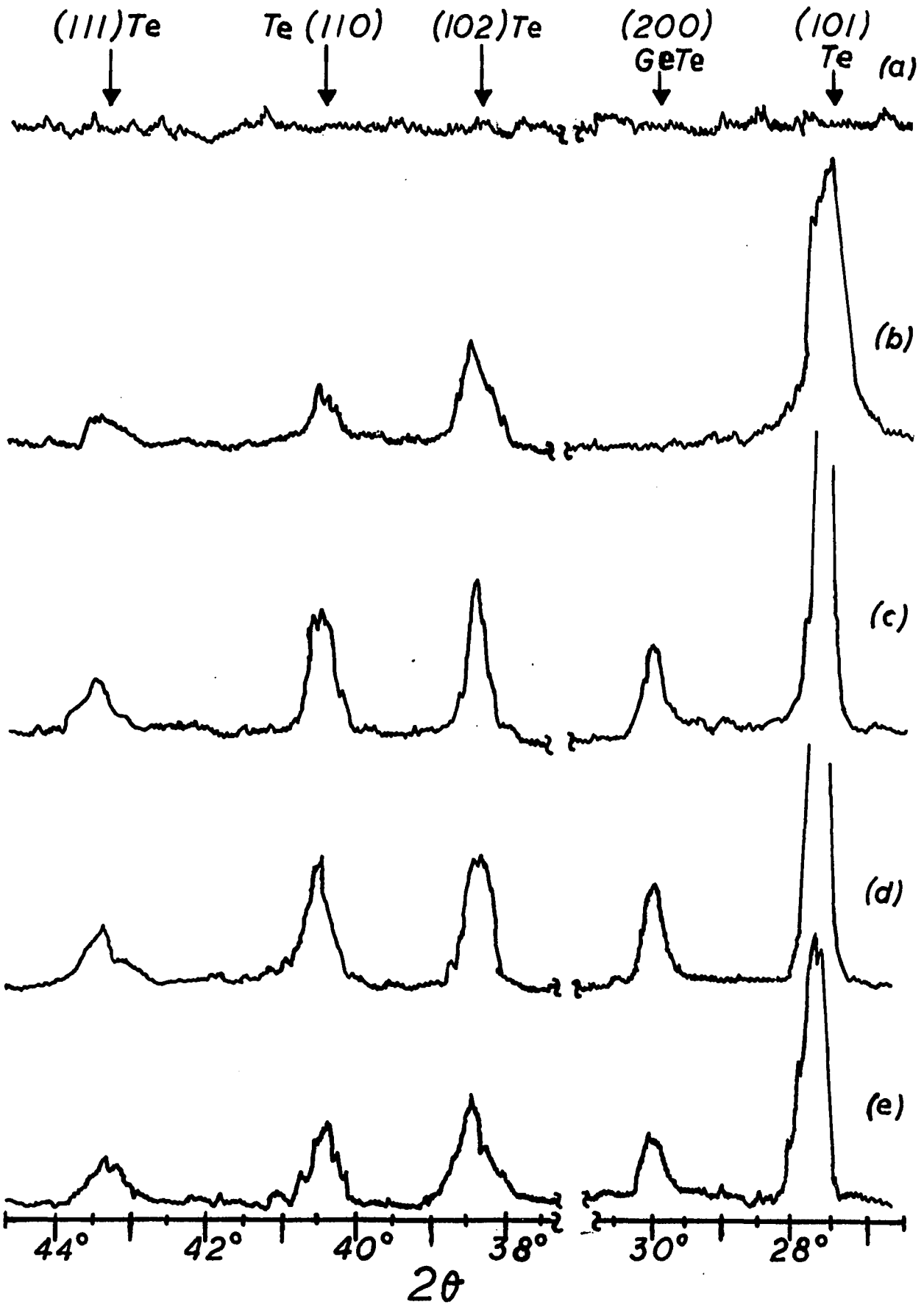

Figure 66. X-ray diffraction peaks for powdered samples of $Ge_{15}Se_4Te_{81}$ (a) unannealed, (b) annealed at 220°C, (c) at 285°C, (d) at 316°C, and (e) at 335°C, each for 1 hr. in vacuum. (Miller indices in parentheses).

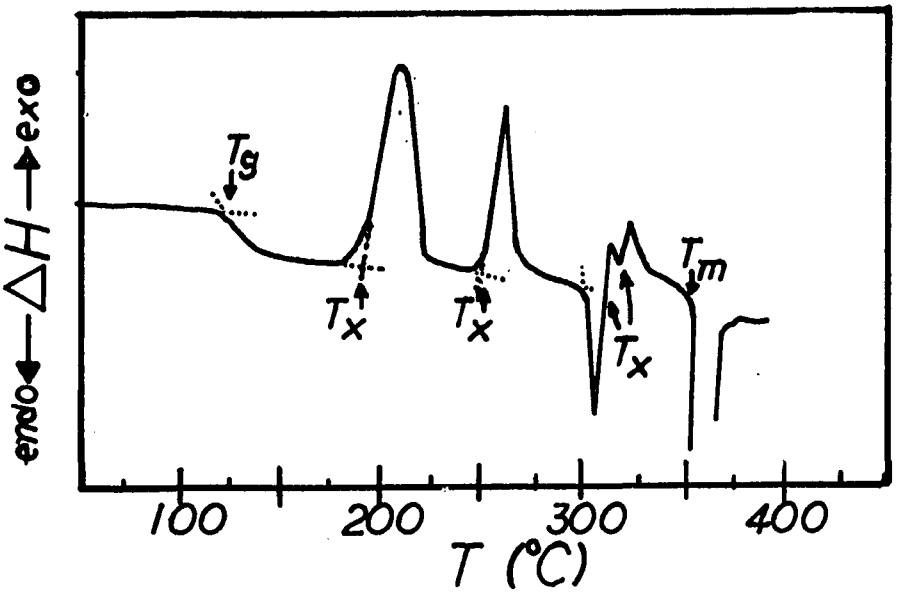

Sample	Crystallization Temperature (°C)	Annealing Temperature (°C)	$\sigma_{r.t.}$ (ohm^{-1}-cm^{-1})	X-ray Peaks
A	---	---	7.0×10^{-5}	none
B	189	220	3.6×10^{-1}	Te
C	253	285	5.8	Te, GeTe
D	312	316	9.5	Te, GeTe
E	321	335	8.3	Te, GeTe

Table 9. Summary of results obtained for samples of $Ge_{15}Se_4Te_{81}$ annealed for 1 hr. in vacuum at temperatures indicated by DTA curve (above) to be onsets of crystallization.

VI. DISCUSSION

The glass-forming region in the Ge-Se-Te system appears to be larger than is generally the case for ternary compositions[25,26,28]. Also, it extends to all three sides of the phase diagram, forming glasses at some compositions for any of the three binary combinations; this too is rare.

From the phase diagram it is evident that tellurium content plays a major role in glass formation—the more tellurium the less likely that a molten mixture will remain in the amorphous state upon cooling, even at rapid quenching rates. Conversely, upon heating, DTA results indicate that the greater the Te content, the more readily will a glass composition undergo crystallization. Some workers have suggested that binary quenched glasses rich in Te are actually polycrystalline[78], though no actual phase separation could be found in films of $Ge_{15}Te_{85}$[82].

Tellurium also nucleates readily at the sample surface and crystallizes to give the higher conduction found on annealing at temperatures below those at which bulk crystallization occurs[77,83]. Despite the ease with which Te-rich glasses crystallize, quenching the molten samples in an ice bath was found to be sufficient to produce the amorphous state in small 1 gram samples. Larger samples ∿25 grams apparently require more rapid quenching in liquid nitrogen[79]

When devitrification does occur, the first crystal-

line phase to appear is that of Te, followed by GeTe. Annealing $Ge_{15}Se_4Te_{81}$ for one hour at temperatures where crystallization occurs indicated that formation of the GeTe crystalline phase further increases the sample conductivity beyond the value obtained on formation of the crystalline Te phase. This agrees with results for bulk samples of binary $Ge_{17}Te_{83}$, ternary $Ge_{15}As_5Te_{80}$, and quaternary $Ge_{15}Te_{81}Sb_2S_2$ and thin films of $Ge_{15}Te_{85}$[83]. Investigation of the bulk samples after 27 hours of annealing at a temperature slightly below the onset of Te crystallization revealed the formation of a semiconducting surface layer of crystalline Te having a higher conductivity and an activation energy of 0.02 eV. Further annealing at a higher temperature produced the crystalline GeTe phase resulting in still higher, but metallic conductivity. Similarly, electron diffraction and TEM studies on the binary thin films suggested that the initial high resistance amorphous state of the glass gives way to lower resistance Te crystallites forming in the amorphous matrix, followed by a still lower resistance state created by Te crystallites in a GeTe crystalline matrix[84].

The endothermic DTA peak followed by exothermic recrystallization peaks unique for ternary Te-rich glasses containing ∿4 at. % Se does not appear to enhance the conductivity directly after an hour of annealing. But, as mentioned earlier, it may enable a larger area to undergo crystallization than would otherwise devitrify in the short

space of a switching event.

Electrical conductivity measurements on the bulk glass samples as a function of temperature yielded the familiar exponential relation [Eq.(26)] characteristic of semiconductors. Thermoelectric power measurements indicated holes as the majority carriers in all compositions.

Increasing Te content resulted in increasing conductivity and increasing glass density, with little change in activation energy (Table 3). Similar increases in conductivity and density with increased Te content were noted for the As-Te-Se system, though with decreasing activation energy[81]. Increasing Te content also produced higher conductivities for As-Te-I glasses[38].

Increasing Ge content seemed to decrease the activation energy in glasses measured "as prepared", i.e. those that were not reheated after quenching. However, compositions of $Ge_x(Se_{.6}Te_{.4})_{100-x}$ (Fig. 45, insert) approached activation energies between 0.6 - 0.7 eV after first being heated 125 - 150°C above room temperature. These new activation energies agree well with the range arrived at by Sakai, *et al* for similar compositions[50]. These low temperature annealing effects have also been observed in $As_2(Se,Te)_3$ glass systems[81]. All these materials have in common a substantial selenium content. Increasing activation energy may be due to structural change within the glass involving the easily

broken Se-Se bonds (49 kcal·mole^{-1}; melting point 217°C) and leading to stronger[78] heteropolar Ge-Se bonds that allow a more disordered system to exist than is first created on quenching.

Activation energies for binary ($Ge_{17}Te_{83}$), ternary ($Ge_{15}As_5Te_{80}$), and quaternary ($Ge_{15}Sb_2S_2Te_{81}$) glasses near the composition of $Ge_{15}Te_{85}$ have been reported to be about 0.43 - 0.48 eV and their densities were about 5.5 g/cm^3. DSC determined values for T_g, T_x, and T_m for $Ge_{17}Te_{83}$ were 133°C, 225°C, and 380°C respectively[83]. In my study, a composition of $Ge_{20}Te_{80}$, had an activation energy of 0.45 eV, a density of 5.4 g/ml and DTA determined values of T_g, T_x and T_m, of 150°C, 220°C, and 390°C. Similar values were obtained for the binary glass activation energy by Tsu , *et al*,[86] and for DTA peaks by Savage[87].

A.C. conductivity measurements as a function of temperature at a number of frequencies yielded values identical to the d.c. values indicating that electrical conduction at those temperatures proceeded by an "intrinsic" mechanism as in Equations (35) and (31) rather than by a hopping mechanism which would have had some frequency dependence. Coupled with the fact that TEP values were always positive, the activation energies measured corresponded to hole creation in the extended states of the valence band given by $\varepsilon_f - \varepsilon_v$ (Fig. 16). Low temperature a.c. conductivity measurements would be more likely to detect contributions from a hopping

mechanism; however, poor instrument sensitivity at the higher sample resistivities precluded such measurements. Drift mobility determinations, though complicated, would probably be the definitive method of obtaining information on the influence of localized states at low temperatures (see Appendix).

The optical gap, presumed to be the energy gap between extended states of the conduction and valence bands, $\varepsilon_c - \varepsilon_v$, corresponds to the mobility gap (Fig. 13). The result that $\varepsilon_c - \varepsilon_f$ appears to be greater than $\varepsilon_f - \varepsilon_v$ for all the samples measured (Table 7) suggests that the reason for predominant hole conduction in amorphous materials stems from their lower activation energy. This agrees with all the theoretical density-of-states models (Figs. 12, 14, and 16) proposed to explain electrical conduction in these materials. Note that even if the second peak in a transmission spectrum is used to calculate $\Delta\varepsilon_{opt}$, $\varepsilon_f - \varepsilon_v < \varepsilon_c - \varepsilon_f$. For example, the second peak in Figure 47 for $Ge_{15}Se_4Te_{81}$ occurs at 1.47 μm corresponding to a $\Delta\varepsilon_{opt}$ of 0.844 eV. Subtracting the value for $\varepsilon_f - \varepsilon_v$ determined from d.c. conductivity to be 0.38 eV yields 0.46 eV for $\varepsilon_c - \varepsilon_f$ so that ε_f is again not in the middle of the band gap but shifted toward the valence band.

EMPA studies on samples of $Ge_{15}Se_4Te_{81}$ and $Ge_{20}Se_{15}Te_{65}$ before and after switching did not detect significant changes in composition in the area of the electrodes or the filament formed between them. The slight increase in Te content from 81 at.% to 87 at.% and decrease in Ge content from 15 at.% to

9 at.% may indicate a composition change to a point just outside the glass-forming region, thus quenching to the crystalline state. Similarly, for $Ge_{20}Se_{15}Te_{65}$, the composition of the filament formed upon switching to the low resistance state appears to have decreased in Ge and Se content while increasing to ~69 at.% Te. This would place the filament composition near the arbitrarily drawn border of the glass-forming region (Fig. 67). While these changes are so small as to be within the realm of experimental coincidence, they are in the right direction. A study of $Ge_{30}Se_{20}Te_{50}$ indicated a substantial increase in Te content in the filament area with corresponding decreases in Ge and Se contents, though no determination of the new composition was reported[88]. The same study included glasses of $Ge_{30}Se_{30}Te_{40}$ and $Ge_{30}Se_{40}Te_{30}$ which underwent threshold switching with filament formation being observed, but experienced little or no composition change, while $Ge_{30}Se_{30}Te_{20}$, $Se_{80}Te_{20}$ and $Se_{90}Te_{10}$ did not undergo switching, though some melting was observed.

These results appear on the phase diagram of Figure 67. Coupled with the DTA results of Figures 59 - 61, it is apparent that the tendency to undergo switching is linked to a materials' ability to undergo crystallization, even in threshold devices. Proximity to the edge of the glass-forming region, evidently reduces the need or the opportunity to undergo a compositional change before crystallization.

Experiments performed independently by Uttecht, *et al*[76],

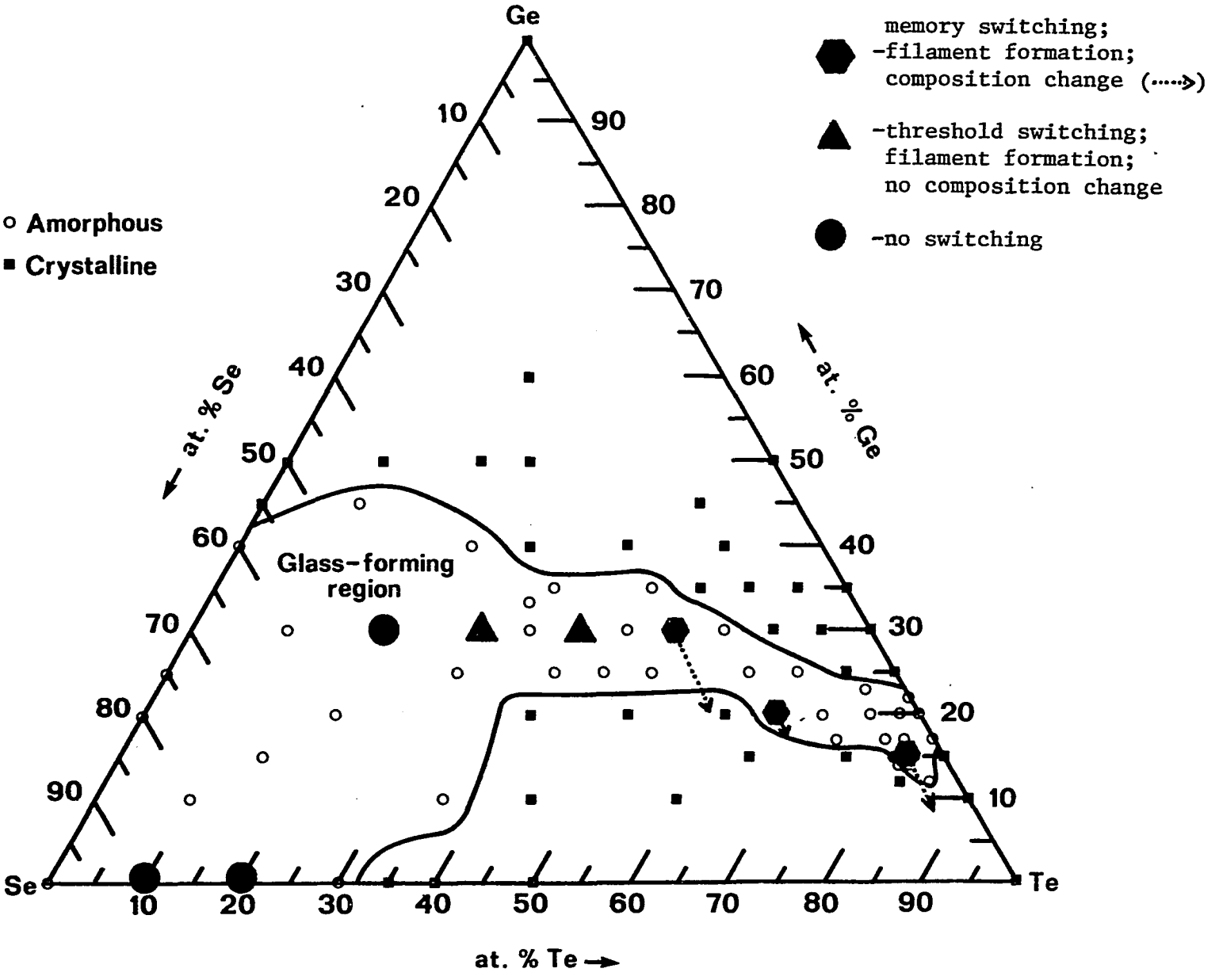

Figure 67. Results of switching experiments as they relate to the phase diagram of Ge-Se-Te.

and later by Tanaka, *et al*[89] on glasses in the Ge-As-Te system yield results from which similar conclusions may be drawn. The earlier work on $Ge_{10}As_{35}Te_{35}$ found a change in composition in the area of the filament formed upon switching. The new composition was determined to be $Ge_5As_{22}Te_{73}$ and the filament seemed to grow outward from the positive electrode. The later work on $Ge_{10}As_{45}Te_{45}$ and $Ge_{10}As_{20}Te_{70}$ found that $Ge_{10}As_{45}Te_{45}$ formed a filament containing almost pure Te at the anode and approached the composition of the crystalline eutectic As_2Te_3 along the rest of its length. The other composition, $Ge_{10}As_{20}Te_{70}$, formed a filament whose composition was determined to be close to that of the matrix. In the first composition the filament grew outward from the anode; in the second there was no directionality.

If the compositions studied are placed on a phase diagram of Ge-As-Te (Fig. 68) the glasses that undergo substantial composition changes in the filament area lie well within a glass-forming region. Those that undergo little or no composition change lie very near the edge of the glass-forming region. In any case, composition changes tend toward an increase in Te with corresponding decreases in the other two components.

The appearance of Te at the anode prompted the suggestion by Tanaka, *et al* that the switching mechanism included field-induced ionization of Te to Te^- and As to As^+ with consequent ion migration resulting in crystalline Te formation

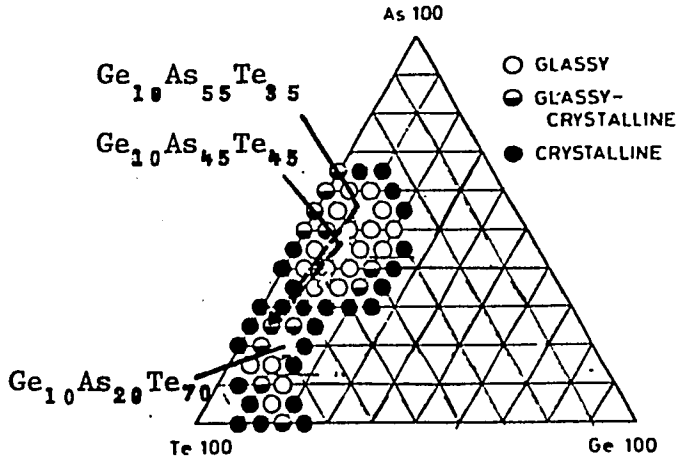

Figure 68. Results of switching experiments as they relate to the phase diagram of Ge-As-Te. Lines indicate composition changes in the filament upon switching. (Phase diagram after ref.89).

at the anode. The other composition, $Ge_{10}As_{20}Te_{70}$, rich in Te, crystallizes too rapidly to allow migration and, therefore, experiences little or no composition change.

Returning to the Ge-Se-Te system, x-ray micrographs taken before and after switching did not indicate any particular redistribution or enrichment of Te near the positive electrode (Fig. 58.2). In view of its rich Te content, this is to be expected for the $Ge_{20}Se_{15}Te_{65}$ glass. It was, nevertheless, hoped that x-ray micrographs would illustrate the ordering of non-crystalline material into the crystalline filament. This was not the case however, as the results only confirmed what had earlier been resolved at a conference on ordered structure in glasses held in the Soviet Union— "Other methods of studying the structure of substances, despite their extensive development in recent years, do not permit, for some reason or other, to reveal the regions of increased ordering in glass."[90].

From Figure 67 it is evident that, while memory switching requires the presence of sufficient readily crystallizing components, in this case Te, threshold switching will occur in compositions in the middle of the glass-forming region which are intermediate in their ability to undergo crystallization. Recent work by Saji and Kao[70] has shown that bulk samples of Ovshinsky's original threshold composition $Ge_{10}Si_{12}As_{30}Te_{48}$ undergo filament formation upon threshold switching and that, while V_{Th} decreases with increasing temperature, the

power required to produce switching, $I_{Th}V_{Th}$, remains the same. They also found that the device "locks" into a memory state as higher currents are passed in the threshold ON-state.

It would appear that, at least in bulk samples of amorphous material, switching, both threshold and memory, depends on the presence of some crystallizing component as well as thermal and kinetic effects which determine the extent and rate of crystallization.

VII. CONCLUSION

Glasses in the Ge-Se-Te system probably consist of mixtures of ordered and disordered domains which impart an overall short-range order to the glass creating a distinct energy gap. The sizes and number of ordered domains depends primarily on the tellurium content. The higher the Te content, the higher the conductivity and the lower the activation energy for conduction. The higher the Te content, the smaller the glass-forming region, the faster the crystallization process, and the lower the voltage required to produce switching.

One can view the glass-froming region in the Ge-Se-Te phase diagram as consisting of three overlapping areas. The narrow region on the right, rich in Te contains many microcrystalline domains in a disordered matrix. Under the influence of a high field, some electronic mechanism (avalanche breakdown, etc.) increases the current to the point where Joule heating causes the domains to consolidate into a small continuous channel which dissipates the heat rapidly on forming, but not fast enough to keep it from crystallizing. The crystalline filament in the memory device is thus formed. The rapid crystallization keeps the filament composition close to what it was before switching. The left side of the first area does not contain as many crystalline domains and the resulting slower crystallization rate enables the filament concentration to differ from the matrix

through a mechanism of ion migration or more likely due to factors stemming from the thermodynamically dependent solute-solvent liquid-solid phase transition, as in zone refining.

The second area, somewhat larger and to the left of the first, contains still fewer crystalline domains. When the field is applied, the domains begin to overlap, but do so only at higher voltages. As they begin forming a conductivity channel between the electrodes, they dissipate heat before they can crystallize to form larger filaments; they remain as overlapping microcrystalline domains as long as a holding current is maintained. High currents passed at this point will increase the sizes of these microcrystalline channels until lock-on to the memory state occurs. Adding a fourth or even fifth element to these compositions would decrease the chance of extensive overlap between the Te domains, thus increasing the stability of these threshold devices.

Finally, the third area, the largest and richest in Se content, is probably the closest to being a truly amorphous material in that DTA shows no distinct crystallization peaks and a sample of $Ge_{30}Se_{50}Te_{20}$ did not undergo switching of any sort even at fields greater than 45,000 V/cm.

APPENDIX

1. FORTRAN IV program and flow chart for the calculation of d-values from the Bragg Equation and comparison to the ASTM literature listings. (Written for the IBM 1130).

2. HP-9810A calculator program for calculating and plotting log σ vs. $10^3/T$, and determining $\varepsilon_f - \varepsilon_v$ and σ_0 from the least-squares slope and intercept. (For use with the HP-9862A plotter).

3. HP-9810A calculator program for plotting conductivity data as a function of temperature for different samples on a common set of coordinates (using the HP-9862A plotter).

4. HP-9810A calculator program for the determination of relative x-ray peak intensity ratios and elemental compositions from electron microprobe data.

5. Drift Mobility

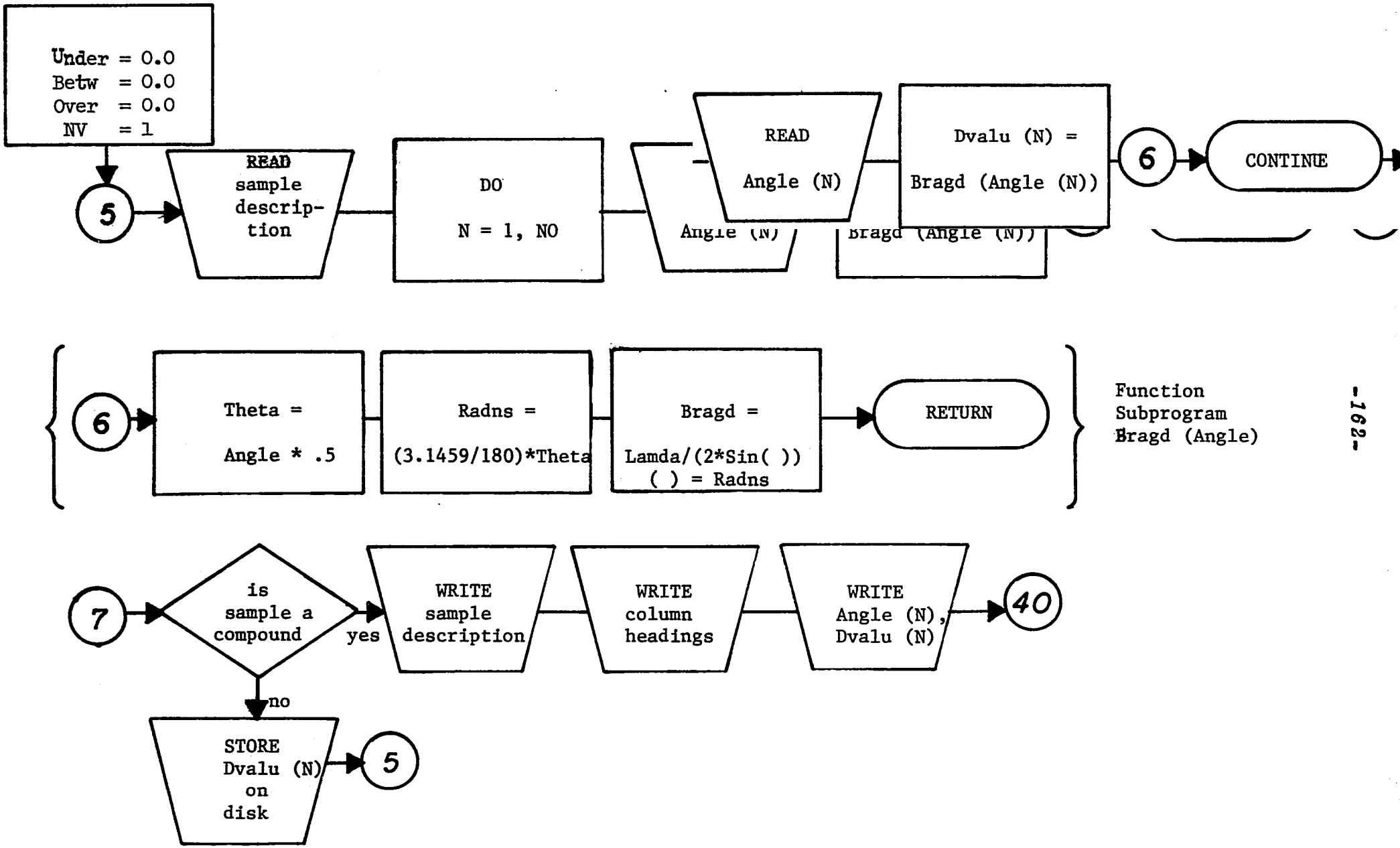
Under = 0.0
Betw = 0.0
Over = 0.0
NV = 1
5
READ sample description
DO N = 1, NO
READ Angle (N)
Dvalu (N) = Bragd (Angle (N))
6
CONTINUE
6
Theta = Angle * .5
Radns = (3.1459/180)*Theta
Bragd = Lamda/(2*Sin( )) ( ) = Radns
RETURN
Function Subprogram Bragd (Angle)
7
is sample a compound
yes
WRITE sample description
WRITE column headings
WRITE Angle (N), Dvalu (N)
40
no
STORE Dvalu (N) on disk
5

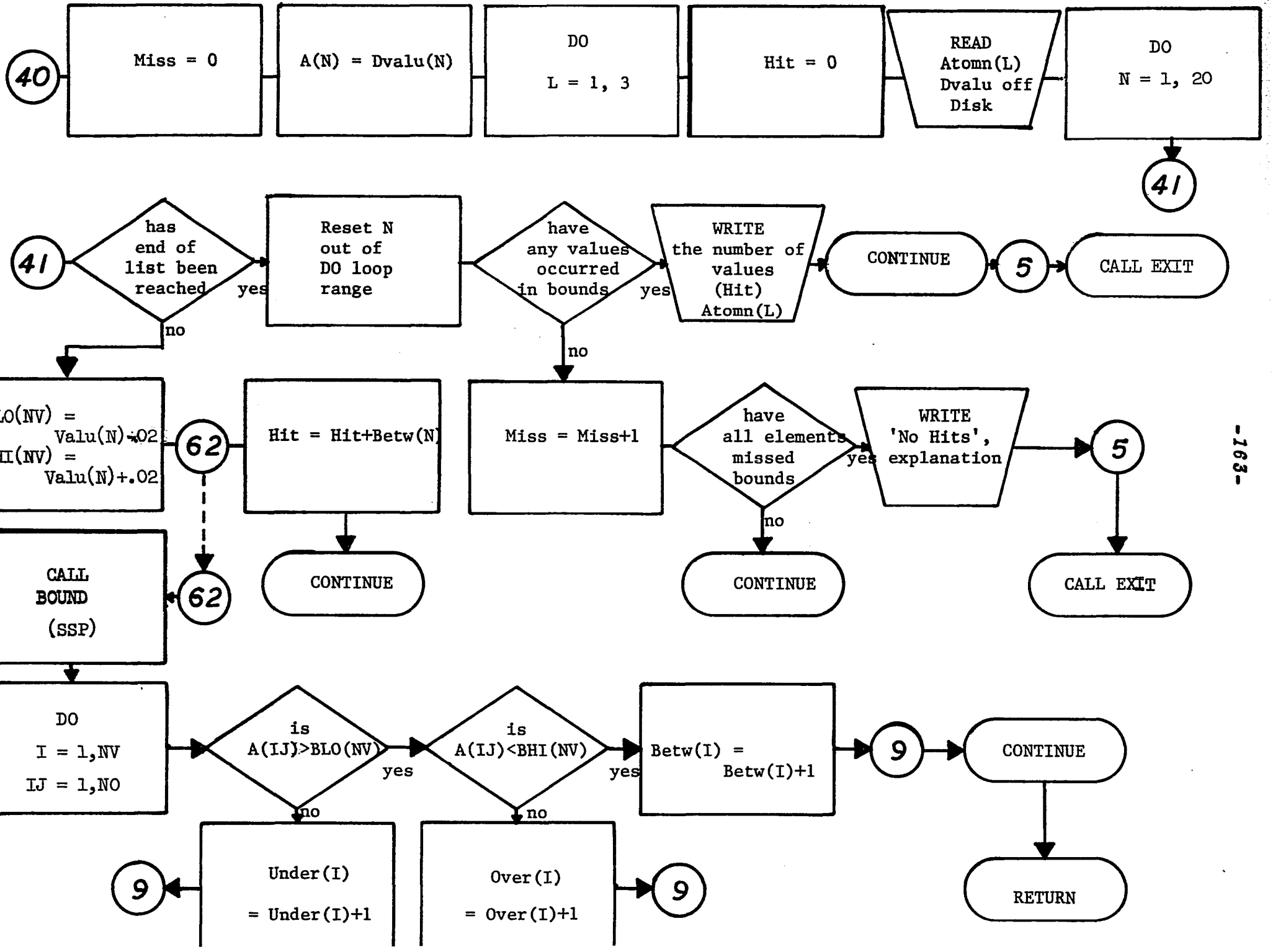
40
Miss = 0
A(N) = Dvalu(N)
DO
L = 1, 3
Hit = 0
READ
Atomn(L)
Dvalu off
Disk
DO
N = 1, 20
41
41
has
end of
list been
reached
yes
Reset N
out of
DO loop
range
have
any values
occurred
in bounds
yes
WRITE
the number of
values
(Hit)
Atomn(L)
CONTINUE
5
CALL EXIT
no
no
BLO(NV) =
Valu(N)-.02
BHI(NV) =
Valu(N)+.02
62
Hit = Hit+Betw(N)
Miss = Miss+1
have
all elements
missed
bounds
yes
WRITE
'No Hits',
explanation
5
CALL
BOUND
(SSP)
62
CONTINUE
no
CONTINUE
CALL EXIT
DO
I = 1,NV
IJ = 1,NO
is
A(IJ)>BLO(NV)
yes
is
A(IJ)<BHI(NV)
yes
Betw(I) =
Betw(I)+1
9
CONTINUE
no
no
9
Under(I)
= Under(I)+1
Over(I)
= Over(I)+1
9
RETURN

```
PAGE    1    CFCCCCOO

// JOB T                                                    CF000000

LCG DRIVE    CART SPEC    CART AVAIL   PHY DRIVE
  CCCC         CC05         C005         0000

V2 M08    ACTUAL 16K  CONFIG 16K

// FOR
* CNE WCRD INTEGERS
* LIST ALL
      FUNCTICN BRAGC(ANGLE)                                                    3
      REAL LAMCA                                                               4
      CATA LAMCA/1.514/                                                        5
C     THIS FUNCTION SUBPRCGRAM COMPUTES VALUES OF D FROM THE BRAGG             1
C     EQUATICN, USING LAMBCA AS THE VARIABLE FOR WAVELENGTH.
      THETA = ANGLE * .5                                                       7
      RADNS = 3.14159/180.0*THETA                                              7
      BRAGD = LAMDA/(2.0*SIN(RADNS))                                           8
      RETURN                                                                   9
      END                                                                      10
VARIABLE ALLCCATICNS
 BRAGD(R )=0000      LAMCA(R )=0002      THETA(R )=0004      RADNS(R )=0006

FEATURES SUPPCRTED
 CNE WCRD INTEGERS

CALLED SUBPRCGRAMS
 FSIN    FMPY    FCIV    FLD     FSTO    FDVR    SUBIN

REAL CCNSTANTS
  .50CCCOE 00=CC08    .314159E 01=000A    .180000E 03=000C    .200000E 01=000E

CCRE REQUIREMENTS FCR BRAGC
 CCMMCN      0  VARIABLES      8  PROGRAM      40

RELATIVE ENTRY PCINT ACCRESS IS 0010 (HEX)

END OF CCMPILATICN
```

```
// DUP

*STORE      WS  UA  BRAGD
CART ID C005   DB ADDR  5F2B   DB CNT   0004

// FOR
** CHECK FOR ELEMENTS REMAINING IN CRYSTALLINE PHASE,J. WIEDER-
* NAME CHECK
* ICCS(DISK, 2501 READER, 1403 PRINTER)
* ONE WORD INTEGERS
* LIST ALL

C       THIS PROGRAM READS EXPERIMENTAL VALUES FOR X-RAY DIFFRACTION DATA      1
C       IN TERMS OF DOUBLE ANGLES WHERE PEAKS HAVE OCCURRED, CALCULATES        2
C       THE D-VALUE FROM THE BRAGG EQUATION BY MEANS OF A FUNCTION             3
C       SUBPROGRAM, STORES THE VALUES FOR THE PURE ELEMENTS ON DISK,           4
C       USES SSP SUBROUTINE BOUND TO COMPARE VALUES FOR COMPOUNDS TO           5
C       THOSE OF THE ELEMENTS IT CONTAINS, IN ORDER TO DETERMINE IF THE        6
C       ELEMENTS ARE STILL PRESENT IN CRYSTALLINE FORM.                        7
        INTEGER ATOMN(3), SAMPL                                                8
        DIMENSION ANGLE(20),VALUE(20),DVALU(20),A(20),S(20),BLO(1),BHI(1)      9
       1  ,BETW(1),UNDER(1),OVER(1)
        EQUIVALENCE (A(1),S(1))                                                10
        DEFINE FILE 14(1,40,U,NREC),15(1,40,U,NREC),32(1,40,U,NREC),           11
       1  33(1,40,U,NREC),34(1,40,U,NREC),52(1,40,U,NREC)                     12
        BETW(1) = 0.0
        UNDER(1) = 0.0
        OVER(1) = 0.0
C       SET UP NUMBER OF VARIABLES, NV                                         13
        NV = 1                                                                 14
5       READ(8,10)(ATOMN(N),N = 1,3),SAMPL,NO                                  15
        DO 15 N = 1,NO                                                         16
        READ(8,23) ANGLE(N)                                                    17
        DVALU(N) = BRAGD(ANGLE(N))                                             20
15      CONTINUE                                                               22
        IF (ATOMN(2)) 30,30,6                                                  23
6       WRITE(5,19) ATOMN, SAMPL,NO                                            24
        WRITE(5,20)                                                            25
        WRITE(5,24)  (ANGLE(N), DVALU(N), N = 1,NO)                            26
        WRITE (5,27)
        GO TO 40                                                               27
C       IF SAMPLE IS AN ELEMENT, STORE ITS DVALUES ON DISK                     28
```

```
30    K = ATOMN(3)
      WRITE(5,22) DVALU
      WRITE(K'1) DVALU                                                    29
22    FORMAT (20F6.2)
      GO TO 5                                                             30
C     IF SAMPLE IS A COMPOUND (AT LEAST TWO ATOMIC NUMBERS) COMPARE WITH  31
C     ELEMENT LISTS. INITIALIZE HIT AND MISS COUNTERS TO ZERO.            32
40    MISS = 0                                                            33
C     DEFINE OBSERVATION MATRIX A(NO,NV) FOR SUBROUTINE (SSP)             34
      DO 41 N = 1,NO                                                      35
41    A(N) = DVALU(N)                                                     36
      DO 84 L = 1,3                                                       37
      HIT = 0.0                                                           38
      J = ATOMN(L)
      READ(J'1) VALUE
      DO 65 N = 1,20                                                      40
C     CHECK WHETHER END OF LIST (ANGLE = 0, DVALUE = 1.51) HAS BEEN       41
C     REACHED. SET UP SUBROUTINE BOUNDS, BLO AND BHI.
      IF (VALUE(N) - 1.52) 70,70,60                                       42
60    BLO(NV) = VALUE(N) -.02                                             43
      BHI(NV) = VALUE(N) + .02                                            44
      CALL BOUND(A,S,BLO,BHI,UNDER,BETW,OVER,NO,NV)                       45
65    HIT = HIT + BETW(NV)                                                46
70    N = 21                                                              47
      IF (HIT - 1.0) 80,80,75                                             48
75    WRITE(5,25) HIT, ATOMN(L)                                           49
      GO TO 84
84    CONTINUE                                                            50
      GO TO 5                                                             51
80    MISS = MISS + 1                                                     52
      IF (MISS - 3) 84,85,85                                              53
85    WRITE(5,26)                                                         54
      GO TO 5                                                             55
10    FORMAT(3I3,4X,I3,5X,I2)                                             56
19    FORMAT('1SAMPLE CONTAINING ATOMIC NUMBERS', 3I3, ', OF COMPOSITION  57
     1 TYPE,', I3, ', WITH,',I2,' ANGLES AT WHICH PEAKS OCCURRED.',////)
20    FORMAT(1HO,T46,' ANGLE',10X,'D-VALUE',/)                            59
23    FORMAT(F6.2)                                                        60
24    FORMAT(T46,F6.2,9X,F6.2)                                            61
25    FORMAT('0SAMPLE SHOWS', F4.1,' PEAKS DUE TO ELEMENT NUMBER',I3,     62
     1' PRESENT IN CRYSTALLINE PHASE.')                                   63
26    FORMAT('0SAMPLE SHOWS CRYSTALLINE PHASE PRESENT, BUT NO ELEMENTAL   64
     1 FORMS ARE PRESENT, SOME REACTION HAVING TAKEN PLACE.')
27    FORMAT(/////)
      CALL EXIT                                                           65
```

```
RIABLE ALLCCATICNS
   A(R )=005C-002A      S(R )=0050-002A ANGLE(R )=0078-0052 VALUE(R )=00A0-007A DVALU(R )=00C8-00A2    BLO(R
 BHI(R )=00CC-00CC   BETW(R )=00CE-00CE UNDER(R )=00D0-00D0  OVER(R )=00D2-00D2    HIT(R )=00D4       ATOMN(I
AMPL(I )=00D9        NREC(I )=00DA         NV(I )=00DB          N(I )=00DC          NO(I )=00DD          K(I
MISS(I )=00DF          L(I )=00E0          J(I )=00E1

ATEMENT ALLCCATICNS
2   =C0F5  10   =C0F8  19   =00FF  20   =013C  23   =014B  24   =014D  25   =0152  26   =017C  27   =01B6
5   =0224  6    =0233  30   =0261  40   =0277  41   =027F  60   =02B8  65   =02DF  70   =02F3  75   =02FE
C   =0318  85   =0324

ATURES SUPPCRTED
NE WCRD INTEGERS
CCS

LLED SUBPRCGRAMS
RAGC    BCUNC    FACD     FADDX    FSUB     FLD      FLDX     FSTO     FSTOX    READZ    SRED     SWRT     SCOMP
ICAF    SICFX    SICIX    SIOF     SIOI     SUBSC    PRNZ     SDFIO    SDRED    SDWRT    SDCOM    SDAF

AL CCNSTANTS
.COCCCOE 00=CCE6     .152000E 01=00E8     .200000E-01=00EA     .100000E 01=00EC

TEGER CCNSTANTS
   1=COEE       8=00EF       3=00F0       5=00F1       0=00F2      20=00F3      21=00F4

RE REQUIREMENTS FCR CHECK
CMMCN       C  VARIABLES     230  PROGRAM     582

C OF CCMPILATION

 XEC
```

HP-9810A Program

CONDUCTIVITY CALCULATIONS, PLOT, AND ERROR ANALYSIS

Enter voltage, V, ↑, area/length, A/1, CONTINUE.
(for a.c. data, enter 1 in place of voltage value).

Enter current, i, ↑, temperature (°C), t, CONTINUE.
(for a.c. data, enter conductance in place of current).

After n^{th} data entry ($n \leq 19$), press CONTINUE.

Steps 0000-0026 store A/1 and V and prepare maxima and minima registers.

Steps 0027-0053 calculate and print T (°K) and $10^3/T$, select X_{min} and X_{max}, and store each value of x ($10^3/T$).

Steps 0054-0102 calculate and print σ and log σ, select Y_{max} and Y_{min}, and store each value of y (log σ).

Steps 0103-0152 calculate and store various sums for use in least-squares and statistical calculations.

Steps 0153-0230 calculate and print b (y-intercept), m (slope), and $\varepsilon_f - \varepsilon_v$ (the activation energy for conduction) from a least-squares calculation:

$$m = \frac{\Sigma y \Sigma x - n\Sigma xy}{(\Sigma x)^2 - n\Sigma x^2} \quad ; \text{ for n data entries}$$

$$b = \frac{\Sigma x \Sigma xy - \Sigma y \Sigma x^2}{(\Sigma x)^2 - n\Sigma x^2}$$

$$\varepsilon_f - \varepsilon_v = -0.1984(m)$$

Steps 0231-0255 calculate the value of a statistical factor, SF from:

$$SF = \frac{(\Sigma y^2 - \{b\Sigma y\}) - m\Sigma xy}{(n - 2)}$$

Steps 0256-0328 find the highest and lowest points on a least-squares line between X_{max} and X_{min}, and compare them with Y_{max} and Y_{min}. The extrema are then used to plot the line, expanding it to cover the entire graph.

Steps 0329-0404 calculate Δy ($|$actual y - least-squares y$|$) for each data point and store the sum $\Sigma(\Delta y)^2$ for use in statistical calculations.

Steps 0405-0427 plot each data point, expanding the plot to cover the entire graph by use of the scaling equations:

$$X_{plot} = \frac{(x - X_{min})}{(X_{max} - X_{min})} \cdot (9999)$$

$$Y_{plot} = \frac{(y - Y_{min})}{(Y_{max} - Y_{min})} \cdot (9999)$$

Steps 0428-0449 calculate the sum $\Sigma(x - \Sigma x/n)^2$ for use in statistical calculations.

Steps 0450-0489 calculate and print the following values:

standard error in slope $= \{SF/\Sigma(x - \Sigma x/n)^2\}^{\frac{1}{2}}$

standard error in intercept $= \{(SF)\Sigma x^2/n\Sigma(x - \Sigma x/n)^2\}^{\frac{1}{2}}$

r.m.s. deviation in log $\sigma = \{\Sigma(\Delta y)^2/n\}^{\frac{1}{2}}$

NOTE: Calculator must be shut off between different sample data in order to clear x and y storage registers (#'s: 001-019, 021-039).

```
0000--XTO---23
0001--  0  ---00
0002--  π  ---56
0003--YTO---40
0004--  0  ---00
0005--  2  ---02
0006--  0  ---00
0007--  2  ---02
0008--  0  ---00
0009--XTO---23
0010--  b  ---14
0011--XTO---23
0012--  0  ---00
0013--  4  ---04
0014--  1  ---01
0015--XTO---23
0016--  0  ---00
0017--  4  ---04
0018--  3  ---03
0019--CHS---32
0020--XTO---23
0021--  0  ---00
0022--  4  ---04
0023--  2  ---02
0024--CLX---37
0025--  UP---27
0026--  UP---27
0027--STP---41
0028--RUP---22
0029--X=Y---50
0030--  0  ---00
0031--  1  ---01
0032--  5  ---05
0033--  3  ---03
0034--  2  ---02
0035--  7  ---07
0036--  3  ---03
0037--  .  ---21
0038--  1  ---01
0039--  5  ---05
0040--  +  ---33
0041--EEX---26
0042--  3  ---03
0043--XEY---30
0044--PNT---45
0045--DIV---35
0046--XFR---67
0047--  0  ---00
0048--  4  ---04
0049--  0  ---00
0050--X<Y---52
0051--YTO---40
0052--  0  ---00
0053--  4  ---04
0054--  0  ---00
0055--XFR---67
0056--  0  ---00
0057--  4  ---04
0058--  1  ---01
0059--X>Y---53
0060--YTO---40
0061--  0  ---00
0062--  4  ---04
0063--  1  ---01
0064--RUP---22
0065--XFR---67
0066--DIV---35
0067--  0  ---00
0068--  2  ---02
0069--  0  ---00
0070--XEY---30
0071--XFR---67
0072--  0  ---00
0073--IND---31
0074--1/X---17
0075--  X  ---36
0076--  1  ---01
0077--  0  ---00
0078--  I  ---65
0079--XEY---30
0080--PNT---45
0081--  I  ---65
0082--XEY---30
0083--DIV---35
0084--XFR---67
0085--  0  ---00
0086--  4  ---04
0087--  2  ---02
0088--X<Y---52
0089--YTO---40
0090--  0  ---00
0091--  4  ---04
0092--  2  ---02
0093--XFR---67
0094--  0  ---00
0095--  4  ---04
0096--  3  ---03
0097--X>Y---53
0098--YTO---40
0099--  0  ---00
0100--  4  ---04
0101--  3  ---03
0102--  1  ---01
0103--XTO---23
0104--  !  ---33
0105--  a  ---13
0106--XTO---23
0107--  +  ---33
0108--  b  ---14
0109--  DN---25
0110--  X  ---36
0111--YTO---40
0112--  +  ---33
0113--  0  ---00
0114--  4  ---04
0115--  4  ---04
0116--RUP---22
0117--PNT---45
0118--XTO---23
0119--  +  ---33
0120--  0  ---00
0121--  4  ---04
0122--  5  ---05
0123--XTO---23
0124--IND---31
0125--  a  ---13
0126--XSQ---12
0127--XTO---23
0128--  +  ---33
0129--  0  ---00
0130--  4  ---04
0131--  6  ---06
0132--XEY---30
0133--PNT---45
0134--PNT---45
0135--XTO---23
0136--  +  ---33
0137--  0  ---00
0138--  4  ---04
0139--  7  ---07
0140--XTO---23
0141--IND---31
0142--  b  ---14
0143--XSQ---12
0144--XTO---23
0145--  +  ---33
0146--  0  ---00
0147--  4  ---04
0148--  8  ---10
0149--GTO---44
```

```
0150--  2  ---02
0151--  4  ---04
0152--  +  ---33
0153--XFR---67
0154--  0  ---00
0155--  4  ---04
0156--  5  ---05
0157--  UP---27
0158--XFR---67
0159--  X  ---36
0160--  0  ---00
0161--  4  ---04
0162--  4  ---04
0163--  UP---27
0164--XFR---67
0165--  0  ---00
0166--  4  ---04
0167--  6  ---06
0168--XFR---67
0169--  X  ---36
0170--  0  ---00
0171--  4  ---04
0172--  7  ---07
0173--  -  ---34
0174--RUP---22
0175--XSQ---12
0176--XEY---30
0177--  a  ---13
0178--XFR---67
0179--  X  ---36
0180--  0  ---00
0181--  4  ---04
0182--  6  ---06
0183--  -  ---34
0184--  DN---25
0185--DIV---35
0186--YTO---40
0187--  0  ---00
0188--  2  ---02
0189--  0  ---00
0190--  UP---27
0191--XFR---67
0192--  0  ---00
0193--  4  ---04
0194--  5  ---05
0195--XFR---67
0196--  X  ---36
0197--  0  ---00
0198--  4  ---04
0199--  7  ---07
0200--RUP---22
0201--PNT---45
0202--  a  ---13
0203--XFR---67
0204--  X  ---36
0205--  0  ---00
0206--  4  ---04
0207--  4  ---04
0208--  -  ---34
0209--XEY---30
0210--RUP---22
0211--DIV---35
0212--  .  ---21
0213--  1  ---01
0214--  9  ---11
0215--  8  ---10
0216--  4  ---04
0217--CHS---32
0218--XEY---30
0219--  X  ---36
0220--PNT---45
0221--XTO---23
0222--  0  ---00
0223--  4  ---04
0224--  4  ---04
0225--RUP---22
0226--  X  ---36
0227--  a  ---13
0228--DIV---35
0229--RUP---22
0230--PNT---45
0231--  2  ---02
0232--  -  ---34
0233--XFR---67
0234--  0  ---00
0235--  2  ---02
0236--  0  ---00
0237--XFR---67
0238--  X  ---36
0239--  0  ---00
0240--  4  ---04
0241--  7  ---07
0242--CHS---32
0243--RUP---22
0244--  -  ---34
0245--XFR---67
0246--  0  ---00
0247--  4  ---04
0248--  8  ---10
0249--  +  ---33
0250--  DN---25
0251--XEY---30
0252--DIV---35
0253--YTO---40
0254--  0  ---00
0255--  +  ---33
0256--XFR---67
0257--  0  ---00
0258--  4  ---04
0259--  4  ---04
0260--  UP---27
0261--XFR---67
0262--  X  ---36
0263--  0  ---00
0264--  4  ---04
0265--  0  ---00
0266--RUP---22
0267--XFR---67
0268--  0  ---00
0269--  2  ---02
0270--  0  ---00
0271--  +  ---33
0272--RUP---22
0273--XFR---67
0274--  X  ---36
0275--  0  ---00
0276--  4  ---04
0277--  1  ---01
0278--  +  ---33
0279--XFR---67
0280--  0  ---00
0281--  4  ---04
0282--  2  ---02
0283--X<Y---52
0284--YTO---40
0285--  0  ---00
0286--  4  ---04
0287--  2  ---02
0288--RUP---22
0289--XEY---30
0290--XFR---67
0291--  0  ---00
0292--  4  ---04
0293--  3  ---03
0294--X>Y---53
0295--YTO---40
0296--  0  ---00
0297--  4  ---04
0298--  3  ---03
0299--XFR---67
```

```
0300--  0  ---00
0301--  4  ---04
0302--  3  ---03
0303--  -  ---34
0304--RUP---22
0305--XEY---30
0306--  -  ---34
0307--CHS---32
0308--XFR---67
0309--  +  ---33
0310--  0  ---00
0311--  4  ---04
0312--  2  ---02
0313--DIV---35
0314--1/X---17
0315--RUP---22
0316--  X  ---36
0317--  9  ---11
0318--  9  ---11
0319--  9  ---11
0320--  9  ---11
0321--  X  ---36
0322--FMT---42
0323--  UP---27
0324--RUP---22
0325--  X  ---36
0326--CLX---37
0327--FMT---42
0328--  DN---25
0329--XTO---23
0330--  0  ---00
0331--  4  ---04
0332--  7  ---07
0333--XTO---23
0334--  0  ---00
0335--  4  ---04
0336--  8  ---10
0337--XTO---23
0338--  6  ---14
0339--  a  ---13
0340--XTO---23
0341--DIV---35
0342--  0  ---00
0343--  4  ---04
0344--  5  ---05
0345--  1  ---01
0346--XTO---23
0347--  +  ---33
0348--  6  ---14
0349--  2  ---02
```

```
0350--  0  ---00
0351--XTO---23
0352--  +  ---33
0353--  6  ---14
0354--  UP---27
0355--XFR---67
0356--IND---31
0357--  6  ---14
0358--  UP---27
0359--RUP---22
0360--XTO---23
0361--  -  ---34
0362--  6  ---14
0363--XFR---67
0364--  0  ---00
0365--  4  ---04
0366--  3  ---03
0367--  -  ---34
0368--CHS---32
0369--XFR---67
0370--  +  ---33
0371--  0  ---00
0372--  4  ---04
0373--  2  ---02
0374--DIV---35
0375--XFR---67
0376--IND---31
0377--  6  ---14
0378--XFR---67
0379--  X  ---36
0380--  0  ---00
0381--  4  ---04
0382--  4  ---04
0383--XFR---67
0384--  +  ---33
0385--  0  ---00
0386--  2  ---02
0387--  0  ---00
0388--RUP---22
0389--  -  ---34
0390--XFR---67
0391--IND---31
0392--  6  ---14
0393--XFR---67
0394--  -  ---34
0395--  0  ---00
0396--  4  ---04
0397--  1  ---01
0398--XEY---30
0399--XSQ---12
```

```
0400--XTO---23
0401--  +  ---33
0402--  0  ---00
0403--  4  ---04
0404--  7  ---07
0405--XFR---67
0406--  0  ---00
0407--  4  ---04
0408--  0  ---00
0409--XFR---67
0410--  -  ---34
0411--  0  ---00
0412--  4  ---04
0413--  1  ---01
0414--DIV---35
0415--  9  ---11
0416--  9  ---11
0417--  9  ---11
0418--  9  ---11
0419--  X  ---36
0420--RUP---22
0421--  X  ---36
0422--  DN---25
0423--XEY---30
0424--FMT---42
0425--  UP---27
0426--FMT---42
0427--  DN---25
0428--XFR---67
0429--IND---31
0430--  b  ---14
0431--XFR---67
0432--  -  ---34
0433--  0  ---00
0434--  4  ---04
0435--  5  ---05
0436--XSQ---12
0437--XTO---23
0438--  +  ---33
0439--  0  ---00
0440--  4  ---04
0441--  8  ---10
0442--  b  ---14
0443--  UP---27
0444--  a  ---13
0445--X=Y---50
0446--  0  ---00
0447--  4  ---04
0448--  5  ---05
0449--  3  ---03
```

```
0450--GTO---44
0451--  0  ---00
0452--  3  ---03
0453--  4  ---04
0454--  5  ---05
0455--XFR---67
0456--  0  ---00
0457--  4  ---04
0458--  8  ---10
0459--1/X---17
0460--XFR---67
0461--  X  ---36
0462--  0  ---00
0463--PSE---57
0464--  UP---27
0465--  r  ---76
0466--PNT---45
0467--XFR---67
0468--  0  ---00
0469--  4  ---04
0470--  6  ---06
0471--  X  ---36
0472--  a  ---13
0473--DIV---35
0474--1/X---17
0475--XEY---30
0476--  r  ---76
0477--PNT---45
0478--XFR---67
0479--  0  ---00
0480--  4  ---04
0481--  7  ---07
0482--  X  ---36
0483--  DN---25
0484--  r  ---76
0485--PNT---45
0486--CLX---37
0487--  UP---27
0488--  UP---27
0489--END---46
```

HP9810A Program

COMMON COORDINATE CONDUCTIVITIES

Enter intercept, b, ↑, slope, m, CONTINUE.

Enter V, ↑, A/l, CONTINUE.

Enter i, ↑, t, CONTINUE.

After last data entry press CONTINUE.

Steps 0000-0025 store m, b, A/l, and V.

Steps 0026-0064 calculate the abcissa, $10^3/T$, and select values of X_{min} and X_{max} for use in plotter scaling equations.

Steps 0065-0085 calculate the values for the ordinate, log σ .

Steps 0086-0120 plot all the data points on a graph with the coordinate ranges currently being:

y-axis: -2 to -11
x-axis: 5 to 2

Steps 0121-0207 plot a least-squares line between the data points containing X_{min} and X_{max} .

Steps 0208-0215 restore the X_{max} memory register to zero.

```
0000--CNT---47
0001--XTO---23
0002--  0 ---00
0003--  0 ---00
0004--  0 ---00
0005--YTO---40
0006--  0 ---00
0007--  0 ---00
0008--  1 ---01
0009--STP---41
0010--XTO---23
0011--  0 ---00
0012--  0 ---00
0013--  2 ---02
0014--YTO---40
0015--  0 ---00
0016--  0 ---00
0017--  3 ---03
0018--  9 ---11
0019--CNT---47
0020--XTO---23
0021--  0 ---00
0022--  0 ---00
0023--  4 ---04
0024--CLR---20
0025--STP---41
0026--RUP---22
0027--X=Y---50
0028--  0 ---00
0029--  1 ---01
0030--  2 ---02
0031--  1 ---01
0032--  2 ---02
0033--  7 ---07
0034--  3 ---03
0035--  . ---21
0036--  1 ---01
0037--  5 ---05
0038--  + ---33
0039--  1 ---01
0040--  0 ---00
0041--  0 ---00
0042--  0 ---00
0043--XEY---30
0044--DIV---35
0045--XFR---67
0046--  0 ---00
0047--  0 ---00
0048--  4 ---04
0049--CNT---47
```

```
0050--CNT---47
0051--X>Y---53
0052--YTO---40
0053--  0 ---00
0054--  0 ---00
0055--  4 ---04
0056--XFR---67
0057--  0 ---00
0058--  0 ---00
0059--  5 ---05
0060--X<Y---52
0061--YTO---40
0062--  0 ---00
0063--  0 ---00
0064--  5 ---05
0065--XFR---67
0066--  0 ---00
0067--  0 ---00
0068--  2 ---02
0069--1/X---17
0070--RUP---22
0071--XFR---67
0072--DIV---35
0073--  0 ---00
0074--  0 ---00
0075--  3 ---03
0076--  % ---36
0077--  DN---25
0078--CNT---47
0079--  I ---65
0080--  UP---27
0081--  1 ---01
0082--  0 ---00
0083--  I ---65
0084--DIV---35
0085--CNT---47
0086--  1 ---01
0087--  1 ---01
0088--  + ---33
0089--  9 ---11
0090--CNT---47
0091--CNT---47
0092--DIV---35
0093--RUP---22
0094--XEY---30
0095--  2 ---02
0096--  - ---34
0097--  3 ---03
0098--DIV---35
0099--CNT---47
```

```
0100--CNT---47
0101--  9  ---11
0102--  9  ---11
0103--  9  ---11
0104--  9  ---11
0105--  X  ---36
0106--RUP---22
0107--  X  ---36
0108--  DN---25
0109--XEY---30
0110--FMT---42
0111--  UP---27
0112--FMT---42
0113--  DN---25
0114--CNT---47
0115--CNT---47
0116--GTO---44
0117--  0  ---00
0118--  0  ---00
0119--  2  ---02
0120--  4  ---04
0121--CNT---47
0122--CNT---47
0123--XFR---67
0124--  0  ---00
0125--  0  ---00
0126--  5  ---05
0127--  UP---27
0128--XFR---67
0129--  X  ---36
0130--  0  ---00
0131--  0  ---00
0132--  0  ---00
0133--XFR---67
0134--  +  ---33
0135--  0  ---00
0136--  0  ---00
0137--  1  ---01
0138--  UP---27
0139--CNT---47
0140--  1  ---01
0141--  1  ---01
0142--  +  ---33
0143--  9  ---11
0144--CNT---47
0145--CNT---47
0146--DIV---35
0147--RUP---22
0148--XEY---30
0149--CNT---47
0150--CNT---47
0151--  2  ---02
0152--  -  ---34
0153--  3  ---03
0154--DIV---35
0155--  9  ---11
0156--  9  ---11
0157--  9  ---11
0158--  9  ---11
0159--  X  ---36
0160--RUP---22
0161--  X  ---36
0162--  DN---25
0163--XEY---30
0164--FMT---42
0165--  UP---27
0166--XFR---67
0167--  0  ---00
0168--  0  ---00
0169--  4  ---04
0170--  UP---27
0171--XFR---67
0172--  X  ---36
0173--  0  ---00
0174--  0  ---00
0175--  0  ---00
0176--XFR---67
0177--  +  ---33
0178--  0  ---00
0179--  0  ---00
0180--  1  ---01
0181--  UP---27
0182--  1  ---01
0183--  1  ---01
0184--  +  ---33
0185--  9  ---11
0186--CNT---47
0187--CNT---47
0188--DIV---35
0189--RUP---22
0190--XEY---30
0191--  2  ---02
0192--  -  ---34
0193--  3  ---03
0194--DIV---35
0195--  9  ---11
0196--  9  ---11
0197--  9  ---11
0198--  9  ---11
0199--CNT---47
0200--CNT---47
0201--  X  ---36
0202--RUP---22
0203--  X  ---36
0204--  DN---25
0205--XEY---30
0206--FMT---42
0207--  DN---25
0208--CNT---47
0209--CLR---20
0210--XTO---23
0211--  0  ---00
0212--  0  ---00
0213--  5  ---05
0214--PSE---57
0215--END---46
```

HP-9810A Program

ELECTRON MICROPROBE ANALYSIS

Enter intensities for standards, I_0 .

I_0 for Ge, x→( ), 0 0 1
I_0 for Se, x→( ), 0 0 2
I_0 for Te, x→( ), 0 0 3

Press 'Go To' 0 1 3 8, CONTINUE, in order to load atomic weights and other constants.

Enter intensities for sample, I .

I for Ge, ↑
I for Se, ↑
I for Te, CONTINUE

Steps 0000-0029 print intensity entries after first correcting the Se_{K_α} value for peak overlap from Ge_{K_β} .

Steps 0030-0054 calculate and print relative peak intensity ratios.

Steps 0055-0137 calculate and print the atomic per cent composition.

Steps 0138-0181 load constants into memory registers 0 1 0, 0 1 1, 0 1 2, 0 4 0, 0 4 5.

```
0000--RUP---22
0001--XTO---23
0002--  0 ---00
0003--  2 ---02
0004--  0 ---00
0005--XFR---67
0006--  X ---36
0007--  0 ---00
0008--  4 ---04
0009--  5 ---05
0010--RUP---22
0011--XEY---30
0012--  - ---34
0013--  0 ---00
0014--X<Y---52
0015--  0 ---00
0016--  0 ---00
0017--  2 ---02
0018--  0 ---00
0019--XEY---30
0020--XFR---67
0021--  0 ---00
0022--  2 ---02
0023--  0 ---00
0024--PNT---45
0025--XEY---30
0026--PNT---45
0027--RUP---22
0028--PNT---45
0029--PNT---45
0030--RUP---22
0031--XFR---67
0032--DIV---35
0033--  0 ---00
0034--  0 ---00
0035--  1 ---01
0036--RUP---22
0037--XFR---67
0038--DIV---35
0039--  0 ---00
0040--  0 ---00
0041--  2 ---02
0042--RUP---22
0043--XFR---67
0044--DIV---35
0045--  0 ---00
0046--  0 ---00
0047--  3 ---03
0048--RUP---22
0049--PNT---45
0050--RUP---22
0051--PNT---45
0052--RUP---22
0053--PNT---45
0054--PNT---45
0055--RUP---22
0056--XFR---67
0057--DIV---35
0058--  0 ---00
0059--  1 ---01
0060--  0 ---00
0061--RUP---22
0062--XFR---67
0063--DIV---35
0064--  0 ---00
0065--  1 ---01
0066--  1 ---01
0067--RUP---22
0068--XFR---67
0069--DIV---35
0070--  0 ---00
0071--  1 ---01
0072--  2 ---02
0073--RUP---22
0074--XTO---23
0075--  0 ---00
0076--  3 ---03
0077--  0 ---00
0078--RUP---22
0079--XTO---23
0080--  + ---33
0081--  0 ---00
0082--  3 ---03
0083--  0 ---00
0084--RUP---22
0085--XTO---23
0086--  + ---33
0087--  0 ---00
0088--  3 ---03
0089--  0 ---00
0090--RUP---22
0091--XFR---67
0092--DIV---35
0093--  0 ---00
0094--  3 ---03
0095--  0 ---00
0096--XFR---67
0097--  X ---36
0098--  0 ---00
0099--  4 ---04
```

```
0100--  0  ---00
0101--RUP---22
0102--XFR---67
0103--DIV---35
0104--  0  ---00
0105--  3  ---03
0106--  0  ---00
0107--XFR---67
0108--  X  ---36
0109--  0  ---00
0110--  4  ---04
0111--  0  ---00
0112--RUP---22
0113--XFR---67
0114--DIV---35
0115--  0  ---00
0116--  3  ---03
0117--  0  ---00
0118--XFR---67
0119--  X  ---36
0120--  0  ---00
0121--  4  ---04
0122--  0  ---00
0123--RUP---22
0124--PNT---45
0125--RUP---22
0126--PNT---45
0127--RUP---22
0128--PNT---45
0129--PNT---45
0130--PNT---45
0131--PNT---45
0132--GTO---44
0133--  0  ---00
0134--  1  ---01
0135--  8  ---10
0136--  1  ---01
0137--CNT---47
0138--  7  ---07
0139--  2  ---02
0140--  .  ---21
0141--  5  ---05
0142--  9  ---11
0143--XTO---23
0144--  0  ---00
0145--  1  ---01
0146--  0  ---00
0147--  7  ---07
0148--  8  ---10
0149--  .  ---21
0150--  9  ---11
0151--  6  ---06
0152--XTO---23
0153--  0  ---00
0154--  1  ---01
0155--  1  ---01
0156--  1  ---01
0157--  2  ---02
0158--  7  ---07
0159--  .  ---21
0160--  6  ---06
0161--XTO---23
0162--  0  ---00
0163--  1  ---01
0164--  2  ---02
0165--  1  ---01
0166--  0  ---00
0167--  0  ---00
0168--XTO---23
0169--  0  ---00
0170--  4  ---04
0171--  0  ---00
0172--  .  ---21
0173--  0  ---00
0174--  4  ---04
0175--  0  ---00
0176--  0  ---00
0177--XTO---23
0178--  0  ---00
0179--  4  ---04
0180--  5  ---05
0181--END---46
```

Drift Mobilty

Because conduction in localized states differs from that in extended states primarily in the small value of the drift mobility found for a hopping mechanism, measurement of the drift mobility provides a means of obtaining information about these states. Values for the drift mobility over a range of temperature would also indicate the extent to which carrier trapping affects the conduction process.[14]

Excess carriers are created in a thin sample (≃400μm) or film (<50μm) by either an electrical pulse or a pulsed optical or electron beam of energy near the absorption edge of the amorphous material. The sheet of charge that is created moves along the thickness of the sample, d, under the influence of a field, $\vec{E} = \vec{V}/d$. By changing the polarity of the field, the carriers that drift across can be picked to be either holes or electrons. In either case, the time t_t for the carriers to cross to the opposite electrode can be observed as a square-like current transient ($CR<<t_t$) or a ramp-like charge transient ($CR>>t_t$) as in Fig. 1, and will be given by

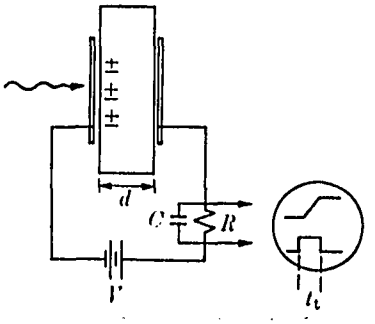

Figure 1. Experimental arrangement for drift mobility study.

$$t_t = d^2/\mu_D V \qquad (1)$$

where μ_D is the drift mobility.

In the presence of traps (Fig. 2), the drift mobility will be lower

than the conductivity mobility, μ_o, because of the time, τ_r, that some of the carriers will spend in traps. Assuming a shallow level of trap states, i.e. near a band edge, such that N_t lies at an energy ε_t below the conducting states, N_c, and $\tau_r << t_t$, $\tau << t_t$, then the drift mobility will be

$$\mu_D = \mu_o \left(\frac{n_o}{n_o + n_t} \right) \tag{2}$$

where n_o and n_t are the numbers of free and trapped carriers respectively.

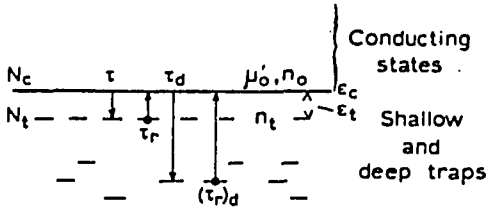

Figure 2. Schematic of deep and shallow trapping centers. τ and τ_r refer to shallow traps and denote the free electron lifetime and the average time before thermal release respectively; τ_d and $(\tau_r)_d$ are the corresponding quantities for deep traps.

Assuming a thermal distribution of carriers,

$$n_t/n_o = N_t/N_c [e^{(\varepsilon_t/kT)}] \tag{3}$$

so that the drift mobility becomes

$$\mu_D = \mu_o [1 + (N_t/N_c) e^{-(\varepsilon_t/kT)}]^{-1} \tag{4}$$

At higher temperatures, trapping becomes negligible as $\mu_D = \mu_o$. However, at low temperatures, the exponential term dominates giving

$$\mu_D \simeq \mu_o (N_c/N_t) e^{-(\varepsilon_t/kT)} \tag{5}$$

Experimentally, measuring μ_D at higher temperatures would thus

yield μ_o, while over a lower temperature range, a plot of ln μ_D vs. 1/T would give the trap depth. Switching polarities would enable this information to be obtained for both hole and electron carriers.[91]

In non-crystalline semiconductors, this analysis becomes somewhat ambiguous if the trap states or density of localized states varies extensively over a range of energies rather than existing primarily at ε_t.[14] Also, it is difficult to determine how much of a particular drift mobility value is due to trap limitation of conduction in extended states and how much to conduction in localized states. In other words, given a small drift mobility, is it small because of the effect of trapping states becoming dominant or because conduction at that temperature is by a hopping mechanism? This is easily resolved, however, if the two situations are considered to be synonymous in amorphous materials, as suggested in the discussion of the CFO theory (Sec. IIB).

An attempt to perform a drift mobility experiment using a Fexitron 730 Pulser, model 2710, yielding 30 nsec x-ray or electron pulses was considered. Thin-film samples were evaporated onto conducting glass substrates (quartz disks impregnated with SnO_2)[92] and coated with gold films, so that the resulting sandwich electrode geometry would permit radiation to enter from one side. Actual results, however, were not obtained for lack of time to implement the experiment in all its technical complexity.

REFERENCES

1. B. T. Kolomiets, Phys. Stat. Sol., 7, 359, 713 (1964).

2. S. R. Ovshinsky, Phys. Rev. Letters, 21, 1450 (1968).

3. S. R. Ovshinsky, J. Non-Crystalline Solids, 2, 99 (1970).

4. H. Ehrenreich, Chrmn. of the Ad Hoc Committee for the Fundamentals of Amorphous Semiconductors in *Fundamentals of Amorphous Semiconductors*, National Academy of Sciences, Washington D.C., 1972, p. 94.

5. R. F. Shaw, Engineering, May 29, 1969, p. 783.

6. J. M. Ziman, *Electrons in Metals*, Taylor & Francis, Ltd., London, 1963, p. 44.

7. J. P. McKelvey, *Solid State and Semiconductor Physics*, Harper & Row, New York, 1966, Chaps. 5, 8-11.

8. L. Banyai, *Physique des Semiconductors*, Dunod, Paris, 1964, p. 417.

9. F. Gutmann and L. E. Lyons, *Organic Semiconductors*, John Wiley & Sons, New York, 1967, Chaps. 1,4,7, & 8.

10. J. Bardeen and W. Shockley, Phys. Rev., 8, 72, (1950).

11. L. P. Hunter, *Introduction to Semiconductor Phenomena and Devices*, Addison-Wesley, New York, 1966, Chaps. 1 & 2.

12. C. Kittel, *Introduction to Solid State Physics*, 3rd Ed., John Wiley & Sons, New York, 1967, Chaps. 9 & 10.

13. W. C. Dunlap, *An Introduction to Semiconductors*, John Wiley & Sons, New York, 1957, Chaps. 5-7, & 9.

14. N. F. Mott and E. A. Davis, *Electronic Processes in Non-Crystalline Materials*, Oxford University Press, London, 1971.

15. F. J. Morin, *Semiconductors*, Ed. by N. B. Hannay, Rheinhold Publishing Corp., New York, 1959, p. 600.

16. N. F. Mott, Contemp. Phys., 10, 125 (1969).

17. A. F. Ioffe and A. R. Regel, *Progress in Semiconductors*, A. F. Gibson, ed., Heywood & Co., Ltd., London, Vol. 4, 1960, p. 237.

18. N. F. Mott, Advan. Phys., 16, 49 (1967).

19. M. H. Cohen, H. Fritzche, and S. R. Ovshinsky, Phys. Rev. Letters, 22, 1065 (1969).

20. D. Adler, Electronics, 43, 61 (9/28/70).

21. K. E. Khor and P. V. Smith, J. Phys. C: Solid State Phys., 4, 2029, 2041 (1971).

22. A. I. Gubanov, *Quantum Electron Theory of Amorphous Semiconductors*, Consultants Bureau, New York, 1965.

23. P. W. Anderson, Phys. Rev., 109, 1492 (1958).

24. N. F. Mott and W. D. Twose, Adv. Phys., 10, 107, (1961).

25. A. R. Hilton and M. Brau, Infrared Phys., 3, 69 (1963).

26. A. R. Hilton and M. Brau, Infrared Phys., 4, 213 (1964).

27. A. Efstathiou, D. M. Hoffman, and E. R. Levin, J. Vac. Sci. & Tech., 6, 383 (1969).

28. H. Rawson, *Inorganic Glass-Forming Systems*, Academic Press, Ltd., London, 1967, Chapter 16.

29. H. Krebs, Angew. Chem., 70, 615 (1958).

30. M. H. Cohen, Physics Today, May 1971, p. 26.

31. I. G. Austin and N. F. Mott, Adv. in Phys., 18, 41 (1969).

32. A. E. Owen and J. M. Robertson, J. Non-Crystalline Solids, 2, 40 (1970).

33. J. T. Edmond, Brit. J. Appl. Phys., 17, 979 (1966).

34. M. Nunoshita, H. Arai, T. Taneki, and Y. Hamakwa, J. Non-Crystalline Solids, 12, 339 (1973).

35. J. Feinleib, J. DeNeufville, S. C. Moss, and S. R. Ovshinsky, Appl. Phys. Letters, 18, 254 (1971).

36. H. K. Henisch, E. A. Fagen, and S. R. Ovshinsky, J. Non-Crystalline Solids, 4, 538 (1970).

37. H. Fritzche and S. R. Ovshinsky, J. Non-Crystalline Solids, 2, 393 (1970).

38. A. D. Pearson, J. Non-Crystalline Solids, 2, 1 (1970).

39. D. L. Nelson, J. Non-Crystalline Solids, 2, 528 (1970).

40. G. R. Fleming, J. Non-Crystalline Solids, 2, 540 (1970).

41. H. J. Stocker, C. A. Barlow, and D. F. Weirauch, J. Non-Crystalline Solids, 4, 523 (1970).

42. N. F. Mott, Philosophical Mag., 24, 911 (1971).

43. H. Fritzche and S. R. Ovshinsky, J. Non-Crystalline Solids, 2, 148 (1970).

44. B. G. Bagley and H. E. Bair, J. Non-Crystalline Solids, 2, 155 (1970).

45. H. J. Stocker, J. Non-Crystalline Solids, 2, 371 (1970).

46. M. Guntersdorfer, J. Appl. Phys., 42, 2566 (1971).

47. E. A. Davis and N. F. Mott, Phil. Mag., 22, 903 (1970).

48. J. C. Male, Brit. J. Appl. Phys., 18(11), 1543 (1967).

49. J. A. Muir and R. J. Cashman, Opt. Soc. of Am., 57, 1 (1967).

50. H. Saki, K. Shimakawa, Y. Inagaki, and T. Arizumi, Jap. J. Appl. Phys., 13, 500 (1974).

51. M. M. Labes and O. N. Rudyj, J. Am. Chem. Soc., 85, 2055 (1963).

52. J. T. Edmond, J. Non-Crystalline Solids, 1, 39 (1968).

53. T. B. Brown, *Electronics*, John Wiley & Sons, New York, 1954, p. 310.

54. D. D. Pollack, *The Theory and Properties of Thermocouple Elements*, Am. Soc. for Testing & Materials, 1971, p. 15.

55. R. D. Mathis, *Evaporation With The Single Grain Box Source*, R. D. Mathis Co., California, 1963.

56. L. S. Birks, *Electron Probe Microanalysis*, Interscience, New York, 1963.

57. H. A. Liebhafsky, H. G. Pfeiffer, E. H. Winslow, and P. D. Zemany, *X-Rays, Electrons, and Analytical Chemistry*, Wiley-Interscience, New York, 1972.

58. J. R. Bosnell and U. C. Voisey, Thin Solid Films, 6, 161 (1970).

59. J. M. Marshall and A. E. Owen, Phil. Mag., 24, 1281 (1971).

60. N. F. Mott, J. Non-Crystalline Solids, 8-10, 1 (1972).

61. H. Stiegler and D. R. Haberland, J. Non-Crystalline Solids, 11, 147 (1972).

62. C. B. Thomas, A. F. Fray, and J. Bosnell, Phil. Mag., 26, 617 (1972).

63. D. M. Kroll, Physical Rev. B, 9, 1669 (1974).

64. W. van Roosbroeck, Phys. Rev. Letters, 28, 1120 (1972).

65. W. van Roosbroeck, J. Non-Crystalline Solids, 12, 232 (1973).

66. D. Armitage, D. E. Brodie, and P. C. Eastman, Canadian J. Physics, 49, 1662 (1971).

67. G. C. Vezzoli, P. J. Walsh, and L. W. Doremus, J. Non-Crystalline Solids, 18, 333 (1975).

68. J. R. Bosnell and C. B. Thomas, Phil. Mag., 27, 665 (1973).

69. K. Shimakawa, S. Nitta, Y. Inagaki, Jap. J. Appl. Phys., 10, 391 (1971).

70. M. Saji and K. C. Kao, J. Non-Cryst. Sol., 18, 275 (1975).

71. R. F. Ormondroyd, M. J. Thompson, and J. Allison, J. Non-Crystalline Solids, 18, 375 (1975).

72. S. Tolansky, *Multiple-Beam Interferometry of Surfaces and Films*, Clarendon Press, London, 1949.

73. C. H. Hurst and E. A. Davis, J. Non-Crystalline Solids, 16, 343 (1974).

74. N. Cusack and P. Kendall, Proc. of Phys. Soc., London, 72, 898 (1958).

75. T. M. Donovan, W. E. Spicer, J. M. Bennett, and E. J. Ashley, Phys. Rev. B, 2, 397 (1970).

76. R. Uttecht, H. Stevenson, C. H. Sie, J. D. Griener, and K. S. Raghavan, J. Non-Cryst. Sol., 2, 358 (1970).

77. K. Shimakawa, Y. Inagaki, and T. Arizumi, Jap. J. Appl. Phys., 11, 1319 (1972).

78. J. P. deNeufville, J. Non-Cryst. Sol., 8-10, 85 (1972).

79. J. A. Savage, J. Non-Cryst. Sol., 11, 121 (1972).

80. R. G. Neale, D. L. Nelson, and G. E. Moore, Electronics, 43, 56 (9/28/70).

81. K. Hulls and P. W. McMillan, J. Non-Crystalline Solids, 15, 357 (1974).

82. P. Chaudhari and S. R. Herd, J. Non-Crystalline Solids, 8-10, 56 (1972).

83. R. K. Quinn and R. T. Johnson, Jr., J. Non-Cryst. Sol., 12, 213 (1973).

84. R. B. Laibowitz, S. R. Herd, and P. Chaudhari, Phil. Mag., 28, 1155 (1973).

85. M. Roilos, D. Meimaris, and K. Zigiris, J. Non-Cryst. Sol., 7, 271 (1972).

86. R. Tsu, W. E. Howard, and L. Esak, J. Non-Cryst. Sol., 4, 322 (1970).

87. J. A. Savage, J. Materials Sci., 6, 964 (1971).

88. M. Noda, S. Maruno, and T. Yamada, Jap. J. Appl. Phys., 11, 1584 (1972).

89. K. Tanaka, Y. Okada, M. Sugi, S. Iizima, and K. Kikuchi, J. Non-Crystalline Solids, 12, 100 (1973).

90. K. S. Evstropyev and E. V. Porai-Koshits, J. Non-Cryst. Sol., 11, 170 (1972).

91. W. E. Spear, J. Non-Crystalline Solids, 1, 197 (1969).

92. R. E. Aitchison, Australian J. Appl. Sci., 5, 10 (1954).